The emission line properties of star-forming galaxies in the WEAVE-LOFAR survey

University of Hertfordshire

Submitted to the University of Hertfordshire in partial fulfilment of the requirement of the

degree of MSc by Research

Faye Davis

24/10/2020

Abstract

The third operational rehearsal of WEAVE-LOFAR has produced 7273 model optical spectra of radio-selected star-forming galaxies. It is the most realistic simulation of what we expect WEAVE's performance to be. The purpose of this research is to build an algorithm which can reliably extract emission line properties from the model spectra in preparation for the bulk arrival of the WEAVE-LOFAR data by the end of 2020. Spectral fitting software already exists; however, the algorithm described in this thesis has been designed to specifically model simulated WEAVE spectra. The algorithm uses Markov chain Monte Carlo (MCMC) techniques to determine posterior distributions of the emission line parameters, and is designed to accurately model low signal-to-noise (SNR) spectra of radio sources. The data preparation stages and the process of modelling the continuum, dust attenuation and the broad and narrow emission lines are discussed in detail in this thesis. The fundamental aim is to gain an insight into what we expect the real WEAVE data to resemble and understand everything we can prior to its arrival. This thesis presents evidence that reliable emission line diagnostics can be retrieved, even from low SNR spectra, by comparing their flux measurements to the input spectra. These emission line measurements are used to classify the targets into star-forming galaxies or AGN, with an accuracy of 89%. Hα fluxes are dust corrected using the Balmer decrement, from which star formation rates (SFR) are derived and compared to those derived from the SKA simulated skies LOFAR 150 MHz measurements. The purpose of this comparison is to understand how representative the radio derived measurements are of the SFR and whether a strong case can be made to use non-thermal radio continuum as an alternative SFR indicator. Radio surveys are very sensitive, impervious to dust and can survey the sky at fast speeds, therefore the use of this diagnostic will be highly beneficial to star formation research. During the process of this analysis, any complications or limitations presented by the model spectra are thoroughly investigated and reviewed. A potential issue with the flux calibration is highlighted which appears to distort the shape of the continuum, offsets the blue and red arm spectra and results in a 25% systematic offset from the input fluxes. Furthermore, the presence of skyline residuals, particularly at longer wavelengths, showed evidence of poor sky subtraction. Despite these issues, the research in this thesis provides a proof of principle that MCMC-based codes can be used in bulk to classify and recover physical information from WEAVE spectra.

Contents

1   Introduction

1.1   WEAVE

The WHT Enhanced Area Velocity Explorer (WEAVE) is a spectroscopic facility which is currently under construction for the 4.2m William Herschel Telescope on La Palma. It is expected to be operational by January 2021, at which point it can begin to retrieve optical spectroscopic data from selected targets. Two key purposes that drove WEAVE's design are to gather optical follow-up data for targets detected by the ground based Low Frequency Array (LOFAR) survey and the space based GAIA survey (Dalton et al., 2018). The spectrograph has been designed to cover a continuous wavelength range of 3600-9600 Å in low resolution mode (R $\sim$ 5000) and it has a multi-object spectrograph (MOS) equipped with an average of 950 fibres which will be assigned to targets spread over a circular field-of-view which is two degrees in diameter (Dalton et al., 2016). The spectrograph has a blue arm which will cover a wavelength range of 3600-6100 Å and a red arm which will cover 5800-9600 Å for all of the targets within a standard one hour observing block (Dalton et al., 2016). This will enable WEAVE to efficiently sample the sky, gathering spectra for hundreds of thousands of radio sources. WEAVE's ability to collect large quantities of data within a short time frame will accelerate the progression of its scientific goals. The final design of WEAVE is presented by Dalton et al. (2016), who expands on the instrumentation and manufacturing details along with the overall project schedule. Dalton et al. (2018) present an updated version of the construction progress along with a summary of the planning behind the 5-year initial phase of survey operations.

WEAVE-LOFAR is designed to efficiently sample the redshift-luminosity plane in order to obtain data for the brightest and rarest radio galaxies at high redshifts as well as the more abundant, fainter star-forming galaxies (Smith et al., 2016). WEAVE-LOFAR will have Deep, Mid and Wide tiers to complement the tiers of the LOFAR Surveys Key Science Project (Röttgering et al., 2011). This three tier 'wedding cake' strategy is described by Smith et al. (2016). WEAVE-LOFAR is one of the many different surveys that WEAVE will do; these will be described by Jin et al (in preparation). High redshift success rates for each of these tiers were estimated using simulations built based on the SKA simulated skies (Wilman et al., 2008), approaching 100% at $z < 1$ (Smith et al., 2016). WEAVE-LOFAR will provide spectroscopic redshifts and classifications of the radio-selected sources which will enable researchers to address a wide range of scientific topics: star formation history of the Universe, AGN accretion modes, the epoch of reionisation, cosmology, and understanding cluster haloes and radio relics (Smith et al., 2016).

Spectroscopy is a useful tool as it is used to measure the spectrum of a galaxy which holds valuable information about its distance, chemical composition, kinematics and physical properties. The wavelengths of emitted and absorbed radiation are known, as the energy levels of electrons within an atom or molecule are quantised. Redshifts and recession velocities can be derived using the wavelengths of spectral lines in the observed spectrum. The galaxy's distance can then be found using Hubble's Redshift-Distance law (Hubble, 1929) or the Velocity-Distance law (Harrison, 1993). The velocity dispersion of the stars within a galaxy can be derived from measurements of the spectral line broadening. The strengths of spectral lines produced by metals can be used to determine the average composition of

stars within a galaxy, which indicates an estimation of age. Information about the stellar population and dust attenuation can also be derived (approximately) from the shape of the spectrum; in the absence of dust, a redder spectrum suggests the galaxy is quenched of cold gas and only consists of older stars, while a bluer spectrum indicates the galaxy hosts young stars and is experiencing recent star formation. Spectroscopy is also used to measure the dark matter in galaxies using the Doppler shift and other physical conditions, such as temperature, by quantitative analysis of the strengths of emission lines (Massey & Hanson, 2013). All the information gained from the analysis of a galaxy's spectrum can be used to constrain models to better understand the evolution of the Universe.

1.2   WEAVE-LOFAR

By the end of 2021, WEAVE will be operational and shortly after it will begin to obtain optical spectroscopic data as follow-up for galaxies identified by the LOFAR Two-metre Sky Survey, LoTSS (Shimwell et al. 2017, 2019). As described by van Haarlem et al. (2013), the Low Frequency array (LOFAR) is a wide-field radio telescope with dramatic improvements over previous radio instrumentation designs. Its revolutionary design replaces the traditional, expensive mechanical dishes with a combination of simple receivers and modern computers. It has unique capabilities which set it apart from other telescopes; these include its incredible sensitivity to one of the last regions of the electromagnetic magnetic spectrum to be studied. One of LOFAR's groups of antennas is optimised for the 30 - 80 MHz range and the other is for the 110-240 MHz range. LOFAR is charting the entire northern sky in these unique frequency ranges at a resolution better than 1" (when international baselines are used), enabling the detection of the faintest galaxy populations. This frequency range is of particular relevance for research into AGN activity and for extragalactic sources dominated by synchrotron emission from star formation activity (Condon, 1992). van Haarlem et al. (2013) discuss some of the capabilities of the LOFAR facility and the 6 'Key Science Projects' that it plans to study: cosmic rays, epoch of reionisation, transients and pulsars, cosmic magnetism, the Sun, and extragalactic surveys.

WEAVE-LOFAR will be the primary source of optical spectroscopic information for the sources in the LoTSS survey (Röttgering et al. 2011; Shimwell et al. 2017; Smith et al. 2016). As part of the WEAVE-LOFAR survey, the spectrograph will obtain over a million fibre hours of spectroscopy for less than a million 150 MHz-selected LoTSS sources and provide high-precision spectroscopic redshifts and accurate classification of the sources (Smith et al., 2016). WEAVE's ability to obtain extensive spectroscopic data for an average of 950 LOFAR targets within a single one-hour exposure time makes it ideal for the efficient detection, redshifting and reliable classification of the sources. The scale of the survey and its unique selection, which is unaffected by dust, set it apart and it will be one of the most important UK-led spectroscopic surveys of the next 10 years. The observing speed, sample size and resolution of WEAVE will supersede that of previous multi-object spectrographs such as SDSS (York et al., 2000), AAOmega (Smith et al., 2004), and VIMOS (Le Fèvre et al., 2003). There are less than 1100 fibres between these three spectrographs, each with low- and high-resolution modes which will be surpassed by that of WEAVE's resolution modes (Smith et al., 2016).

WEAVE-LOFAR's unique radio-selection function will set it apart from previous and existing extragalactic spectroscopic surveys. Low frequency radio surveys are unaffected

by dust obscuration and identify highly active galaxies (i.e. those which host an AGN or significant star formation activity), resulting in a radio-source population rich in emission lines which is ideal for the determination of their redshifts. In contrast, a stellar mass or optical magnitude selected spectroscopic sample (e.g. GAMA (Driver et al., 2011), DEVILS (Davies et al., 2018) and WAVES (Driver et al., 2019)) include a large number of passive galaxies which require a continuum detection in order to deduce their redshift. With a radio-selected sample, WEAVE-LOFAR will obtain more redshifts per unit observing time, and more redshifts for sources with a very faint continuum. In summary, WEAVE-LOFAR is less biased in its selection compared to optical and near-infrared surveys, providing a more representative view of the galaxy population.

SDSS-LOFAR (Alam et al., 2015) is a previous radio-targeted survey in the ELAIS-N1 field with a sample size of 387 faint LOFAR sources at a resolution of R $\sim$ 2000, the scale and resolution of this survey would be superseded by WEAVE-LOFAR in a single good night of observation. WEAVE-LOFAR will be highly beneficial for extragalactic research due to the surveys efficiency at selecting targets for studies into the relationship between star formation and accretion, identifying radio galaxies in the epoch of reionisation and further understanding galaxy evolution and formation. Additionally, LOFAR is expected to routinely reach depths where the radio sky is dominated by star forming galaxies (Shimwell et al., 2017). WEAVE's spectroscopic data is ideal for classifying these radio sources according to their power source, whether this is star forming or AGN galaxies as well as between the accretion modes within the AGN themselves. WEAVE will also be used to measure their velocity dispersions, estimate metallicities and derive viral black hole mass estimates (Smith et al., 2016). Furthermore, WEAVE will also be the primary source of redshift information which is expected to be very efficient due to the dominance of emission-line galaxies and AGN in the faint radio source population. The efficiency of WEAVE-LOFAR is further magnified by LOFAR's fast survey speeds, due to its instantaneous field of view, and WEAVEs ability to output spectroscopic data for 950 targets within a single hour. Many thousands of WEAVE-LOFAR spectra thus offer a unique insight into the relationship between star formation and accretion over a huge swathe of cosmic history. Furthermore, LOFAR will also be surveying areas of the sky which already have multi-wavelength coverage in order to maximise the scientific return of the survey (Shimwell et al., 2017). WEAVE-LOFAR will enable the study of a broad range of subjects for both the rare high-value objects and the fainter more numerous sources.

1.3   WEAVE-LOFAR: Areas of scientific research

WEAVE-LOFAR is driven by the scientific motivation of advancing our knowledge of poorly understood processes occurring within our Universe. It will be able to enrich many areas of research with valuable, transformational data. The areas it will address are broad, ranging from the relationship between accretion and star formation to finding radio galaxies in the epoch of reionisation. Each area will be addressed in unprecedented detail. The Smith et al. (2016) proceedings highlight the primary scientific goals and the design of the WEAVE-LOFAR survey; a summary of a few of these goals are provided in this chapter.

1.3.1 Star formation history of galaxies over cosmological timescales

Star formation plays a key role in driving the structure and evolution of galaxies and it can be quantified by calculating the star formation rate (SFR) within a galaxy (McKee & Ostriker, 2007). There are various indicators which can be used to measure the SFR in a galaxy; these are discussed at length in section 3.3. By carefully studying our own galaxy and nearby ones in the local Universe, we know that there are certain physical conditions within molecular clouds which control the nature and rate of star formation (Evans, 1999). By measuring the SFR of a galaxy and comparing to the galaxy's other known properties, we can further understand the processes which drive star formation.

A galaxy's radio continuum luminosity has a roughly linear relationship with the SFR (e.g. Condon 1992; Bell 2003; Heesen et al. 2014), which makes LOFAR an ideal survey to trace star formation across the Universe. WEAVE's spectroscopic follow-up will be able to clearly distinguish between star-forming galaxies and AGN, which have very similar spectral characteristics (e.g. they are both emission line spectra which often contain strong ionisation lines). This will be done using BPT classifications (Baldwin et al., 1981) and the Kewley et al. (2001b) and Kauffmann et al. (2003) demarcation curves, which discriminate between starburst galaxies and AGN based on the dominant excitation mechanisms. I will be applying this method to the simulated star-forming spectra from WEAVE's third operational rehearsal in order to investigate how successfully the mock spectra can be classified.

The radio continuum selection identifies galaxies based on their star-formation activity as opposed to, for instance, near-infrared surveys which are biased to more massive galaxies as they can't be detected below a certain stellar mass (Eales et al., 2018). The survey will therefore target all environments and identify star formation in galaxies of all masses (Smith et al., 2016). This will allow the study of star formation in galaxies as a function of stellar mass, environment, and redshift. Understanding how the star formation evolves with stellar mass (M_*) can be used to constrain the stellar mass assembly histories of galaxies as well as the initial mass function (IMF) used to derive SFRs (Davé, 2008). The relationship between the SFR and environmental factors will provide valuable insight into how star formation impacts the morphology of the galaxy (disc-to-bulge ratio, concentration, surface density). The specific star-formation rate (SFR/M_*) of galaxies in the local universe correlates strongly with the local density; more massive galaxies are found in denser environments and populated by redder stars (Elbaz et al., 2007; Kauffmann et al., 2004). The star formation history of galaxies across cosmic time can be studied further with the WEAVE-LOFAR survey, with observations of star formation properties over a large range of redshifts.

WEAVE-LOFAR's large unbiased sample sizes and unique selection will lead to better determinations of the star formation rate density of the Universe (Madau et al. 1998; Madau & Dickinson 2014), the star formation rate function (Smit et al. 2012; Cai et al. 2014), and the fundamental metallicity relation (Mannucci et al., 2010), and provide a new insight on the physics behind the far-infrared radio correlation (van der Kruit 1971; Yun et al. 2001; Smith et al. 2014). WEAVE will also be able to determine metallicities and velocity dispersions in star-forming galaxies which can be compared with redshifts. With this information we can determine the mass and chemistry of the star-forming systems which will indicate how stellar populations form and evolve over a huge period of cosmic time (Smith et al., 2016).

1.3.2 Active Galactic Nuclei (AGN)

AGN are extremely luminous compact objects found at the centre of a galaxy which emit radiation across the electromagnetic spectrum. This radiation is a result of the material in the surrounding accretion disk falling onto the central black hole; Shlosman et al. (1990) outline a unified model for the mechanisms and fuel that drives this accretion. The approximate structure of AGN is known; however, the physical processes occurring within them are often hidden from view (Antonucci 1993; Becker et al. 2001). Researchers want to understand these extreme processes as they are our principal probe to earlier epochs of the Universe due to their high luminosity, so it is vital to study them in order to understand how the Universe has evolved over cosmic time (Urry & Padovani, 1995). Our ability to detect radiation emitted by AGN depends on factors such as its orientation (Lagos et al., 2011), the density of gas and dust that surrounds the AGN and its luminosity. Material from a galaxy's dusty interstellar medium can be sufficient to attenuate the optical, ultra-violet (UV), and soft X-ray emission from an AGN accretion disk, but hard X-rays with shorter wavelengths ($\lambda_e <$ 0.2 nm) are not obscured (Heckman & Best, 2014).

Starburst galaxies experiencing rapid star formation have similar optical spectral characteristics to that of an AGN, making it hard to distinguish between these galaxies. However, AGN can be distinguished from star-forming galaxies as they have different excitation mechanisms (Baldwin et al., 1981). This results in an AGN containing a wider range of ionisation emission lines with different relative strengths in their spectrum and a significantly greater range of velocities to that of a star-forming galaxy (Osterbrock, 1989). It is important to distinguish between them as it is thought there are important processes occurring due to AGN activity which greatly affect star formation within the galaxy, and consequently its evolution (Heckman & Best 2014; Sabater et al. 2019). The WEAVE-LOFAR survey will enable us to classify AGN and star-forming galaxies as well as identify properties of AGN such as their accretion rate, black hole mass and the power of the jets (Smith et al., 2016). The combination of optical and radio data will further our knowledge of the relationship between star formation and AGN. Evidence of this is demonstrated by Hardcastle et al. (2019) who combine a LoTSS (Shimwell et al., 2017) radio sample with the SDSS (York et al., 2000) spectroscopic sample for local radio source populations to distinguish between star-forming galaxies and AGN and investigate how stellar and black hole mass relates to radio-AGN activity.

If accretion is above a certain fraction of the Eddington rate, then observationally we obtain radiatively efficient AGN which radiate a large fraction of the accreted energy as photons: some people call this 'quasar mode' (Best & Heckman, 2012). The Eddington limit is when the gravitational force of the black hole no longer balances the opposing radiation pressure acting outwards and therefore the accreting material would no longer be in hydrostatic equilibrium (Osterbrock, 1989). Jets are present in some AGN, with a jet power related to the spin of the black hole. The accretion rate is indirectly related to the magnetic field, thus the radiative efficiency of the object is independent of the power of the jets (Hardcastle & Croston, 2020). The radiation and the jets have different feedback effects. In our current understanding of AGN feedback, radiatively efficient AGN can drive cold gas out of the galaxy to terminate star formation activity (Fabian, 2012). This can happen when the energy produced by the growth of a black hole exceeds the binding energy

of the bulge by a large factor. If even a small fraction of this energy is transferred to the gas, then the active nucleus can have an immense effect on the stellar evolution of its host galaxy (Fabian, 2012). It is suggested that this feedback is one quenching mechanism due to AGN activity that explains the difference between the observed galaxy mass function and theoretical cold dark matter cosmology mass function (Bongiorno et al. 2016; Baldry et al. 2008). Powerful AGN jets provide a lower rate of energy input which may not drive the cold gas out of the galaxy, but can result in the heating of the cold galactic medium and the presence of a hot halo (Best & Heckman 2012; Fabian 2012). The jets prevent the hot gas falling onto the galaxy and consequently inhibit star formation; another factor that can explain the luminosity function conundrum.

The WEAVE spectroscopic data will be able to determine the radiative efficiency of an AGN by detecting the presence of high ionisation emission lines in the spectra of the highly luminous 'quasar mode' which are absent in AGN with radiatively-inefficient accretion (Smith et al., 2016). Radiatively-inefficient accretion, where inflow time is much shorter than the radiative cooling time, results in a reduced emission of high energy photons (Hardcastle et al., 2007). Distinguishing between the two will enable researchers to further analyse AGN accretion mechanisms. It will also provide vital data for the testing of simulations in order to better understand the relationship between star formation and accretion over cosmic time (Smith et al., 2016).

WEAVE-LOFAR will be surveying the LoTSS sky (Shimwell et al., 2017), a deep radio survey which will enable us to explore the abundant population of radio-quiet AGN activity and evolution at redshifts greater than 1. By detecting these sources with radio telescopes, the observation of the AGN will not be obscured by dust and the survey will be able to make a complete census of black hole accretion which will include sources missed by X-ray surveys. WEAVE-LOFAR will work to enable the study of properties and characteristics of the AGN and observing how they vary with redshift. LOFAR data will help us to determine the jet power via the radio luminosity, and the accretion rate can be determined by calculating the emission line luminosity using the WEAVE spectroscopic data (Smith et al., 2019). As described in section 2, I will use simulated spectra of WEAVE to determine how successfully the emission line properties required for these studies can be extracted as well as distinguishing between star-forming galaxies and AGN.

1.3.3   Epoch of Reionisation (EoR)

The EoR is the period in the history of the Universe where the first sources of radiation with energy greater than 13.6eV ionised the intergalactic medium which predominantly consisted of neutral hydrogen (Barkana & Loeb 2001; Loeb & Barkana 2001). During the Epoch of Recombination, which preceded the EoR, the Universe cooled and hydrogen became neutral as ions and electrons recombined (Sunyaev & Chluba 2009; Seager et al. 1999). Once the last scattering occurred, the intergalactic medium was composed entirely of neutral particles. During this period of neutrality there were no short wavelength sources, and if any were emitted they would have been absorbed immediately by hydrogen. Since the Universe was opaque during this period, it is referred to as the Dark Ages (Zaroubi, 2013). Over time the Universe expanded and cooled which allowed the collapse of over dense regions caused by dark matter. The collapsed baryonic matter led to the formation of the first stars in the Universe

(Madau & Dickinson, 2014). It is believed that these first stars were the source of high energy radiation required to ionise hydrogen (13.6eV). Hence this began the Universe-wide phase transition to ionised plasma, or in other words, the Epoch of Reionisation. Choudhury & Ferrara (2006) review the physical processes governing the cosmic reionization.

Gunn & Peterson (1965) discuss the Lyman alpha forest in a quasar at $z = 2.01$. This work later led to our understanding that we can probe the end of the EoR by locating a Gunn-Peterson trough with complete absorption (i.e. a neutral intergalactic medium). The first observation of this was made by Becker et al. (2001) at a redshift of $z > 6$ in a spectrum of a quasar which indicated that ionisation was not complete at $z > 6$. The 21-cm hydrogen line is another potential means for studying this period, as it occurs very rarely and is also temperature dependent. If we can detect and study this line it would be possible to learn more about the early structure of the Universe.

The recent discovery and study of a quasar at $z > 7$ suggests reionisation is incomplete 750 Myr after the Big Bang (Matsuoka et al., 2019). WEAVE-LOFAR will be able to map the distribution of neutral gas at $z > 6$ in the wide tier as it will be capable of locating radio AGN at $z > 6$ every 200 deg^2 of the northern sky. At 10,000 deg^2 the survey is expected to have collected spectroscopic data for 50 of these radio selected quasars. This provides multiple lines of sight, which increases the chance of targeting the brightest and highest-redshift sources (Smith et al., 2016). High redshift radio galaxies and quasars can also be used to probe the end of the EoR; however, we are more likely to find quasars as they are bright in the optical and so will be selected as WEAVE targets. Different samplings of the intergalactic medium across multiple lines of sight will also indicate if there is any variation in the Gunn-Peterson troughs at $z \sim 6$.

WEAVE-LOFAR aims to chart the end of the Dark Ages when the first stars formed and began to ionise the neutral baryonic gas. The advanced technical capability of WEAVE opens up a redshift window range of 5 - 6.9 onto the EoR. Many questions will be answered such as: the redshift range for the bulk of ionisation, how long the reionisation took, which sources were responsible for it and identification of different stages of the process (Röttgering et al., 2011). I will investigate the limitations of extracting emission line properties from WEAVE's simulated mock spectra at the high wavelength range and review how achievable WEAVE's EoR goals are.

2 Project description and motivation

In 2019 the WEAVE consortium conducted a realistic end-to-end simulation of the WEAVE data flow, including realistic model input spectra for WEAVE-LOFAR sources. The details of WEAVE's third operational rehearsal are described by Jin et al (currently in preparation). It is the most realistic simulation of what we expect WEAVE's performance to be. The simulation of the mock spectra accounts for all the different places the MOS will lose signal; the quantum efficiency of the chips, the atmospheric transmission above the telescope, the fact that some photons are lost as they travel through the optical fibres and more. The simulation has built thousands of model optical spectra for the LOFAR selected star-forming galaxies. These mock spectra are physically motivated models of what the optical spectroscopic observations of these sources will look like with WEAVE, with a realistic range of emission line

fluxes and continuum properties. I will henceforth refer to the mock spectra output by this rehearsal as the OPR3 spectra.

The fundamental goal of my work in this thesis is to develop, test and verify a fitting algorithm for emission lines within the OPR3 spectra of star-forming galaxies which can also be used on real spectral data in the future. Spectral fitting software already exists, such as GANDALF (Sarzi et al., 2006), which is what the WEAVE processing pipeline is using, however mine will use Markov chain Monte Carlo (MCMC) techniques to determine posterior distributions on the continuum, dust attenuation and emission line parameters which makes it unique. The parameter estimates can be compared with those output by GANDALF, which will enable WEAVE researchers to isolate issues within the algorithms. The algorithm is also specifically intended to accurately model for lower SNR spectra and is designed with radio sources in mind, whereas GANDALF is programmed for high SNR spectra of E and S0 galaxies (Sarzi et al., 2006).

The fitting algorithm will provide parameter estimates for the Hα λ6564 Å, Hβ λ4861 Å, OIII λ5007 Å and the NII λ6584 Å line profiles which will be used to determine their integrated fluxes and line luminosities. These specific integrated fluxes are fundamental requirements to produce a BPT diagram (Baldwin et al. 1981), and the dust corrected Hα luminosity will be used to calculate the SFR of the target galaxy. I will test how successfully the WEAVE spectra can be used to determine SFRs and subsequently verify the SFR(L$_{150}$) by comparing it to the SFR(Hα) estimates of the OPR3 sample. The SFR(L$_{150}$) values have been calculated from the low-frequency radio luminosity–SFR relation derived by Gürkan et al. (2018) using the 150MHz radio continuum of the galaxies from the SKA simulated skies (Wilman et al., 2008). Radio surveys are very sensitive, impervious to dust and can survey the sky at fast speeds, therefore it will be highly beneficial to star formation research if the 150MHz radio continuum can be used to accurately determine the SFR of a galaxy. Hα derived SFRs are used in comparison as they are the most reliable among other optical emission line tracers (e.g. Moustakas et al. 2006).

One of the outcomes of my investigation will be a thorough review of the OPR3 spectra and the simulation that built it. This is not necessarily a goal or the purpose of my research, however it is a benefit of working closely with the data. Ultimately, I want to learn everything I can about what WEAVE-LOFAR spectra for star-forming galaxies will resemble, and how reliably we can retrieve emission line information, perform BPT classifications and measure SFRs.

3 Literature reviews

3.1 Spectral fitting software

There are many spectral fitting software packages which are readily available for use such as: PAN (Peak Analysis) by Dimeo (2005), STECKMAP (STEllar Content and Kinematics via Maximum likelihood A Posterior) by Ocvirk et al. (2006), GIPSY (Groningen Image Processing System) by van der Hulst et al. (1992), pPXF (Penalized Pixel-Fitting) by Cappellari & Emsellem (2004), slinefit by Schreiber (2019) and GANDALF by Sarzi et al. (2006). The fundamental aim of these programmes is to semi-automatically fit a selected model to a given

spectrum. Each of the listed software packages have been designed for different purposes, with differing user-friendly tools and features. It is wise to research the pros and cons of each programme before attempting to use it. I have reviewed three of these methods below, including GANDALF which will be used by the standard WEAVE data analysis pipeline.

3.1.1 PAN: Peak Analysis

PAN (Peak Analysis) by (Dimeo, 2005) is an IDL-based software with many built in functions which can be used simultaneously for spectral line fitting. It applies the Levenberg-Marquardt (LM) least-squares minimisation fitting algorithm to estimate the optimal parameters of a model to the data. The LM technique is expanded upon in section 4.4. PAN is mostly tailored towards integral-field spectroscopy data which have potentially hundreds of spectra. Whereas WEAVE's MOS is designed to assign each of its fibres to a different target, the integral field spectroscopy technique produces a 2D map of the flux of a galaxy as a function of position. York et al. (2000) discusses the observing strategy using integral field spectroscopy for targets in the SDSS-IV survey.

PAN is capable of reading in multiple spectra simultaneously, and automatically fits an initial guess to each of these. Its interactive features set it apart from other spectral fitting software as it minimises the amount of typing by allowing the initial parameters (e.g. Gaussian centre, amplitude and width) to be selected with a mouse. This would be problematic for WEAVE as it can output an average of 950 spectra per hour, hence it requires an automatic fitting procedure with minimal interaction to initiate it. PAN visually displays the spectrum and the fit along with the parameters and statistics in a graphical user interface, providing a convenient way of reviewing the quality of the fit. The documentation for PAN (Dimeo, 2005) lists the following features:

- Library of fit functions: Gaussian, Lorentzians, lognormal, sloping background

- Use the mouse for interactive initial parameter entry

- Automatically fit multiple groups to the same model

- Constrain parameters with upper and lower bounds

- Specify number of fit iterations

- Visualise the correlation of fit parameters in an intuitive way

There are limitations to using the LM fitting algorithm on nonlinear least squares problems as it can get stuck in local minima and not converge to the optimal solution (Gavin, 2013). The fitting algorithm will converge to different local minima depending upon values of the initial guess, the noise of the spectrum, and additional parameters. PAN is unable to tackle this issue and is therefore not capable of handling optimisation problems with a high dimensionality. PAN was initially written by Rob Dimeo at NIST Centre for Neutron Research in 2002 for the analysis of neutron scattering. An astronomical version has since been developed by Mark Westmoquette (Westmoquette et al., 2007); adding modules to convert FITS data into a format PAN can read, modifying the way it outputs the fit results so it

can be read by a plotting package and enabling the algorithm to handle features such as line doublets. Westmoquette et al. (2007) adapted PAN for the automated fitting of 500 spectra each containing eight emission lines, taking advantage of PAN's ability to read in multiple spectra at once in an array format and allowing the user to visually and interactively specify amplitude, position and width. WEAVE will produce thousands of spectra for the entire northern sky which cannot be individually inspected, therefore it will not benefit from PAN's interactive design.

3.1.2 pPXF: Penalized Pixel-Fitting

pPXF was developed by Cappellari & Emsellem (2004) to extract the stellar kinematics from absorption-line spectra of galaxies, using a maximum penalized likelihood approach. Penalization essentially enables algorithms to overcome instability problems which arise when the likelihood is relatively flat, making the determination of the maximum likelihood estimate difficult. This method was further upgraded by Cappellari (2017). pPXF is the most efficient and reliable implementation of the 'Full-Spectrum Fitting' method, using high-quality synthetic templates to model the continuum and study the stellar population of galaxies (e.g. Bruzual & Charlot 2003). The Calzetti et al. (2000) attenuation curve is used to determine the attenuation suffered by the spectrum, and spectra which are heavily contaminated by the skylines can be corrected for using a sky spectrum. There are many other features included which result in the optimal fitting of spectra and extraction of multiple stellar kinematic properties whilst simultaneously fitting emission lines. This is particularly useful when studying the stellar population of galaxies with prominent emission lines which overlap important absorption features. Sarzi et al. (2006) describes GANDALF, another spectral fitting software which implements pPXF, which will be used in the WEAVE processing pipeline to model and fit the output spectra.

3.1.3 GANDALF: Gas and Absorption Line Fitting

GANDALF is a spectral fitting procedure developed for the analysis of the SAURON data described by Sarzi et al. (2006) for the purpose of accurately separating the stellar continuum and emission line contribution of the observed spectra. The SAURON team developed this software to measure the ionised-gas emission, spatial distributions, stellar and gas kinematic behaviours, line ratios and dust absorption features of their sample.

GANDALF implements the pPXF fitting software to determine stellar kinematic properties and simultaneously extracts information about the galactic ionised gas of emission line spectra. The fitting procedure accurately separates stellar continuum from the emission flux contribution, models reddening by interstellar dust and also returns formal errors on the position, width, amplitude and flux of the emission lines along with the derived stellar kinematics. This would normally be achieved by masking emission line regions within the spectrum, fitting a superposition of templates to the stellar continuum and subsequently measuring the gas emission using a Gaussian model. As shown by Sarzi et al. (2006), masking emission regions can introduce contrived structures in the residual, template-subtracted spectra that can be mistakenly modelled as nebular emission. GANDALF overcomes these limitations by extending the pPXF software to obtain a more refined procedure which mea-

sures the gas kinematics and fluxes without any spectral masking. The key ingredient in GANDALF is to model emission lines with Gaussian templates and, while iteratively searching for their best velocities and velocity dispersions, to solve linearly at each step for their amplitudes and the optimal combination of the stellar templates. GANDALF is also capable of matching complicated models to line profiles which are non-Gaussian, for instance: red- or blue-shifted tails, lines with Voigt profiles, and broad line components. The outputs of the fit, as listed by Sarzi (2012), include: the input spectrum, the optimal combination of stellar templates and the best fitting model and parameters for both the stellar kinematics and emission line components. GANDALF was developed for the SAURON data, therefore its functions are specified for this data set with its purpose for the research goals of Sarzi et al. (2006).

GANDALF will be used in the WEAVE processing pipeline to model and fit the output spectra. Unlike GANDALF, the algorithm described in this thesis will use MCMC methods to determine posterior distributions on the continuum template, dust extinction and emission line parameters. This algorithm is specifically intended to accurately model for lower SNR spectra and designed with radio sources in mind, whereas GANDALF is programmed for high SNR spectra of E and S0 galaxies (Sarzi et al., 2006). As stated, the algorithm will be built with the intention of recovering emission line parameters and flux estimates for the lines in the BPT diagram and to derive SFRs.

3.2   The BPT diagram

The BPT diagram is named after the authors of Baldwin et al. (1981): Baldwin, Phillips and Terlevich. Their research showed that the emission line spectra of most extragalactic objects can be classified into one of four groups corresponding to the predominant excitation mechanisms: photoionisation by UV radiation from hot O/B stars (HII regions or starburst galaxies), power-law photoionisation (AGN), shock-wave heating (LINER galaxies: Low Ionisation Nuclear Emission Line Region, Heckman 1980) and planetary nebulae photoionised by stars much hotter than O stars. This is done by using the intensity ratios of strong emission lines which measure various aspects of the excitation level in each galaxy. Baldwin, Phillips and Terlevich were unable to find a single emission line ratio which clearly distinguished between all four excitation mechanisms, this indicated the necessity of a two dimensional diagram. They were successful in discovering several combinations of lines which can be used to separate emission line spectra into one of the four ionisation categories. Hence this led to a graphical classification approach using plots of [NII]6584/Hα vs [OIII]5007/Hβ, and of [OII]3727/[OIII]5007 vs [OIII]5007/Hβ, [NII]6584/Hα, or [OI]6300/Hα as demonstrated in Fig.1.

Previously used classification schemes depended more on the selection criteria, morphology, or line widths rather than on the relative intensities of the emission lines. This disregarded the excitation mechanism acting on the gas, which most strongly links many of the emission spectra together and clearly separates others. The increasing quantity of data on emission line galaxies at the time brought about the need for a quantitative classification system which gives a direct measure of the main excitation mechanism operating on the gas.

The line selection criteria for the intensity ratios required the lines to be easily and accurately measured. Factors such as the line widths, continuum and instrumental limitations
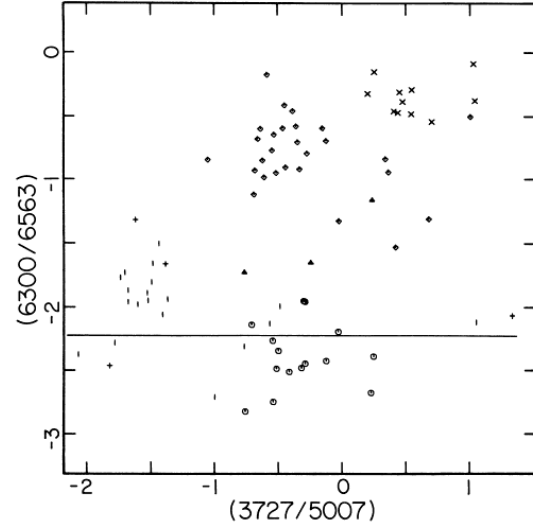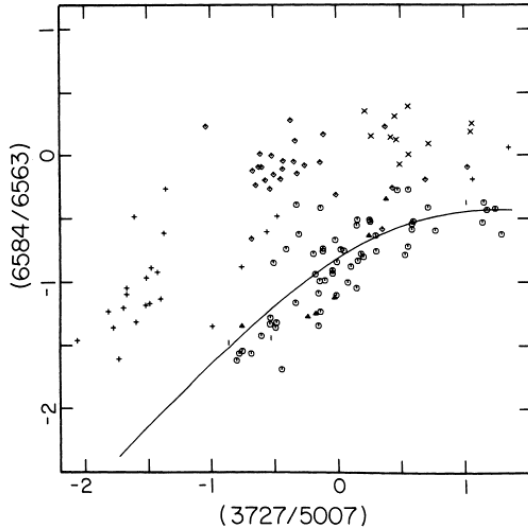
(a) Flux ratios: log [OII]/[OIII] vs log [NII]/Hα   (b) Flux ratios: log [OII]/[OIII] vs log [OI]/Hα

(c) Flux ratios: log [OII]/[OIII] vs log [OIII]/Hβ   (d) Flux ratios: log [NII]/Hα vs log [OIII]/Hβ
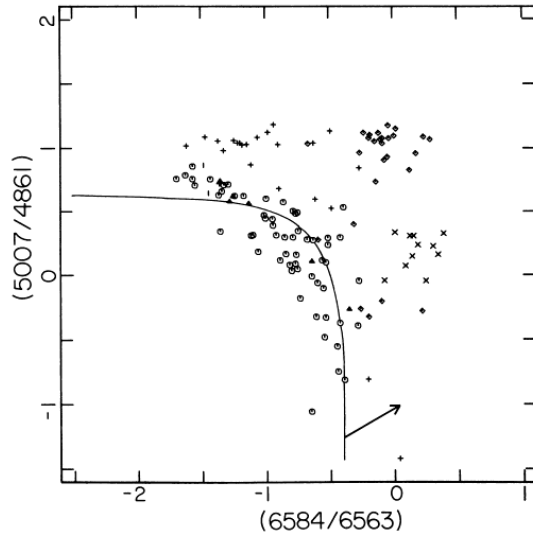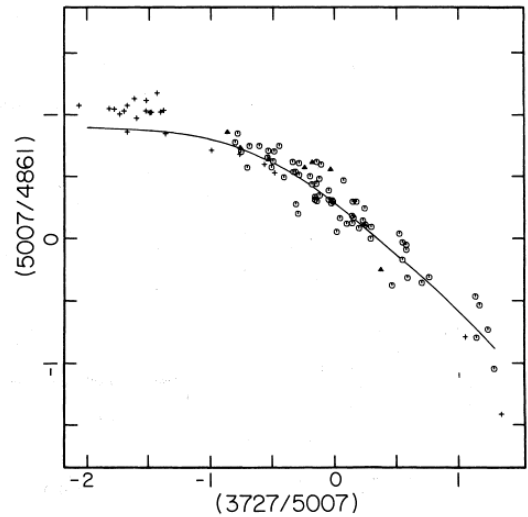
Figure 1: Four BPT plots from Baldwin et al. (1981) showing the relationships between two sets of intensity ratios for HII regions and planetary nebulae. The intensity ratios are expressed in logarithms with reddening corrections applied as described by Baldwin et al. (1981). Symbols: octagons = normal HII regions; triangles = detached extragalactic HII regions; + = planetary nebulae; vertical bar = upper limit on y axis ratio; diamonds: regions photoionised by power laws, X = shock-heated galaxies. Fig.1d will henceforth be referred to as BPT-NII.

can strongly affect the accuracy and uncertainty on the intensity measurements, therefore it is desirable to use a variety of line strengths. It was also important to avoid pairs of weak lines and select pairs within close wavelength proximity to each other in order to make the ratios nearly reddening independent. Certain lines were also avoided due to measurement

difficulties arising from blending with other emission and absorption lines. The main aim was to find line combinations which arise from different excitation mechanisms. For instance the Balmer lines can be used to trace HII regions, and their pairings are forbidden lines which can only be observed in extremely low density gases and plasmas.

The BPT-NII diagram shown in Fig.1d is the most commonly used version of the BPT plots as its line pairings are within a close wavelength proximity which ensures that their ratio is nearly reddening independent and minimises the effects of errors in the flux calibration. The Fig.1d BPT-NII diagram shows four distinct regions, corresponding to the four excitation mechanisms. Following the release of Baldwin et al. (1981), Balzano (1983) used the BPT-NII line diagnostics to classify starburst galaxies and Keel (1983) used the diagram to distinguish between the power-law photoionisation and shock heating excitation mechanisms in low-ionisation emission nuclei (defined as LINERs by Heckman 1980 using a similar data set).

Veilleux & Osterbrock (1987) refined the Baldwin et al. (1981) method by comparing observations of emission line galaxies with photoionisation models of power-law spectra and hot stars. They suggested a new classification method using line ratios involving [OIII] $\lambda 5007$, [NII] $\lambda 6583$, [SII] $\lambda 6716$, [SII] $\lambda 6731$, [OI] $\lambda 6300$, and the Balmer lines. They excluded reddening-sensitive line ratios such as [OII] $\lambda 3727$/[0III] $\lambda 5007$ used by Baldwin et al. (1981). Veilleux & Osterbrock (1987) showed that their revised method could be used to classify emission line galaxies into narrow-line AGNs and starburst galaxies. In more recent work, Stasińska et al. (2006) applied the BPT-NII diagram to distinguish star-forming galaxies and AGNs using optical spectra of 20,000 galaxies from the SDSS sample (York et al., 2000). They concluded that the BPT-NII line ratios were more efficient at classifying galaxies than other tested line diagnostics since it resulted in the clearest division of the galaxy population, and also simple photoionisation models under-predicted the other ratios. The drawback of this diagram is the use of the [NII] $\lambda 6583$ and [OIII] $\lambda 5007$ forbidden lines, making the diagrams sensitive to the N/O abundance ratio (Dopita & Evans 1986; Dopita et al. 2000, 2006).

[NII] $\lambda 6583$ and [OIII] $\lambda 5007$ are high ionisation forbidden lines which means their associated transitions have a very low probability of occurring in most environments, due to the more likely occurrence of collisional de-excitation. Hence, forbidden emission lines are more likely to be generated by harder ionisation sources, such as AGN, in extremely low density plasmas where atomic collisions are very unlikely to occur. Hα is a permitted, non-forbidden transition that will be more prevalent in high density regions like those that host dense gas and star formation. The ratio between NII and Hα indicates which process is dominating the gas ionisation in the galaxy. If the forbidden line flux is higher, then it is AGN dominated, and if the permitted line flux is higher, then it is star formation dominated. Note that both AGN and star-forming regions contribute to both lines, but the AGN contributes more to the forbidden lines and less to the permitted lines than a star-forming galaxy.

The dividing line between these two ionising sources has been well studied and developed. Kewley et al. (2001b) describes the process of placing a theoretical demarcation line between starburst and AGN galaxies based on the Veilleux & Osterbrock (1987) optical diagnostic diagrams. They used a combination of photoionisation and stellar population synthesis models which allowed for a wide range of metallicities, ionisation parameters, dust depletion and also accounted for the effects of shock excitation. They were able to show that continuous
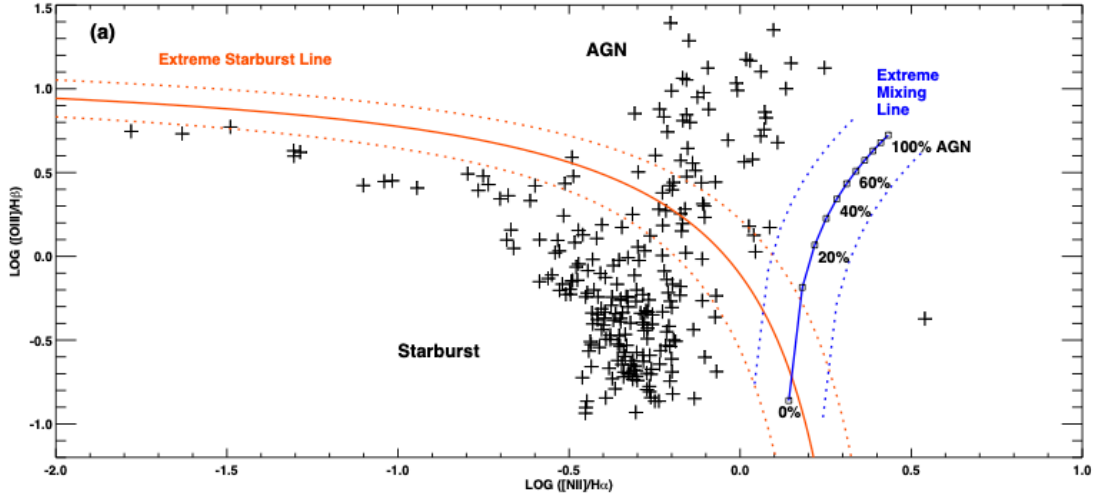
Figure 2: Diagnostic diagram from Kewley et al. (2001b) showing the emission line flux ratios of galaxies from their sample in a BPT-NII diagram. The theoretical classification line described by Eq.1 is represented by the thick orange line ('extreme starburst line') and an 'extreme mixing line' is shown by the thick blue line. The dashed lines of corresponding colours represent ± 0.1 dex of these lines (log width of 0.1), to indicate the error range of the modelling. Any combination of ratio pairings that place the galaxy below the extreme starburst line is classified as a starburst galaxy, otherwise it is classified as an AGN. The extreme mixing line separates AGN galaxies into Seyferts (above) and LINERs (below).

starburst models produced by any modelling procedure always fell below and to the left of an empirical limit on the BPT-NII diagram. The line dividing the starburst region from other types of excitation is represented by the orange line in Fig.2 and parameterized by Eq.1.

$$\log\left(\frac{[\text{OIII}]\ \lambda 5007}{\text{H}\beta}\right) = \frac{0.61}{\log\big([\text{NII}]\lambda 6583/\text{H}\alpha\big) - 0.47} + 1.19 \tag{1}$$

The exact division between star-forming galaxies and AGN in the BPT-NII diagram is subject to considerable uncertainty. The best guess estimate for the error on the Kewley et al. (2001b) dividing line is indicated by the dashed orange lines in Fig.2. This accounts for uncertainties in the modelling, assumptions made in the chemical abundances, chemical depletion factors, the slope of the IMF and the evolutionary tracks. Nevertheless, their results indicated that their theoretical starburst line is a reliable tool for optically classifying galaxies into starburst and AGN types and is more consistent from diagram to diagram than the Veilleux & Osterbrock (1987) classification method.

An extreme mixing line is represented by the blue line in Fig.2 which was produced by Kewley et al. (2001a) using shock modelling to classify galaxies into starburst, LINER, and AGN types (e.g. Seyfert 1 and 2 types). AGN are divided into two groups: LINERs (Heckman, 1980) and Seyfert galaxies (Seyfert, 1943). It is important to note that not all LINERS are likely to be AGN driven. For instance, Davis et al. (2012) used integral-field spectroscopy to conclude that the LINER NGC 1266 does host a deeply embedded AGN, however the ionised gas emission is extended and likely arises from fast shocks caused by

the interaction of the radio jet with the interstellar medium. Liners are a controversial classification, with many claims that the source of the ionisation is that of an AGN (Ho et al., 1993), fast shocks (Dopita & Sutherland, 1995) or photo-ionisation via UV emission from young, massive OB stars (Sarzi et al., 2010). Seyferts contain broad emission lines in their spectra which arise from its bright, semi-stellar nucleus (Khachikian & Weedman, 1974). Seyferts are separated into class 1, where the Balmer lines are thousands of km s^{-1} wide and much broader than the forbidden lines, and class 2, in which the two line species are the same widths around 500 - 1000 km s^{-1}; the Seyfert 2 lines are wider than the type 1 forbidden lines (Khachikian & Weedman, 1974). Both Seyfert type AGNs are photoionised by a non-thermal or power-law continuum (Koski, 1978; Veilleux & Osterbrock, 1987). LINERs are dominated by low ionisation emission lines and are photoionised by power-law continua (Veilleux & Osterbrock, 1987), however there is evidence of shock-wave heating (Dopita et al., 1997). The spectra of starburst galaxies are characteristic of HII regions, where the excitation mechanism is also due to the photoionisation by hot stars (Huchra, 1977).

Kauffmann et al. (2003) revised the Kewley et al. (2001b) demarcation curve between starburst galaxies and AGN. They examined the properties of a sample of narrow-line AGN galaxies selected from the SDSS sample (York et al., 2000), which used a pair of multi-fibre spectrographs to conduct a spectroscopic survey of about a quarter of the extragalactic sky for nearly 600,000 galaxies. Fig.3 is a BPT-NII plot for all the emission line galaxies in the sample which have a signal-to-noise ratio (SNR) > 3 in all four lines. The Kewley et al. (2001b) line is represented by the dotted line in Fig.3 which Kauffmann et al. (2003) describes as a very conservative lower limit on the true number of AGN in their sample. In Fig.3 it is evident that the AGN sequence separates from the starburst galaxies well below the Kewley et al. (2001b) demarcation curve. Therefore Kauffmann et al. (2003) revised the formula and derived an inequality which defines when a galaxy can be classified as an AGN. This equation is displayed in Eq.2 and represented by the dashed line in Fig.3.

$$\log\left(\frac{[\text{OIII}]\ \lambda5007}{\text{H}\beta}\right) > \frac{0.61}{(\log([\text{NII}]/\text{H}\alpha) - 0.05} + 1.3 \tag{2}$$

A BPT-NII diagram and the Kauffmann et al. (2003) demarcation curve will be used to retrieve classifications of the star-forming galaxies in the OPR3 sample. Galaxies from this sample will be classified into either star-forming or AGN types using MCMC estimated flux ratios and the Kauffmann et al. (2003) demarcation curve. This will be compared with measurements of their input spectra to indicate how accurately the algorithm will be able to determine emission line fluxes in the WEAVE spectra and reliably classify the galaxies. It is important that WEAVE will be able to distinguish between star-forming galaxies and AGN in order to study the processes occurring within them, gain a better understanding of their evolution and formation and also enable researchers to classify the accretion modes within the AGN.
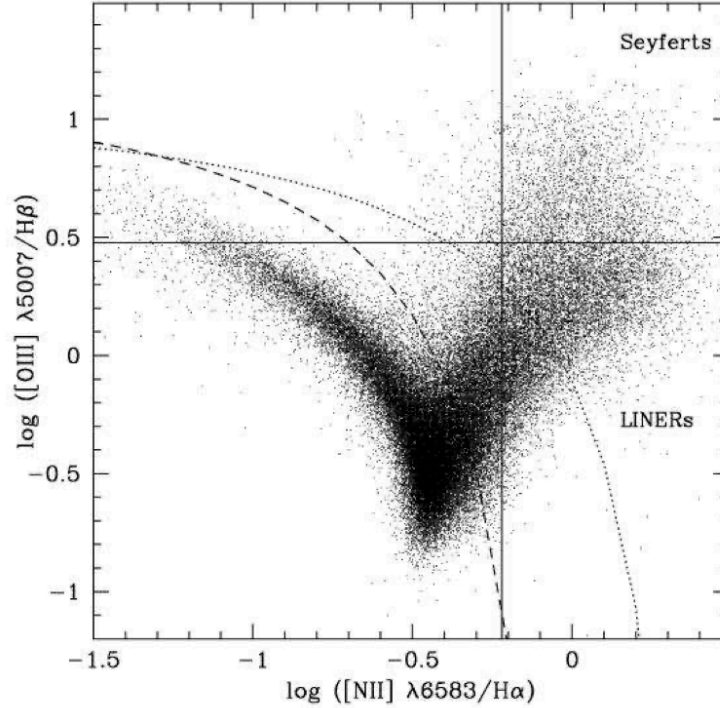
Figure 3: An example of a BPT diagram in which Kauffmann et al. (2003) plot the emission line flux ratio [OIII]/Hβ versus the ratio [NII]/Hα for all the galaxies in their sample where all four lines are detected with a SNR > 3. The 55,757 objects in their sample were taken from the Sloan Digital Sky Survey. The dotted curve shows the demarcation between starburst galaxies and AGN defined by Kewley et al. (2001b) (Eq.1). The dashed curve shows the revised demarcation (Eq.2). A total of 22,623 galaxies lie above the dashed curve. Seyfert galaxies are often defined to have [OIII]/Hβ > 3 and [NII]/Hα > 0.6, and LINERs to have [OIII]/Hβ < 3 and [NII]/Hα > 0.6. According to this definition, their sample includes 2,537 Seyferts and 10,489 LINERs.

3.3   Measuring star formation within a galaxy

Galaxies consist of gas, dust, stars, planetary systems, black holes and dark matter, and each component impacts the galaxy's evolution. Factors such as the stars' composition, age, IMF, metallicity and the rate of formation within a galaxy can be measured as a function of redshift in order to study the process of galaxy formation and how it has evolved over the lifetime of the Universe. A way of quantifying the evolution is by measuring the rate of star formation within the galaxy. SFRs can indicate vital clues about the evolutionary history and formation of the galaxy and the physical processes that drive it, especially when compared to other properties such as stellar mass. New facilities over the past two decades, such as the Galaxy Evolution Explorer (GALEX; UV; Martin et al. 2005), Spitzer Space Telescope (IR; Werner et al. 2004), the Herschel Space Telescope (FIR and sub-millimetre; Pilbratt et al. 2010) and the LOFAR survey (radio), have provided researchers with vast amounts of observational data across the electromagnetic spectrum to study star formation on a range of scales.

Individual stars are unresolved in all but the closest galaxies, therefore SFRs must be determined using integrated light measurements from observations of galaxies. There are many different direct and indirect observational tracers of star formation across the electromagnetic spectrum; examples include the Hα recombination line in the optical, UV, X-ray, IR and the radio continuum (RC). The rate of star formation is measured by probing the energy emission of the young stellar population in the galaxy, which is dominated by massive stars, meaning that each tracer is essentially measuring the rate of massive star formation. However, each of these tracers are probing star formation over different timescales. Ideally, a tracer that probes the presence of the short-lived, massive stars is preferable over one that probes longer timescales, as this can lead to emission contamination from older stars. The shorter the timescale, the lower the dependence the SFR indicator will have on the evolution of the stellar population.

The SFR indicators have been extensively reviewed over the past two decades. Kennicutt (1998) reviewed the diagnostic methods used to measure SFRs, and also presents a set of SFR calibrations. The focus of the review is to understand the broad patterns in the star formation properties along the Hubble sequence. This is done by investigating the correlation between the physical nature of the Hubble sequence and galaxy SFRs. SFRs are key probes of galaxy evolution, so if we understand their evolutionary histories this will also shed light on the physical processes that drive it. Kennicutt & Evans (2012) review the progress of star formation studies and the methods developed for measuring SFRs over the following decade, followed most recently by Madau & Dickinson (2014) who recap the points relevant for measurements of the global star formation history, particularly at high redshift. This chapter summarises the variety of SFR indicators, how they trace star formation and their limitations.

3.3.1   Ultraviolet (UV) continuum

The wavelength range of 1250 - 2500 Å in the UV end of the spectrum is dominated by young stars, which implies the luminosity scales linearly with the SFR. Young stars of several solar masses (e.g. OB stars) emit the bulk of their energy in this region, making it a direct tracer of star formation in the galaxy (Kennicutt 1998; Kennicutt & Evans 2012). The lifetime of a B8 star is ~ 350 Myr, and for every 150 of these there exists a much brighter O6 star with a lifetime of ~ 6 Myr (Calzetti, 2013). Consequently, the UV traces star formation over timescales of $10 - 350$ Myr. The 1250 - 2500 Å wavelength interval is only accessible using optical ground based telescopes for galaxies with redshifted spectra $z > 1$, which makes it ideal for probing the early histories of galaxy evolution. Using this technique on dusty galaxies is problematic as this UV interval is very sensitive to extinction. Calibrating the extinction correction may be possible, however it comes with a lot of inaccuracies (Calzetti et al. 1994; Kennicutt 1998).

Ultraviolet continuum measurements were revolutionised in 2005 by the launch of the Galaxy Evolution Explorer (GALEX) mission (Martin et al., 2005), which imaged two thirds of the sky in the far and near UV, providing integrated UV fluxes and SFRs for hundreds of thousands of galaxies. It was able to detect star formation at low surface brightness and intensities across a wide range of galactic environments. This vast amount of new data provided by GALEX enabled deeper studies of the interstellar dust attenuation problem

and new calibrations were determined with reduced uncertainties (e.g. Seibert et al. 2005; Johnson et al. 2007; Hao et al. 2011).

3.3.2 Hα recombination line

Nebular emission lines are another way of probing the SFRs of galaxies. Young stars with masses greater than 10 $M_\odot$ produce UV photons with energies capable of ionising the surrounding gas (Kennicutt & Evans, 2012). The absorbed energy is re-emitted in the optical wavelength range and form recombination lines in the spectrum of galaxies. The strongest of these nebular lines can be used to directly probe the massive stars with lifetimes shorter than 20 Myr, therefore providing a nearly instantaneous measure of recent star formation. As such, ionising photon tracers are desirable although factors such as the leakage of the ionising photons from the young stellar population must be taken into account. The most reliable SFR emission line indicator is Hα (Moustakas et al., 2006). Other recombination lines include: Hβ, Pα, Pβ, Brα and Brγ. The scaling of the ionising flux to SFR has been computed using an evolutionary synthesis model. Using solar abundances and a Salpeter IMF (Salpeter, 1955) of 0.1-100 $M_\odot$, the calibrations of Kennicutt et al. (1994) and Madau et al. (1998) yield:

$$\mathrm{SFR}(\mathrm{M}_\odot \mathrm{yr}^{-1}) = 7.9 \times 10^{-42} \ \mathrm{L}_{\mathrm{H}\alpha}(\mathrm{ergs \ s}^{-1}) \tag{3}$$

The Hα luminosity is computed using the Case B recombination (Burgess, 1958). The benefit of using this method is the direct relation between the emission line flux and the SFR of the massive stellar population. The Hα line is strong and can be easily detected in the redshifted spectra of starburst galaxies beyond $z = 2$ if the wavelength coverage is large enough. The drawbacks of this method are the uncertainties in the extinction and the IMF, although Hα is emitted at 6564 Å, so will at least suffer less extinction than the UV region (assuming the UV source and the nebular emission is co-located). The extinction in the Hα line can be corrected using the known line ratio of Hα/Hβ, which for Case B is 2.86 (Burgess, 1958). Another limitation is the escape fraction of the ionising photons which are not observed and accounted for in the calculation. There are numerous studies which attempt to quantify this escape fraction using Lyα fluxes of galaxies (e.g. Blanc et al. 2011; Hayes et al. 2011; Leitet et al. 2013), each with very different percentages and large uncertainties.

3.3.3 Far-infrared (FIR) continuum

The UV emission which is intercepted by interstellar dust and re-emitted in thermal FIR (10-300 μm) makes up a large proportion of a galaxy's bolometric luminosity (Kennicutt, 1998). This makes the FIR a sensitive tracer of the young stellar population and, subsequently, the SFR. The IR probes stellar populations with a range of ages, therefore the timescale over which it traces the star formation will depend on the dominant stellar population which is contributing towards the IR emission (Calzetti, 2013). Interstellar dust absorbs approximately half the stellar emission in the universe and re-emits it in the infrared (Kennicutt & Evans, 2012), therefore IR derived SFRs are vital in order to trace all star formation within the galaxy. The Spitzer Space Telescope (Werner et al., 2004), the Herschel Space

Observatory (Pilbratt et al., 2010) and the Wide-field Infrared Survey Explorer (WISE) mission (Wright et al., 2010) are a few of the missions which have significantly impacted star formation research using IR observations.

The reliability of this SFR indicator depends on the contribution of young stars that heat the dust and the optical depth of the dust in the star-forming regions. An ideal situation would be a stellar population where the UV radiation is dominated by young stars and the dust opacity is high. In reality, for most normal galaxies, it is not that simple, as the FIR continuum is made up of another component which is associated with the dust heated by the interstellar radiation field (Cox & Mezger, 1989). In optically blue galaxies this component is dominated by the young stars, however in red galaxies the contamination of dust heating by older stars can have a considerable impact. Therefore there is no FIR emission to SFR calibration which applies to all types of galaxies, it is best to only use the FIR as a measure for circumnuclear starburst galaxies (starburst surrounded by high opacity dust) (Kennicutt & Evans, 2012).

3.3.4   Radio continuum (RC)

The radio continuum star formation rate (RC-SFR) relation of normal star-forming galaxies has been regularly reviewed and studied over the past few decades (Condon 1992; Murphy et al. 2011; Heesen et al. 2014). RC emission can be used as a star formation tracer as it stems from massive stars. HII regions are formed around massive stars which emit ionising UV radiation, this gives rise to RC radiation via thermal free-free emission. Thermal free–free emission is the dominant emission mechanism in the 20–40 GHz range, therefore observing this frequency range is a direct way of probing star formation in galaxies (Condon 1992; Murphy et al. 2011).

When these stars reach the end of their relatively short life, they produce cosmic rays by accelerating electrons in supernovae explosions. Synchrotron emission is generated when these cosmic-ray electrons spiral around interstellar magnetic field lines (Bell, 1978). Since the supernova rate is directly proportional to the SFR, we can measure the luminosity of this synchrotron emission as a proxy for the SFR. This non-thermal emission is an indirect way of probing the star formation, dominating at frequencies lower than 5 GHz; LOFAR 150 MHz detects the synchrotron emission with less contamination from thermal emission than at GHz frequencies (Heesen et al., 2014).

RC is not affected by dust attenuation, which makes it a more desirable SFR tracer than those at UV or optical wavelengths (Madau & Dickinson, 2014). The thermal component of the RC spectrum is relatively spectrally flat and steepens at the non-thermal, lower frequency end of the spectrum (Kennicutt & Evans, 2012). The RC spectrum scales with the luminosity of the ionising emission. A photoionisation related measure of the SFR can be derived using the free-free component of the RC, which does not involve complications from dust extinction. An indirect relationship between the RC synchrotron emission component and SFR is derived using a tight correlation between this emission and the FIR emission of galaxies (Helou et al., 1985; Condon, 1992). The steep non-thermal synchrotron spectrum in the RC makes the RC-IR correlation wavelength dependent. The correlation remains nearly linear over the entire luminosity range, despite the fact the IR becomes a poor tracer of star formation in faint galaxies with low dust content. Bell (2003) addresses this issue which

argues that this tight, nearly linear RC-IR correlation is a conspiracy: both the IR and radio luminosities of dwarf galaxies significantly underestimate the SFR as the low dust content in low-mass galaxies is accompanied by a decline in synchrotron emission. SFR calibrations which take into account this effect are presented in Bell (2003).

Tabatabaei et al. (2017) studied the spectral energy distribution (SED) of the RC emission and found an even tighter agreement using the bolometric luminosity of the mid-radio continuum (MRC) (1-10 GHz). They compared the RC and IR SEDs and found that the RC-IR is a non-linear function of the SFR. The FIR/MRC ratio decreases with SFR due to the amplification of magnetic fields in star-forming regions, hence the ratio is lower at higher redshifts, where mostly star-forming galaxies are detected. The new correlation between the MRC and the SFR along with improvements to the Expanded Very Large Array (EVLA) (Condon et al. 1998; Perley et al. 2009) and other instruments make the RC a more popular, reliable means of determining SFRs in high redshift galaxies. Further studies of the RC-SFR relation have been made possible with LOFAR (van Haarlem et al., 2013). Gürkan et al. (2018) studied the RC-SFR at low radio frequencies in order to observe radio continuum which is completely dominated by the non-thermal radiation. The Herschel-ATLAS project (Eales et al., 2010) surveyed an eighth of the sky in the infrared, detecting 400,000 galaxies up to redshifts of 6 across all the maps. The Herschel-ATLAS North Galactic Pole (NGP) field was surveyed along with LOFAR at an observing frequency of 150 MHz for local galaxies, as part of the LOFAR Surveys Key Science project (Hardcastle et al., 2016). SFRs were derived using a combination of the optical data from the SDSS sample, IR data from Herschel-ATLAS and WISE and the radio data from the LOFAR survey (Gürkan et al., 2018). This enabled a detailed study of the low-frequency RC-SFR relation in the nearby universe from which a broken power-law relationship between the 150 MHz radio luminosity and the SFR was found for star-forming galaxies.

This thesis will compare SFRs derived from simulated 150 MHz LOFAR measurements and from Hα fluxes measured from the simulated OPR3 spectra for star-forming galaxies. Hα derived SFRs are the most reliable among other indicators and optical emission line tracers (e.g. Moustakas et al. 2006) and can therefore be used to gauge how representative the 150 MHz derived SFRs are of the galaxies true SFR. As previously mentioned, if RC measurements are proved to reliably estimate SFRs it would be very beneficial to star formation research. Surveys such as LOFAR are highly sensitive to RC synchrotron emission, they are impervious to dust and can survey the sky very fast.

4 Building an algorithm to model and fit the OPR3 spectra

The primary goal of my project is to write an algorithm which will be able to model WEAVE-LOFAR spectra. The four primary emission lines I will be fitting which are required for the BPT-NII diagram and the SFR(Hα) derivations are: [NII] $\lambda/6584$ Å, Hα $\lambda/6564$ Å, [OIII] $\lambda/5007$ Å and Hβ 4861 Å. I will henceforth be referring to these lines as: NII-2, Hα, OIII-2 and Hβ respectively. WEAVE-LOFAR will have a data flow of 950 spectra per hour, therefore one of the requirements for my algorithm is that it can be used universally for any

spectral type with little, if any, interaction required. Hence, I must consider all possible factors which need to be taken into consideration by the algorithm; line blending, modelling the continuum, dust extinction and the broad line component.

4.1   Further emission lines required for modelling

NII-2 appears as a doublet alongside [NII] $\lambda/6548$ Å (hereafter, NII-1), these two emission lines surround the Hα line and, in the case of the OPR3 spectra, blend with it. Because of this close proximity, which is demonstrated in Fig.4a, NII-1 must be modelled by my algorithm as well. The area within a spectrum containing these three lines will hereafter be referred to as the Hα region.
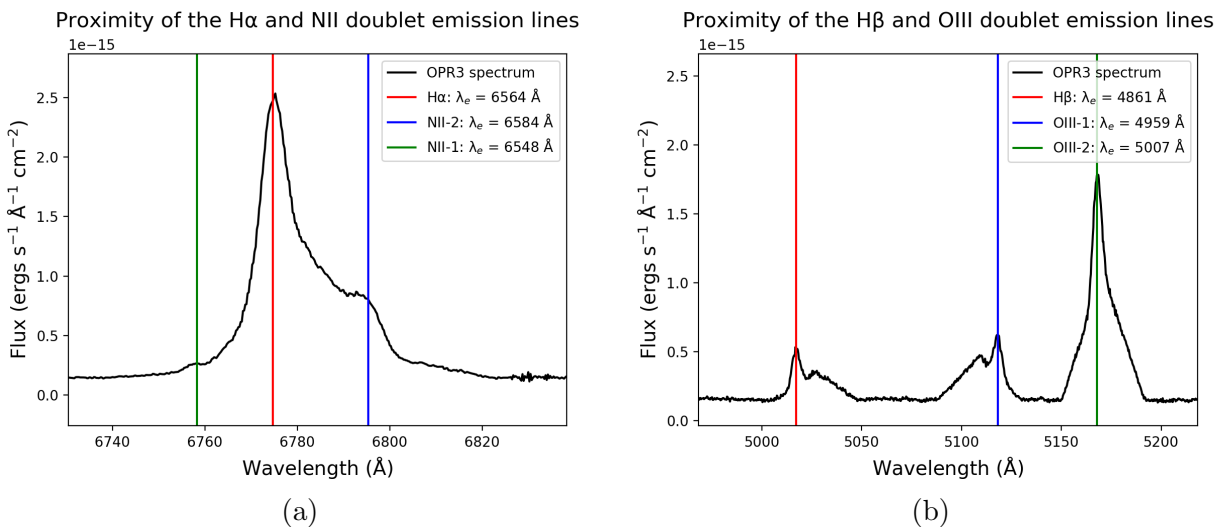
Figure 4: OPR3 spectrum of a star-forming emission line galaxy with a redshift of $z = 0.032$ and a high SNR of 28.6. Fig.4a: The green vertical line indicates the observed frame of NII-1, the red shows Hα and the blue NII-2. The lines in the Hα region are blended. All other structures in this area contaminating the emission lines flux or in close proximity must be modelled alongside Hα and NII-2. Fig.4b: The green vertical line shows the location of the OIII-2 redshifted wavelength, the red for Hβ and the blue for OIII-1. The lines in the Hβ region are unblended. All other structures, for instance the continuum, in this region will be modelled alongside Hβ and OIII-2. The nature of the broad components is discussed in section 7.2.

OIII-2 forms a doublet with [OIII] $\lambda/4959$ Å (hereafter, OIII-1), which falls between Hβ and OIII-2. Fig.4b demonstrates the proximity of these three lines. It is possible to mask this line out however it would be risking the, albeit unlikely, event of also masking out emission from its neighbouring lines. Modelling more lines will also increase the number of parameters the fitting algorithm has to handle; however, it is beneficial to do so in order to get a better estimation of the velocity dispersion and velocity offset of the source. It will be harder for the fitting algorithm to determine these two parameters using the blended emission lines from the Hα region, therefore it will most likely depend on the three unblended lines in the

Hβ region to determine their best estimates and obtain the most representative uncertainties (assuming all the lines have the same velocity dispersion).

4.2   Function and parameters

In this section I present the functions which will be used to model and subtract the continuum and fit the specified emission lines of the OPR3 sample.

4.2.1   Modelling emission line profiles

The profile of emission lines are best modelled by a Gaussian function:

$$f(x) = a \times \exp\left(-\frac{(x - \mu)^2}{2\sigma^2} \right) \tag{4}$$

There are three main Gaussian parameters for spectral lines; the line centre (μ), the width (σ) and the normalisation parameter (a). Radiation is emitted from a source when an electron within an excited atom or molecule loses energy and falls to a lower energy level. The wavelength of the emitted radiation is well known in atomic physics, hence these lines can be located in the spectrum of the source. Since the line centres are known, μ will be modelled as a fixed constant for Eq.4.

The line profiles are Gaussian, as opposed to a sharp peak, due to the internal velocity dispersion (σ_v) of the source resulting in a normal probability distribution of the emitted radiation around the line centre. The source of the emission will originate from an ionised gas or plasma such as an HII region, molecular gas cloud or a diffuse gas cloud. The ionising photons will have come from massive stellar objects in a star-forming region and/or an AGN. The internal σ_v of the gas can reach up to 500 km s^{-1} or even more in some sources (York et al., 2000). The observed frame width (σ) of the line profile is determined by σ_v; it is converted using Eq.5, where λ_e is the emitted wavelength, c is the speed of light in km s^{-1} and z is the redshift.

$$\sigma = \left(\lambda_\mathrm{e} \times \frac{\sigma_\mathrm{v}}{c} \right) \times (1 + z) \tag{5}$$

The velocity offset (v) models the relative difference in velocity between the source of the continuum and the narrow emission lines. If the redshift is derived using the continuum, then the observed wavelength centres of the lines will not correspond with the known redshifted emission wavelengths; therefore, v is required to model this offset. Fig.5 illustrates four example spectra where the known emission line wavelengths align with the peaks of the rest-frame line profiles. It is evident that their redshifts (z) have been derived using observed emission line ratios, hence any offset will most likely be included in these factors. The redshifts affect the location of the line centre, which shifts the line centres by a factor of $z + 1$. The redshifts have been estimated using a method prior to the spectral fitting of the OPR3 spectra, and I am provided with the these factors so it is not necessary to tackle this problem in my project and so the model assumes that the redshifts are known. Visual inspection is not a reliable source of evidence that the redshifts encompass the velocity offset

between the continuum and the emission lines sources. Therefore, I will treat v as a free parameter and review how closely the mean posterior estimates of the velocity offsets fall within 0 km s^{-1}. The observed wavelength (μ) is calculated using the emitted wavelength (λ_e) and the velocity offset in Eq.6. The velocity offset of the broad lines are discussed in the section 4.2.3.

$$\mu = \lambda_e \times \left(1 + \frac{v}{c}\right) \times (1 + z) \tag{6}$$
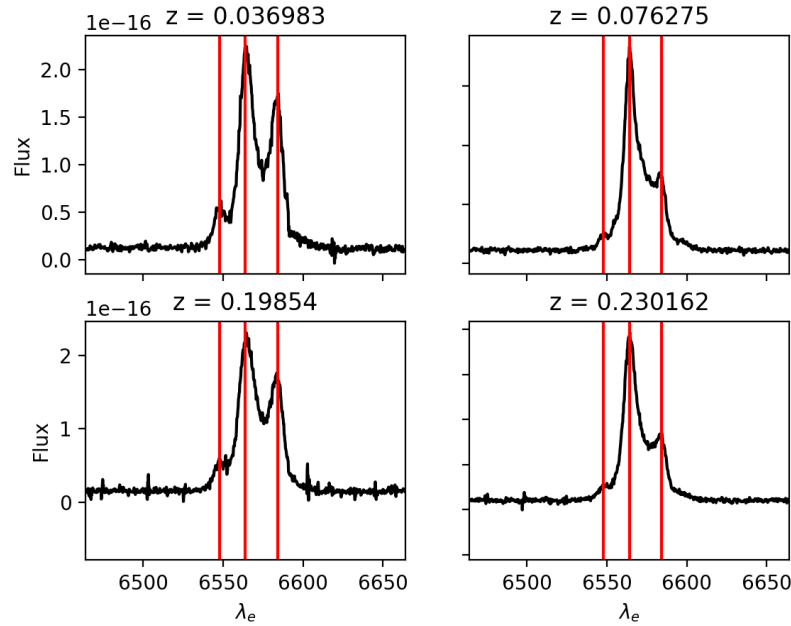
(a) Rest-frame spectra centred on the Hα region for OPR3 spectra with a range of z.
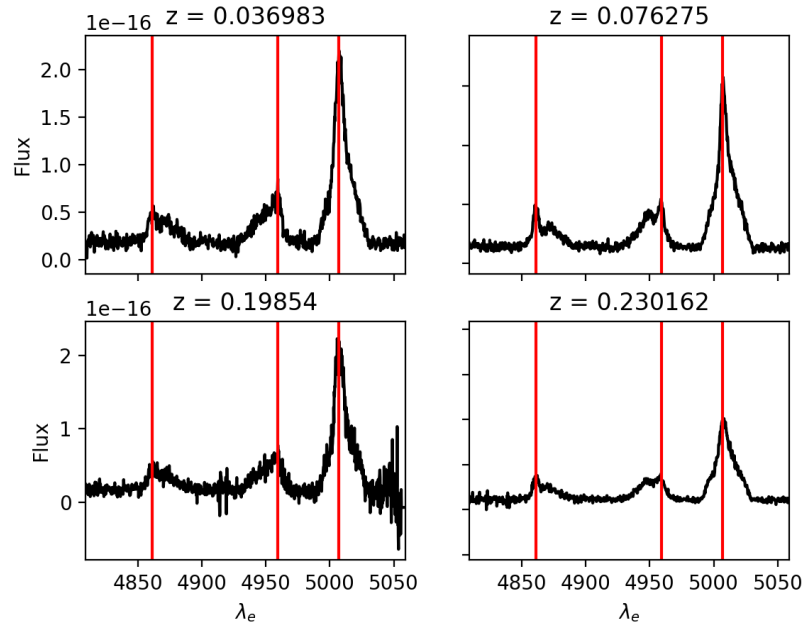
(b) Rest-frame spectra centred on the Hβ region for the same OPR3 spectra as Fig.5a.

Figure 5: The vertical red lines indicate the known emission wavelength (λ_e) of the lines. From left to right in Fig.5a: NII-1 $\lambda/6548$ Å, Hα $\lambda/6564$ Å and NII-2 $\lambda/6584$ Å. From left to right in Fig.5b: Hβ $\lambda/4861$ Å, OIII-1 $\lambda/4959$ Å and OIII-2 $\lambda/5007$ Å. Each vertical red line aligns with the peak of the narrow line component profile, indicating that the velocity offset is accounted for in the redshift. The nature of the broad components which blend with each narrow emission line are discussed in section 7.2.

The final unknown variable is the peak flux of the lines, which adds an additional free parameter for each of the emission lines Gaussian profiles. It is important to keep the number of parameters to a minimum in order to obtain the best estimates within a reasonable time frame. WEAVE will output an average of 950 spectra within an hour, therefore the algorithm must be able to process the same quantity of spectra within a reasonable time frame. The time can be reduced by parallelising the processing, however this is still limited by the availability of resources. Additionally, there is an upper limit to the number of parameters which fitting algorithms are capable of handling, as explained in section 4.4.

4.2.2   Continuum profile

A Gaussian asymptotes the x-axis, however a galaxy's spectrum does not as it contains flux arising from a multitude of sources other than emission lines. The continuum is made up of a combination of stellar black body spectra spanning a range of temperatures. The continuum needs to be modelled, fit and subtracted from the spectrum before fitting the Gaussian profiles to the lines. There are a number of steps involved in this process. In cases where one is only interested in measuring a redshift, and not the line fluxes, it is acceptable to isolate emission lines and model the surrounding continuum as a smooth curve. This can be done using methods described by e.g. Schreiber 2019. Subtracting a fitted smooth curve to the continuum will not adequately reduce the flux surrounding the emission lines to zero, and will often leave behind strong, non-Gaussian features, therefore it cannot be used when measuring the line fluxes. It also means that any information held in the continuum cannot be measured. Instead, I will use MCMC techniques to fit high-quality synthetic templates to the continuum in an attempt to remove all the continuum flux.

The OPR3 simulation used templates based on the synthetic spectra of BC03 (Bruzual & Charlot, 2003). There are 13 templates with a solar metallicity which correspond to 10 instantaneous-burst models with ages of 0.005, 0.025, 0.10, 0.29, 0.64, 0.90, 1.4, 2.5, 5 and 11 Gyr; a constant star formation model with an age of 6 Gyr; and two models with exponentially declining star formation histories with timescales of 5 Gyr and 9 Gr and an age of 12 Gyr. Fig.6 plots these templates within the WEAVE wavelength range with a redshift of $z = 0$. The templates are normalised to $F_\lambda(5500 \text{ Å}) = 1$.

Stellar population models provide the integrated properties of model galaxies as a function of physical parameters such as star formation history, metallicity and the IMF. These models can be used to construct model spectral energy distributions and spectra, which in turn can be used to interpret the light of galaxies and from that infer the real properties of its stellar population (Maraston, 2007). Simple stellar population (ssp) models are named as such due to the simplicity of its assumptions. An ssp models the evolution of a stellar population which consists of stars born at the same time with the same initial chemical composition (Maraston, 2003). Stars of different masses in this population, which are implemented using the IMF, will follow different evolutionary tracks however they will all start at the same point in time. Consequently, the stars in a ssp model can be located along an isochrone in a Hertzsprung-Russel diagram (Maraston, 2003). The benefit of using a ssp is its simplicity, however a galaxies stellar population is far more complex.
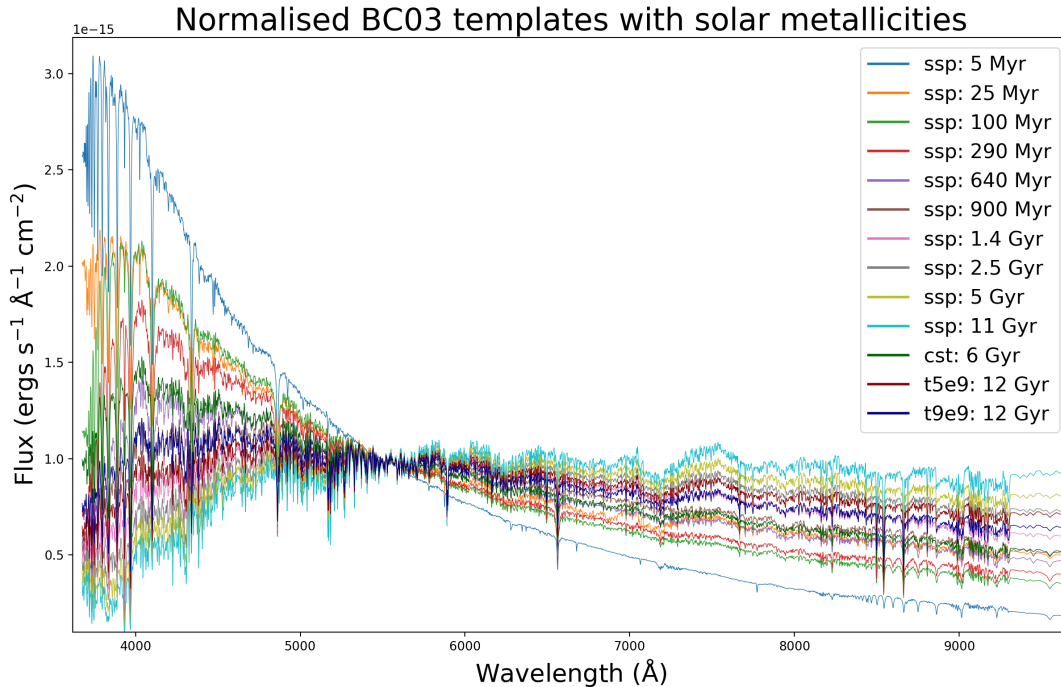
Figure 6: Normalised BC03 templates which have a solar metallicity ($F_\lambda(5500 \text{ Å}) = 1$). The 10 instantaneous-burst models, or Simple Stellar Populations (ssp), become redder with age. The two models with exponentially declining star formation histories of 5 Gyr (t5e9) and the bluer 9 Gyr (t9e9) have ages of 12 Gyr and are both bluer compared to the ssp: 11 Gyr model. The final constant star formation model with an age of 6 Gyr is denoted by cst: 6 Gyr.

These templates are overlaid with an OPR3 spectrum with $z = 0.024$, SNR = 72.72 and SNR(Hα) = 91.87 in Fig.7. Where the SNR is the average ratio of the flux over the noise for the entire wavelength range of the blue and red spectra combined, and the SNR(Hα) calculates the average over the wavelength range in the Hα region (the wavelength range of this region is defined in section 5.2). I have highlighted the location of the Hα peak to demonstrate the absorption features in the continuum. There are very clear prominent structures in the continuum which can only be removed by modelling it with these templates.

A dust attenuation curve must be applied to the templates in order to properly model the continuum in the attenuated OPR3 spectra. Dust attenuation describes the absorption and scattering of emission from a galaxy due to the presence of dust and the implications this has on its spectrum (Salim & Narayanan, 2020). Whereas extinction describes the effects of foreground dust on a single star, attenuation refers to more complex geometrical cases such as dusty galaxies, starburst galaxies or stars with circumstellar dust. Unlike extinction, attenuation is not directly proportional to the quantity of dust in a system, therefore the shape of the attenuation curve will vary with the amount of dust. I used the Calzetti et al. (2000) reddening law for starburst galaxies which I applied to the templates using Eq.7, 8 and 9.
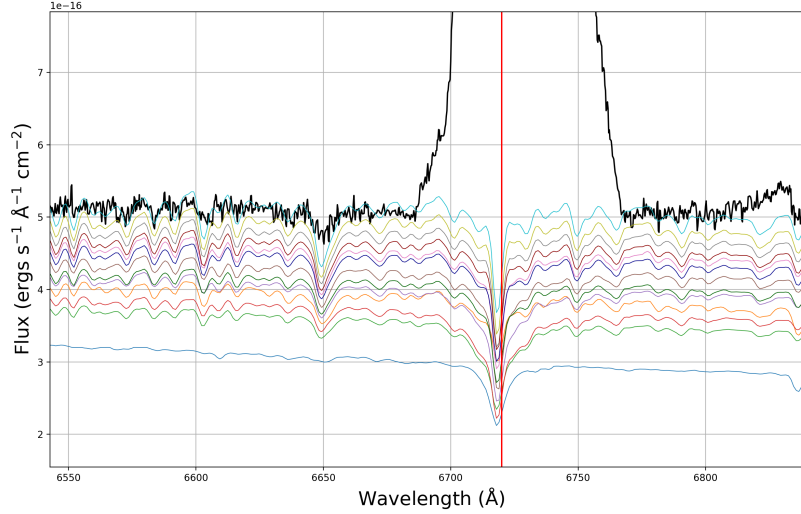
Figure 7: Hα region of an OPR3 spectrum (black line) with $z = 0.024$ and all 13 BC03 templates redshifted and overlaid with a flux offset for comparison. The red vertical red line indicates the redshifted location of the Hα emission line. The SNR of this region is 91.87 and the SNR of the entire spectrum is 72.72. Such a high SNR suggests that any non-Gaussian features in the spectrum are absorption and emission features in the continuum. These continuum features must be modelled and adequately subtracted to get the best estimate for the flux of the emission lines. The shape of the continuum, unlike the templates, has been affected by extinction due to dust; this must be modelled with the template.

$$f_{obs}(\lambda) = f_{int}(\lambda)10^{-0.4A_\lambda} \tag{7}$$

$$A_\lambda = k(\lambda)E(B - V) = \frac{k(\lambda)A_v}{R_V} \tag{8}$$

$$k(\lambda) = \begin{cases} 2.659(-2.156 + \frac{1.509}{\lambda} - \frac{0.198}{\lambda^2} + \frac{0.011}{\lambda^3}) + R_V, & 0.12\ \mu\text{m} <\lambda<0.63\ \mu\text{m} \\ 2.659(-1.857 + \frac{1.040}{\lambda} + R_V, & 0.63\ \mu\text{m} <\lambda<2.20\ \mu\text{m} \end{cases} \tag{9}$$

Where f_{obs} is the observed flux, f_{int} is the initial flux before reddening, A_λ is the total extinction, A_v is the total extinction in the v band, k is the reddening law by Calzetti et al. (2000) and R_V is the effective total obscuration at v.

As shown in Fig.8, A_v significantly influences the shape of the spectrum. A_v must be greater than 0 as a negative extinction would mean the dust is contributing towards the flux in the optical instead of absorbing the emission. The extinction curve will be parametrised with the only unknown variable: the total extinction (A_v). There will also be a normalisation parameter for the scaling of the template; however, it is not possible to recover this value as there is another normalisation parameter for the blue and red spectra which accounts for
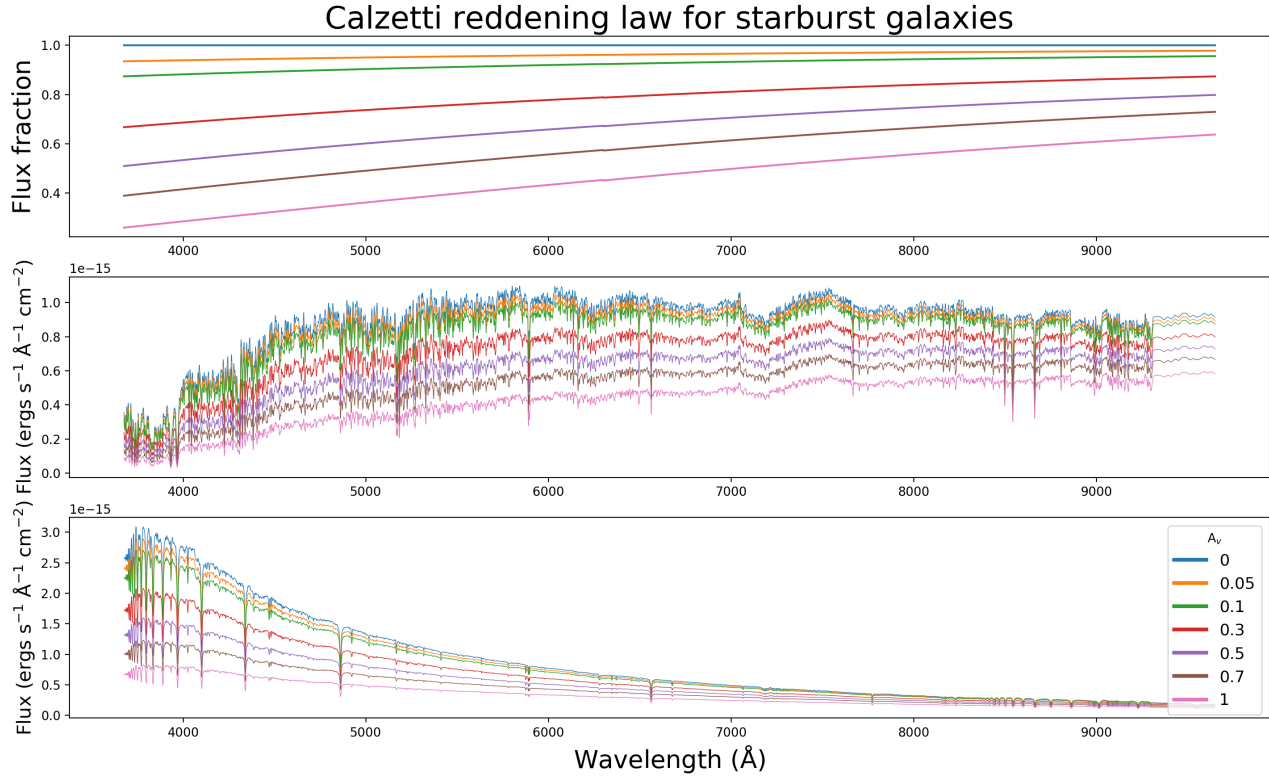
Figure 8: The Calzetti dust law, as shown in Eq.7, is represented in the above plots. The first plot shows how A_v magnitudes between 0 and 1 impact the flux as a function of wavelength; this is represented as a fraction of the original flux. As A_v increases, the original flat line becomes attenuated towards the blue end. The effect this has on the continuum templates is demonstrated in the second and third plots of ssp: 11 Gyr (the longest age model) and ssp: 5 Myr (the shortest age model) respectively.

the calibration offset between the two arms. This calibration offset is explained in section 5.4.

$$N_b = S_t \times S_{cb} \tag{10}$$

$$N_r = S_t \times S_{cr} \tag{11}$$

Eq.10 and Eq.11 are the equations for the normalisation parameters. Where N_b and N_r represent the combination of the template scaling factor, S_t, and the calibration offset corrections, S_{cb} and S_{cr} in the blue and red arms respectively. The offset caused by this suspected calibration issue must be corrected before fitting the lines, as it is necessary that the blue and red spectra align and their line fluxes must be representative of the true, dust attenuated emission from the galaxy. The fitting algorithm will only be able to retrieve estimates for a combination of the template scaling and the calibration offset correction, as demonstrated by Eq.10 and Eq.11. I will, however, be able to obtain a measurement for the calibration correction ratio of S_{cb} and S_{cr}, which I can use to scale the blue spectrum in order to align it with the red. The decision to correct the blue spectrum comes from an assumption

that it is the calibration of the flux in this arm exclusively causing the offset. The blue end of the spectrum is most sensitive to high temperatures, which is a potential reason for the offset when using the spectrum of white dwarfs to flux calibrate the galaxy's spectrum. A possible implication of doing this is that it removes the calibration of the flux in the blue spectrum and it may still not be representative of the true input flux. Other implications will become clearer when I obtain estimates for the calibration scaling ratios and I can analysis their distributions. If the blue spectrum is scaled incorrectly, then the integrated flux of the emission lines will not be comparable to the true input values. Consequently, I will be unable to correct for dust extinction in the Hα line using the Balmer decrement for galaxies with a redshift which places the Hβ region within the wavelength range of the blue arm. The line flux ratios required for the BPT-NII diagram will still be usable as the integrated flux ratios will not be affected by the calibration offset. The lines used in each of the ratios are so close in wavelength that the overall calibration is not important, it just needs to be smooth.

To normalise the template and model the extinction following the Calzetti law, I used Eq.12 and Eq.13 where C$_b$ and C$_r$ is the attenuated continuum for the blue and red arm respectively and T represents the selected BC03 template. The template which results in the best-fit will be used along with its mean Bayesian estimated parameters to subtract the continuum. This will be determined by whichever template results in a χ^2_ν closest to 1. The χ^2_ν is a statistic which is further expanded upon in section 5.7.

$$C_b(\lambda) = N_b \times T(\lambda)10^{-0.4A_\lambda} \tag{12}$$

$$C_r(\lambda) = N_t \times T(\lambda)10^{-0.4A_\lambda} \tag{13}$$

4.2.3 Broad line components

There are features which accompany each of the emission lines in the OPR3 spectra which were originally identified as broader emission lines with a velocity offset from their narrow counterparts. The origin of these broad components are unknown, as the simulation was not expected to produce them. In a real spectrum, the broad and narrow components would originate from different sources within the galaxy which have similar chemical compositions but with different velocity dispersions. After further investigation I discerned that the broad component of each emission line appears to have a unique velocity offset relative to their narrow component which is consistent for every spectra in the OPR3 sample. This is demonstrated in Fig.9 which illustrates the rest-frame spectra of four different sources as well as Fig.10 which illustrates in detail the spectra of two high SNR galaxies. A constant velocity offset for each emission line is most convincing for the Hβ and OIII-1 lines as their broad and narrow line peaks are not blended. The velocity offsets of the broad lines relative to their narrow counterparts are estimated as follows: 555.44 km s^{-1} for Hβ, -544.46 km s^{-1} for OIII-1, 179.75 km s^{-1} for OIII-2, -229.08 km s^{-1} for NII-1, 319.93 km s^{-1} for Hα and 410.09 km s^{-1} for NII-2. This is functionally equivalent to assuming rest-frame wavelengths for the broad lines of Hβ λ/4870 Å, OIII-1 λ/4950 Å, OIII-2 λ/5010 Å, NII-1 λ/6543 Å, Hα λ/6571 Å and NII-2 λ/6593 Å.
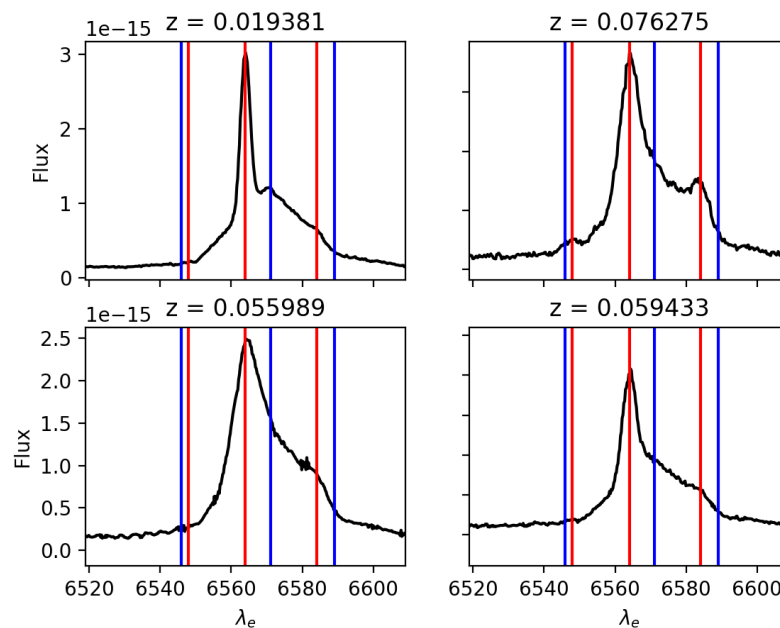
(a) Rest-frame Hα region for high SNR OPR3 spectra with a range of z values.
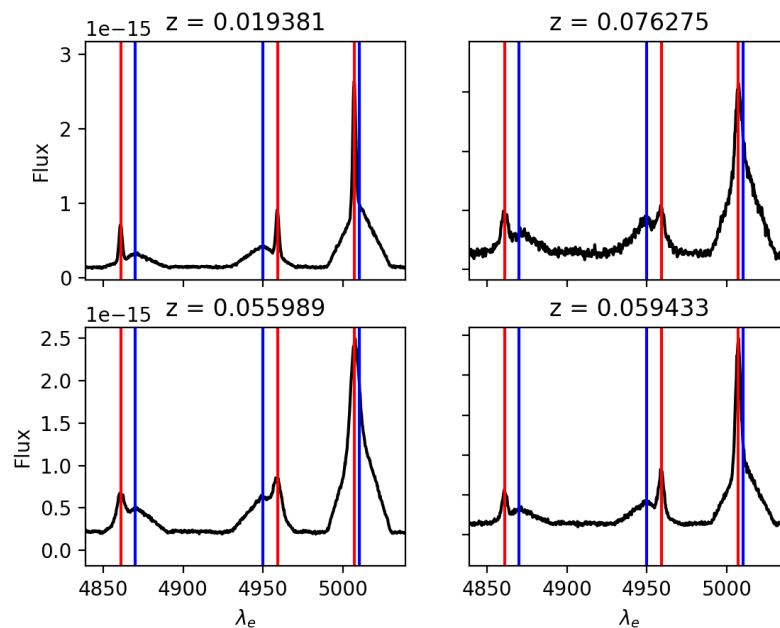
(b) Rest-frame Hβ region for the same OPR3 spectra as Fig.9a.

Figure 9: Example spectra showing the regions around Hα and Hβ in the rest-frame. The vertical red lines indicate where the emitted wavelength (λ_e) of the narrow emission lines are located. The blue vertical lines indicate where I have identified the peaks of their broad components.
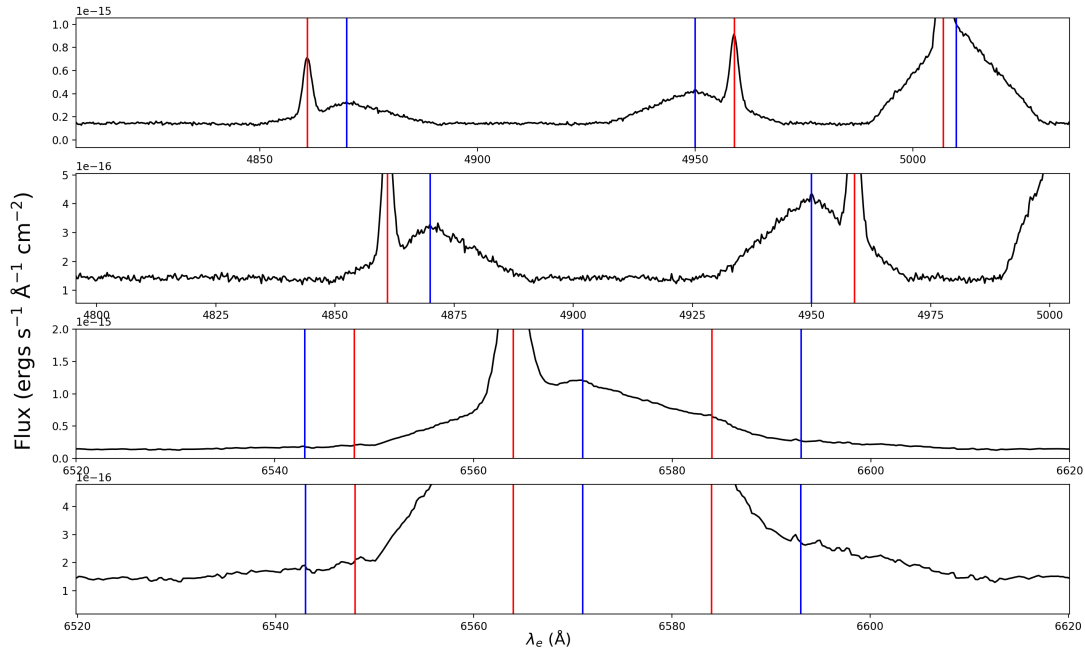
(a) Rest-frame Hα and Hβ regions for a high SNR OPR3 spectrum: $z = 0.019$, SNR(Hα) $= 47.71$, SNR(Hβ) $= 26.91$.
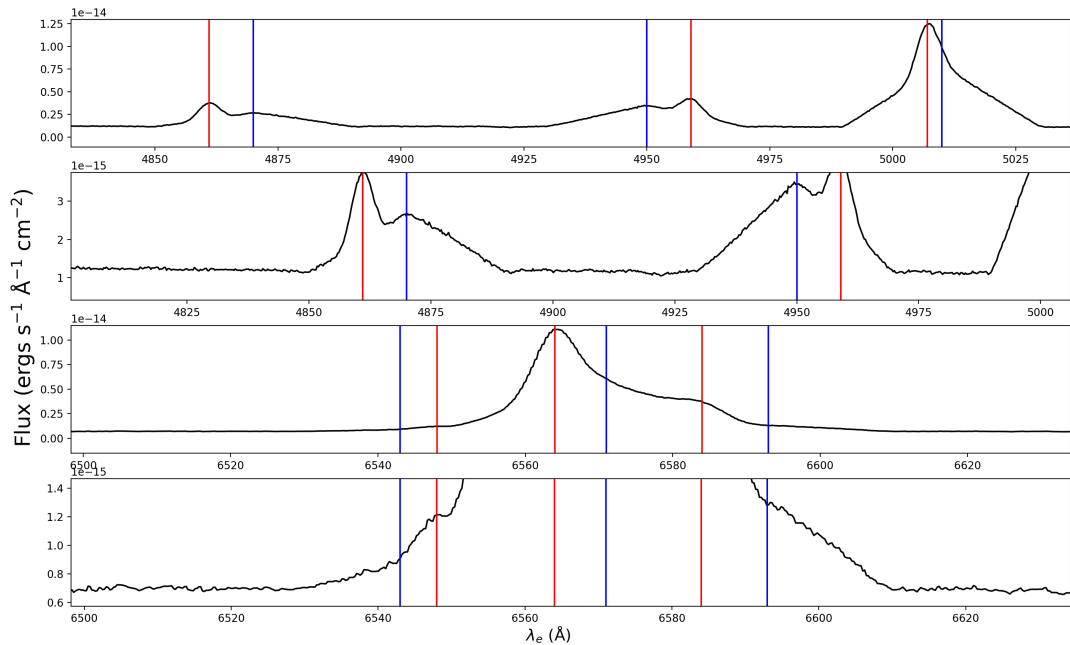
(b) Rest-frame Hα and Hβ regions for a high SNR OPR3 spectrum: $z = 0.012$, SNR(Hα) $= 102.31$, SNR(Hβ) $= 75.464$.

Figure 10: The upper plot in both Fig.10a&b show the Hβ region of high SNR spectra, the second plot highlights a lower flux range for the Hβ and OIII-1 lines, the third plot shows the Hα region and the final plot highlights a lower flux range for this region. The vertical red lines indicate where the emitted wavelength (λ_e) of the narrow emission lines are located and the blue vertical lines indicate where I have identified the peaks of the broad component.

Identifying the locations of the broad components in the Hβ region was straightforward as the peaks of the lines are clearly visible. However, the above emission wavelengths for the broad lines in the Hα region are poor visual estimates since all six lines are blended and it is not always possible to see the line peaks (with the exception of the Hα peak appearing in Fig.10a). Visual inspection is not a reliable method; therefore, the broad line Gaussian centres will contribute a further six free parameters and their heights, velocity dispersion and offset provide another eight. The values quoted for the broad lines centres will be used as the initial guesses in the fitting algorithm. It is clear, given the number of free parameters which now stands at 22, that this optimisation problem will require a sophisticated fitting algorithm that can handle high dimensionality.

The nature and origin of these broad lines became clear further along in the fitting process where I discovered they are non-Gaussian structures. Their true profile is discussed in section 7.1 along with how I ultimately decided to model them. It should be noted at this point that these are nuisance structures as their integrated flux is proven to hold no information about the galaxy, and the only purpose of modelling them is to remove them from their narrow counterparts. As such, they will henceforth be defined by their estimated rest-frame wavelengths as stated in this chapter.

4.3   Simultaneous fitting

The parameters and functions I have discussed so far make up a model for the OPR3 spectra. The narrow components of each emission line are in very close proximity to its broad counterpart, with the most severe case in the Hα region where all six narrow and broad lines are blended together due to the broad Hα component which has a large signal. This makes the option of modelling individual lines, or even narrow and broad pairs together, in this region impossible. There are many benefits to modelling lines individually; fewer parameters, reduced dimensionality, simpler fitting algorithms, reduced parameter uncertainty and less demand on CPU time and resources. Fitting the Hα and Hβ regions separately would reduce the complexity of the problem; unfortunately, there are a few factors which make this impractical. The line width is the main issue: this should be consistent for all the emission lines originating from the same source and fits to individual unblended emission lines should all output the same width. The line width of the narrow emission lines in the Hα region is prone to be overestimated as the surrounding foreign signal from the broad lines may be mistakenly modelled as part of their emission. In order to influence and constrain the estimation of this parameter towards its true value, the Hα region must be modelled alongside the Hβ region. The three emission lines in this region are only blended with their broad components, and are more likely to result in a width estimation which is more representative of the true value. The continuum, however, can be modelled and removed before modelling the lines, and not simultaneously. Modelling the continuum on the blue and red spectra together is necessary as their flux originates from the same target and therefore A_v and S_t must be the same for both the spectra.

4.4   Fitting algorithms

I initially attempted to fit my model to the OPR3 spectra using 'LMFIT', a module in Python which allowed me to use the Levenberg–Marquardt (LM) algorithm (Newville et al., 2014). This algorithm was developed to solve nonlinear least squares problems, which is done by fitting a nonlinear parameterised function to a set of data by minimising the sum of the squares of the errors between the data points and the function. A function is defined as linear if all the terms in the model are either a constant or a parameter multiplied by an independent variable, and any regression equation which does not follow these rules are classed as a nonlinear model. Hence, the functions used in my model for the OPR3 spectra are nonlinear.

In order to minimise the sum, the iterative algorithm uses a series of calculations to make updates to the parameters after each iteration. The LM fitting algorithm combines the gradient descent and the Gauss-Newton methods (Ranganathan, 2004). The gradient descent method updates the parameters in the steepest-descent direction, in other words the algorithm continues its search in the direction which will minimise the sum of the squared errors, given its current point. LM applies this method when the parameters are far from their optimal values, once it is within a closer proximity it selects the Gauss-Newton method as this is more accurate and faster when closer to the minimum error. The Gauss-Newton method reduces the sum by assuming the least squares function is locally quadratic, and finding the minimum of the quadratic.

LM is capable of handling models with multiple free parameters and is able to find the optimal solution even with a poor initial guess. However it is prone to get stuck in local minima of parameter space once there are more than a few fitted parameters. A key indicator of this is that the output will depend very sensitively on the initial guess. LM struggled to fit the OPR3 spectra using the model described in section 4.2, which has 22 parameters. Small adjustments to the initial guesses heavily influenced the output estimates. In multiple cases LM was able to estimate parameters which resulted in good χ_ν^2 values, however the estimates were not reproducible with, what should be, negligible perturbations to the initial guesses. Hence I concluded that my LMFIT results were unreliable and LM was not a suitable algorithm for this particular optimisation problem.

The Markov chain Monte Carlo (MCMC) method is much better suited to this optimisation problem. 'emcee' (Foreman-Mackey et al., 2013) is a Python implementation of the affine invariant ensemble sampler for MCMC proposed by Goodman & Weare (2010). MCMC methods are used to approximate the posterior distribution of a parameter by random sampling in a probabilistic space. In Bayesian statistics, the prior distribution represents our belief about a parameter before seeing the data and the likelihood distribution summarises the likeliness of different parameters to represent the observed data. Bayesian analysis combines both these distributions to determine the posterior distribution. The posterior is the probability distribution over the model parameters given the observed data and the priors. For instance, I can be certain that the width and the height of the Gaussian profiles which model the emission lines are positive values. In many cases the posterior distribution is impossible to solve analytically, this is where MCMC methods come in useful.

Monte Carlo simulations essentially using randomisation in order to estimate fixed parameters and can handle very complicated processes. Markov chains are sequences of events,

where each event comes from a set of outcomes and each outcome determines the next event, according to a fixed set of probabilities. All the information required in order to predict the next event is available from the previous outcome, in other words the chains have no memory. This is important as there are no underlying trends in spectra fitting, and therefore the probability of the next event occurring should be independent of prior events (van Ravenzwaaij et al., 2016).

MCMC will generate random values for a set of parameters and, given our prior beliefs, will determine how likely it is that each set of parameters can explain the data. If the chosen point in parameter space has a higher likelihood than the previous value it is added to the chain along with a statistic which describe how much better it is. Once the MCMC algorithm finds the local maximum likelihood point it doesn't remain there but instead samples the posterior as there is a finite probability of selecting lower probability values. Since the random samples are subject to fixed probabilities, they will eventually converge around a region of the best estimate for the parameter and form a posterior distribution. The posterior distribution will generally form a Gaussian centred around the best guess for the parameter. The best guess will henceforth be referred to as the posterior mean estimate. MCMC will be handling 22 parameters for the emission line fitting algorithm, and within this 22-dimensional probabilistic space there exist regions of higher probability where the parameters best explain the observed data, whilst also taking into account the prior knowledge.

5   Preparing the OPR3 data

The most significant step when preparing the spectra in the sample for the MCMC fitting procedure is to remove the continuum from the emission lines. There are many more procedures involved prior to this, these include: filtering high redshift spectra from the sample, masking spectral features, masking the wavelength range overlap of the two arms and setting up priors and initial guesses for the free parameters. This section also reviews the flux offset between the blue and red spectra, statistics of the OPR3 sample and how the algorithm will be tested for its reliability and reproducibility.

5.1   Filtering OPR3 spectra - redshift

There is a maximum redshift, z_m, after which NII-2 will no longer fall within the wavelength range of the red arm in the low resolution mode. This emission line has the longest emitted wavelength which is required for the BPT-NII diagram, therefore any OPR3 spectra with targets beyond z_m are excluded from my analysis. It is important to set the boundary low enough to account for the velocity dispersion of the source, which manifests in the data as the width of the lines, as it will widen the line profile beyond the observed wavelength. This will set the z_m low enough to avoid fitting only a segment of the true line profile. From visual inspection, I expect the velocity dispersion of the sources within the OPR3 simulation to be at most 500 km s^{-1}, hence I have set a sensible maximum of 1600 km s^{-1}, which should account for the true line broadening and provide sufficient continuum to ensure NII-2 is within the wavelength range of the red arm. z_m is calculated using Eq.14 and Fig.11 shows

the Hα region of the spectrum with the longest redshift in the sample after filtering for this boundary.

$$z_m = \frac{\lambda_m}{\lambda_e(1 + (\frac{\sigma_v}{c}))} - 1 \qquad (14)$$

- Maximum wavelength of the OPR3 spectrum: $\lambda_m = 9594$ Å

- Emission wavelength of the broad NII-2 line: $\lambda_e = 6593$ Å

- Maximum redshift: $z_m = 0.448$

I note that the spectra in my final sample were mistakenly not filtered using this method. Instead of defining z_m using the velocity in the rest-frame, I defined it in the observed frame using a redshifted fixed width, σ_f, of 35 Å. This is converted to σ_v using Eq.15 and substituted into Eq.14 to give Eq.16.

$$\sigma_v = \frac{\sigma_f}{\lambda_e} \times c \qquad (15)$$

$$z_m = \frac{\lambda_m}{\lambda_e + \sigma_f} - 1 \qquad (16)$$

The emission wavelength of NII-2 is constant for all the spectra, therefore the method I have used results in the same z_m of 0.448. It becomes more complicated in situations where boundaries are set for multiple emission lines with different λ_e. For example, spectra are filtered when the emission lines overlap with the two CCD chip gaps in Fig.12. Each of the emission lines have a different λ_e which means a fixed width should not be used to determine the redshift range of the overlap; it should change as a function of λ_e. The boundaries I set should be dependent on the emission lines emitted wavelength, and it should not be set as a constant upper/lower bound of $\pm 35 \times (1 + z)$ Å for all the lines in the observed spectrum. This will have an overall negligible effect on my sample size (± 10 spectra), and spectra with contaminated emission will be filtered from the sample as I ensured large upper limits were set for all boundaries.

There are physical gaps between the two CCD chips in each arm of the spectrograph which results in gaps within the spectra where WEAVE will be unable to capture photons. This gap falls between the wavelength ranges of 5482 and 5542 Å in the blue arm, and 7575 and 7676 Å in the red arm. Spectra with redshift values between 0.087 and 0.179 will not be used in my analysis as at least one of the required redshifted line wavelengths fall within range of these chip gaps. As described above, I set a maximum upper and lower bound of $\pm 35 \times (1 + z)$ Å on all the lines observed wavelengths to ensure all the emission is accounted for in the fitting along with a sufficient amount of continuum.
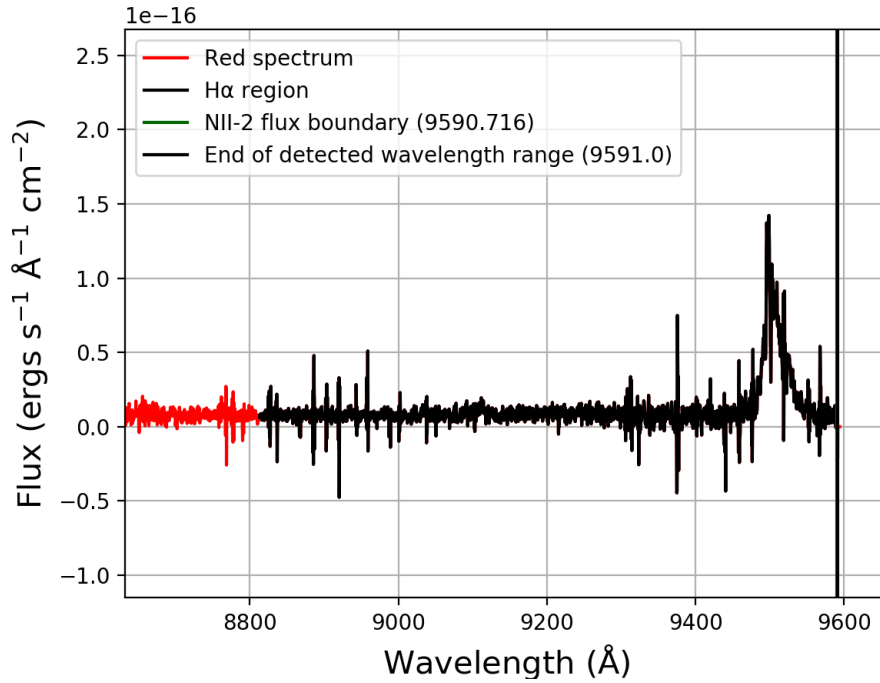
Figure 11: Spectrum with the largest redshift, $z = 0.447$, in the OPR3 sample where the NII-2 boundary of $(\lambda_e + 35) \times (1 + z)$ Å (green vertical line) is shorter than the longest detected wavelength in the red arm (black vertical line). The red line represents the red spectrum and the black represents the Hα region which is defined in the next section.
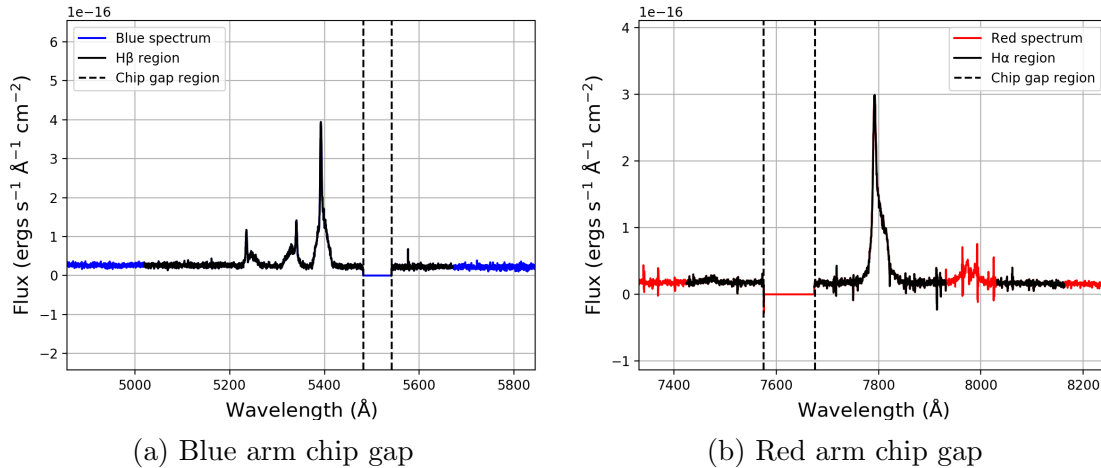
(a) Blue arm chip gap   (b) Red arm chip gap

Figure 12: Blue arm (a) and red arm (b) CCD chip gaps with spectra of redshift $z = 0.077$ and 0.187 respectively. The CCD chip gaps are contained between the black dashed lines. As described in the following section, these regions are not measured and will therefore be masked out before the continuum fitting.

5.2 Filtering OPR3 spectra - masking

The chip gaps contain no flux, therefore to avoid the chips gaps influencing the fit they were masked out. I also masked out any other areas of the spectrum where the instrumentation was unable to detect flux, for example at the far ends of the spectrum. This can be seen in Fig.13 at the end of the blue spectrum and the start of the red spectrum where there is a short wavelength range of 0 ergs s^{-1} Å^{-1} cm^{-2}.
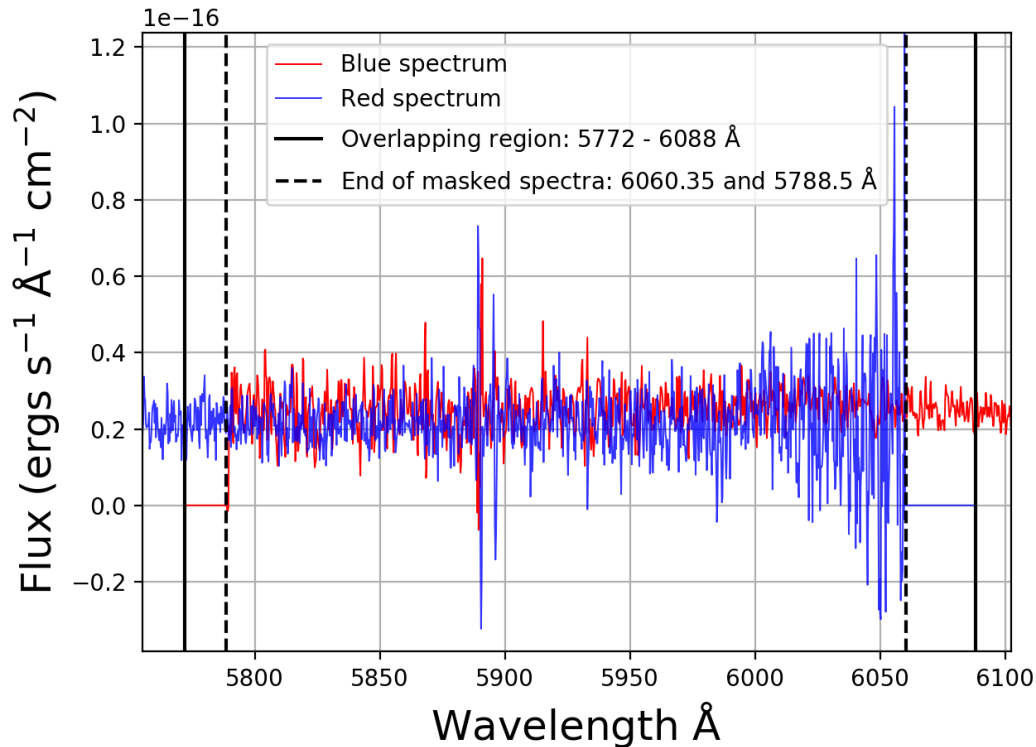
Figure 13: Overlapping region of the blue and red spectra. The black vertical lines represent the overlapping wavelength range for the two arms and the dashed black lines represent the overlapping region once the short wavelength range of 0 ergs s^{-1} Å^{-1} cm^{-2} either end of the spectra are masked out.

Before fitting for the continuum it is important to mask out all the spectral lines within the OPR3 spectra. I wrote an algorithm which masks out any flux within $\pm 35 \times (1 + z)$ Å of the line centres. Elements with lines modelled by the simulation which, with redshifts $z < z_m$, can fall within the WEAVE low-resolution wavelength range include: Calcium, Argon, Helium, Hydrogen, Balmer, Magnesium, Nitrogen, Neon, Oxygen and Sulphur lines. However, during the continuum fitting process (section 6.1) I found the dust attenuated templates were unable to adequately model the continuum. The χ_ν^2 is poor and the template does not sufficiently reduce the continuum to zero. In many cases, A_v tended towards 0 for all 13 templates, and allowing it to become negative improved the fit which clearly indicated that my model did not correspond to the spectra. The shape of the majority of the OPR3 spectra are either flat, where A_v is most likely 0, or blue, as demonstrated

in Fig.14a and Fig.14b respectively. A blue spectrum occurs when the flux decreases with
increasing wavelength, and a red spectrum for flux which increases with wavelength. Over
half of the BC03 templates have a red continuum, which means a negative A_v would be
required in order to fit these to the bluer OPR3 spectra. This indicates that there is a
problem with the flux calibration. The flux between the overlap of the blue and red arm in
Fig.14b appears discontinuous, which is further evidence of this calibration issue.

(a) Flat spectrum	(b) Blue spectrum
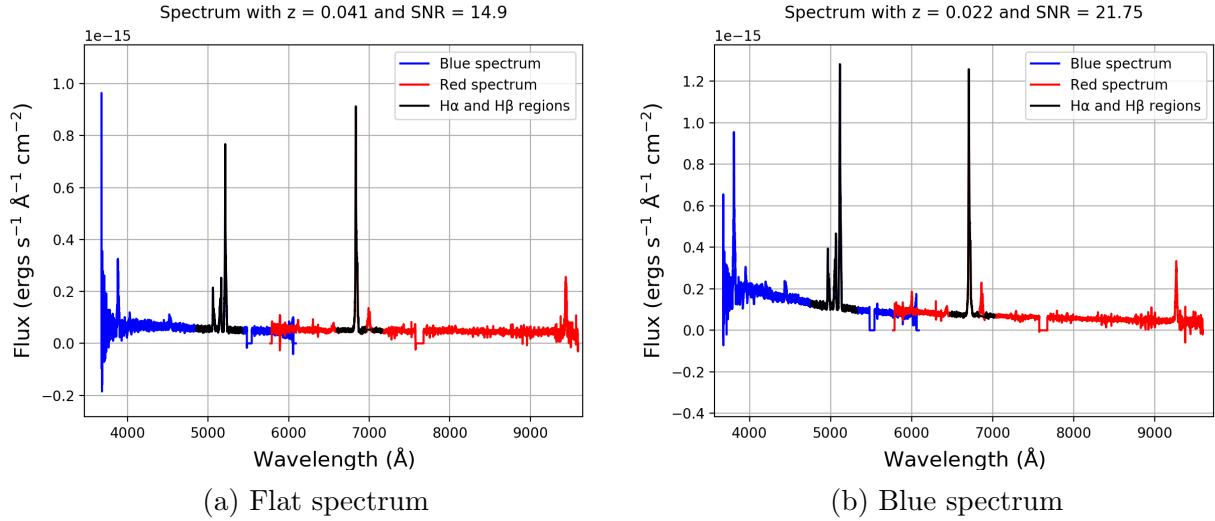
Figure 14: Two example spectra are presented to represent the two shapes of the majority
of the sample: a flat spectrum in Fig.14a and a blue spectrum in Fig.14b. The blue line
represents the wavelength range of the blue arm, and the red line represents the red arm.
The two black sections of the spectrum in each plot are the Hβ and Hα regions.

    I revised my approach of fitting the entire spectrum and instead masked the areas outside
of the Hβ and Hα regions. Each region is now not only defined by the emission lines but also
an additional $200 \times (1 + z)$ Å of continuum either side of the outer lines in the region: Hβ
to the broad OIII-2 line for the Hβ region, and the broad NII-1 line to the broad NII-2 line
for the Hα region. The only line that must be masked out for the continuum fitting, other
than the 12 which will be modelled, is the SII $\lambda/6731$ Å emission line which falls within
the Hα region, as demonstrated in Fig.15d. No other lines previously listed fall within the
wavelength range of these two regions. If an area within either of the regions is masked out
or cut off, whether it is due to the SII line, chip gap or the end of the blue or red spectrum,
the same area of continuum will be added on to either side of the region. In this way, the
quantity of data for the emitted wavelength range is the same for all the continuum fits.

(a) Hβ region with masked lines

(b) Hα region with masked lines

(c) Hβ region

(d) Hα region with masked SII line
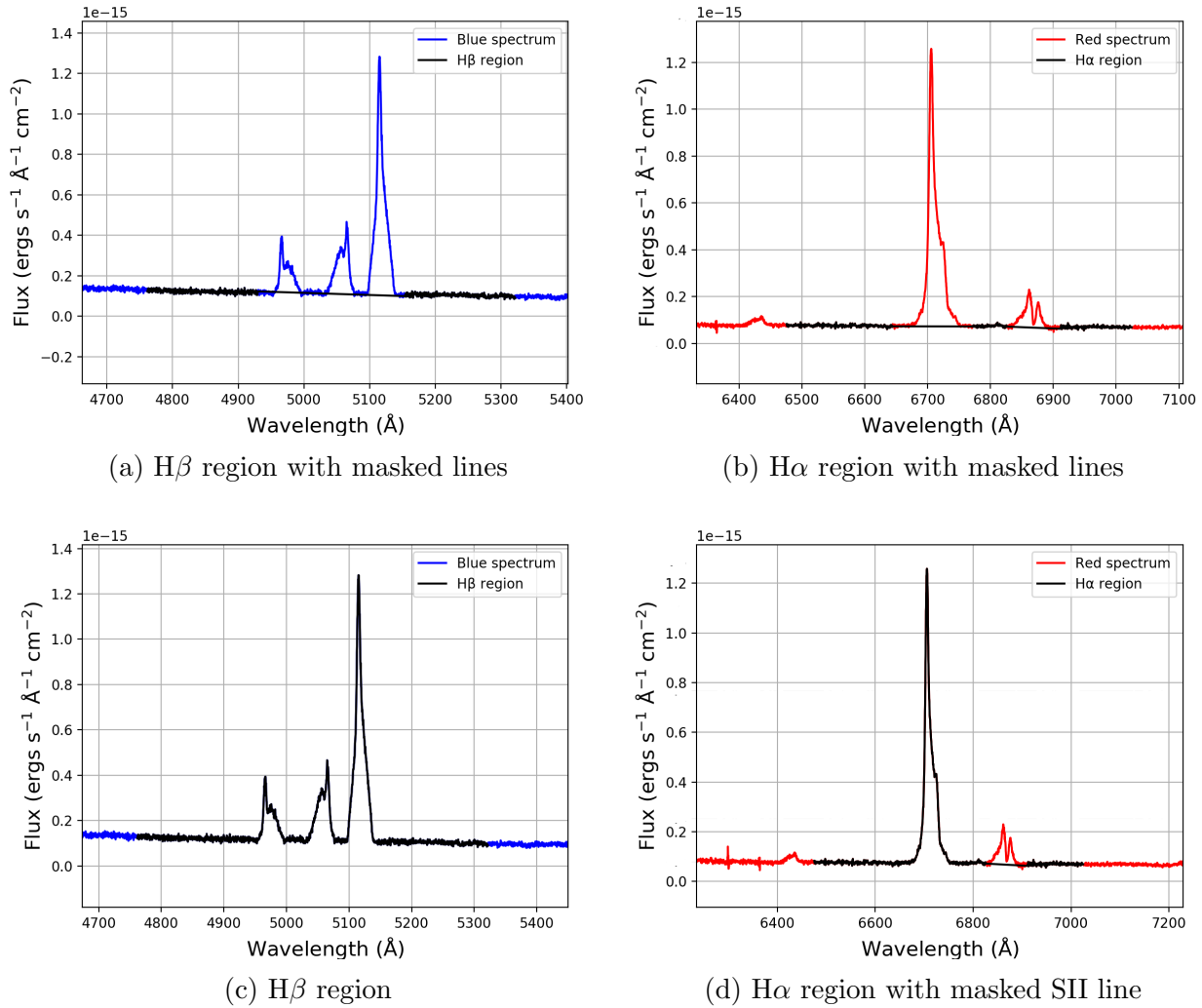
Figure 15: Each figure plots the observed spectrum of a radio source with $z = 0.022$. The black continuum sections in Fig.15a&b will be fit with the BC03 templates simultaneously. The black regions in Fig.15c&d represent the Hα and Hβ regions; defined as a $\pm 200 \times (1 + z)$ Å wavelength range from the outer redshifted emission lines in each region. Once the continuum is removed, the wavelength range of these regions will be used to fit the spectral lines. The redshifted SII emission line appears at 6879 Å in Fig.15b&d. The wavelength range of this line, $\lambda_e \pm 35 \times (1 + z)$, is masked out and the same range is appended to the end of the Hα region.

5.3 Overlap

There is a wavelength range between 5772 and 6088 Å where the blue and red spectra overlap. As the redshift increases from 0.18 to 0.3, the OIII doublet and Hβ will begin to cross this overlap as shown in Fig.16. Since the two spectra were captured with different instrumentation, it is important not to model a single emission line across this overlap. Conveniently, the wavelength range of this overlap is large enough to fit the flux of all three

emission lines. So when $z < 0.2$ the flux in the blue spectrum alone will be used to fit these lines, and when $z > 0.2$ the red spectrum will be used instead. At $z = 0.2$, OIII-2 is just about to fall within a $35 \times (1 + z)$ Å range of the end of the blue spectrum and Hβ is within the red arms wavelength range.

The Hβ and OIII doublet emission within the overlapping region at z = 0.2
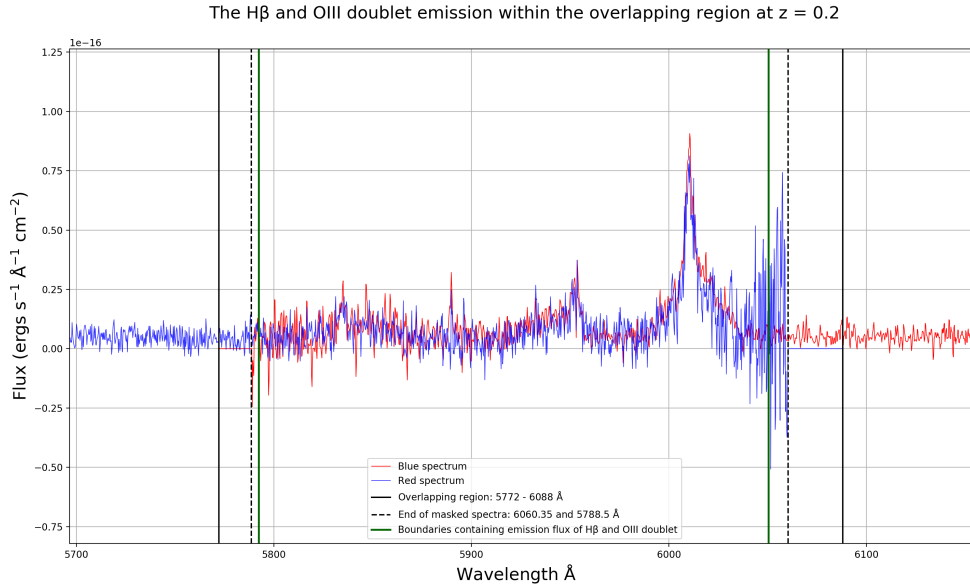
Figure 16: An OPR3 spectrum with $z = 0.2$ where the redshifted Hβ and OIII lines fall within the overlapping region. The overlapping region is represented by the black lines and is defined as the shortest wavelength of the red arms wavelength range, 5772 Å, and the longest of the blue arm, 6088 Å. The black dashed lines are the shortest, 5788.5 Å, and the longest wavelengths, 6060.25 Å, of the detected flux for this particular spectrum in the red and blue arm respectively. The wavelength range between the green lines contain the emission from all six lines, this is defined as $4861 - 35 \times (1 + z)$ Å for the shorter boundary and $5010 + 35 \times (1 + z)$ Å for the longest boundary. Both the green lines fall within the dashed black line region meaning it can be modelled by both the blue or red spectrum. The algorithm will model the lines in the blue spectrum for this example, and any targets with a redshift greater than 0.2 will be modelled by the red arm.

If the Hβ region falls within the wavelength range of the blue arm, the red spectra will be masked out between 5772 Å and the longest wavelength value in the blue spectrum which does not have a flux count corresponding to 0 ergs s^{-1} Å^{-1} cm^{-2} as this will have already been masked. The same applies for the blue spectrum when the Hβ region is modelled by the red arm. As the Hβ region approaches the overlap, any area of the $200 \times (1 + z)$ Å to the right of the emission lines which surpasses the end of the blue spectrum will instead be collected on the left side so that the quantity of data for the emitted wavelength range is the same for all the continuum fits. This consistency is important in order to compare the results of the continuum and emission properties. It also means the spectra experience the same level of degeneracy in the fits.

In future work we can take advantage of this overlap and use it to investigate the inconsistent flux calibration between the blue and the red spectra. Once this has been fixed the

algorithm can be instructed to model the emission lines in both spectra at this overlap as a combination of the two samples will give a better estimate of the flux.

5.4 Flux calibration in the two arms

When WEAVE is in operation its CCDs will detect photons, convert them into an electron charge and read them out with some gain in units of counts. The amount of energy detected by each pixel gives rise to the number of counts measured, and these can be converted into flux. This required the WEAVE observations to be flux calibrated which is done by positioning, on average, 15 of the 950 fibres on white dwarf sources for which the brightness is known by a prior method. It is then possible to compare the number of counts that the MOS reads out at a particular wavelength to the known spectrum of a standard white dwarf, and averaging that factor over the calibration targets in the observing block gives the sensitivity function, which is used to multiply the counts to obtain a flux calibrated spectrum. The origin of the offset between the red and blue spectrum, shown in Fig.17), is suspected to be caused by an issue with this flux calibration. The reason is not fully understood at this stage, but it is important to recognise that I must model each spectrum with separate scaling factors. This is discussed further in section 6.1 after I have fit the continuum, retrieved the normalisation parameters posterior distributions and determined the offset ratio between the two arms.
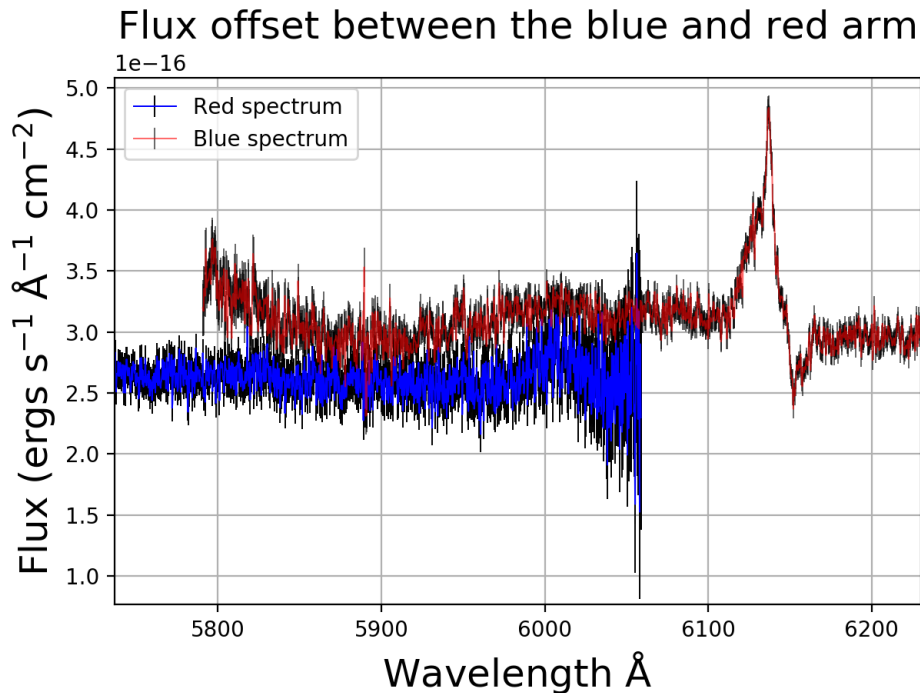
Figure 17: A spectrum with a large offset between the blue and red spectra with $z = 0.045$ and SNR $= 34.68$. The error bars, taken from the RMS array of the spectrum, show that the difference is significant.

As previously explained in section 4.2.2, a ratio between the two correction factors can be found during the continuum fitting process and this can be used to align the two spectra. However a choice needs to be made: whether to apply the ratio to the red or to the blue spectrum. If they are both incorrectly calibrated, then aligning one with the other will not result in a correctly calibrated spectrum. I will continue under the assumption that the blue spectrum is incorrectly calibrated, and aligning it with the red should produce a spectrum which is representative of what the true observed flux should be. This can be tested later when comparing the MCMC estimated line fluxes to the input fluxes. I selected the blue end of the spectrum as it is most sensitive to high temperatures and this could be a potential reason for a calibration issue when using white dwarfs. The majority of the spectra in the OPR3 sample do not appear to be offset with each other, therefore I expect the average ratio of the normalisation parameters to be close to 1.

5.5   Setting the priors and initial guesses

The following priors for the Gaussian parameters were originally set for both the narrow and broad lines. Section 7.1 expands on the decision to change the way I model the non-Gaussian broad components and how the parameters, priors and initial guesses change accordingly.

Normalisation parameter:

- Prior: $0 < a$ (ergs s^{-1}Å^{-1}cm^{-2}) $< 1e{-}12$

- Initial guess: Flux detected at the line's observed wavelength

- Parameter quantity: 12

The minimum boundary is set to 0 ergs s^{-1} Å^{-1} cm^{-2} as I am modelling emission lines, not absorption lines, and a sensible maximum of 10^{-12} ergs s^{-1} Å^{-1} cm^{-2} is set to confine the MCMC walkers within the correct region. The initial guesses for the heights of the Gaussians are selected by taking the flux which corresponds to the line centres wavelength within the continuum subtracted spectrum. This will most likely be larger than the true height since the superposition of emission lines will shift the peak of the Gaussian. To account for this I reduced the heights by 20% for the initial guess, and in cases such as the broad and narrow OIII-2 and Hα lines, where there is more extreme blending, I took a further 50% off. These percentages were decided using visual inspection, other values were tested which did not impact the outcome but did result in a longer burn-in for the MCMC chains. The process that I selected ensures that there are more samples in the posterior distributions, and consequently more reliable estimates for the parameters.

Velocity dispersion:

- Prior: $0 < \sigma_{\mathrm{v}}$ (km s^{-1}) < 1000

- Initial guess: $\sigma_{\mathrm{v},\,0}^{\mathrm{narrow}} = 120$ km s^{-1}, $\sigma_{\mathrm{v},\,0}^{\mathrm{broad}} = 450$ km s^{-1}

- Parameter quantity: 2

Visual inspection suggests that the velocity dispersion of the source for the emission lines is expected to be no more than 500 km s^{-1}. I will be modelling all the lines in the Hα and Hβ region together, therefore it is not crucial to constrain the boundaries on the priors. Hence I have set them to a comfortable range of 1000 km s^{-1}. The decision to set the initial guess of the narrow lines at 120 km s^{-1} and the broad lines at 450 km s^{-1} comes from visual inspection. This choice does not affect the results as the MCMC algorithm is robust against large perturbations of the initial guesses. Any value for the emission lines between 50 and 300 km s^{-1} would be a suitable initial guess as the width varies a lot between sources and this choice does not strongly influence the results.

Velocity offset:

- Prior: $-200 < v \ (\text{km s}^{-1}) < 200$

- Initial guess: $v_0 = 5 \ $ km s^{-1}

- Parameter quantity: 1

The velocity offset measures the relative motion between source of the emission lines and the continuum. As I have shown in Fig.5, it is suspected that the narrow line centres were used to determine the redshift factors, therefore I expect MCMC with return estimates of 0 km s^{-1} for σ. Consequently, I have set a low boundary of 200 km s^{-1}, and an initial guess of 5 km s^{-1}. This boundary needs to be tightly constrained considering the close proximity of the narrow and broad lines. Each of the broad lines have different velocity offsets relative to their narrow components, so instead of setting a fixed rest-frame wavelength with a free v parameter for each broad line species, the rest-frame wavelength will instead be modelled as a free parameter. Since their rest-frame wavelengths appear to be consistent for all the OPR3 spectra, the estimated rest-frame wavelengths in section 4.2.3 will be used as their initial guess. This should avoid the broad lines mistakenly modelling their narrow components.

Broad line centres:

- Prior: $-9000 < \lambda_{e,b}(\text{Å}) < 9000$

- Initial guess: Listed in section 4.2.3

- Parameter quantity: 6

There are essentially no boundaries on the broad line centres, restricting these within a tight region only results in a poor fit of the broad components. The algorithm is capable of finding the optimal value for this parameter even with a very large prior. The initial guess of the broad components are set to the values listed in section 4.2.3: Hβ = 4870 Å, OIII-1 = 4950 Å, OIII-2 = 5010 Å, NII-1 = 6543 Å, Hα = 6571 Å and NII-2 = 6593 Å. As mentioned, the broad lines are nuisance structures and the only purpose of fitting them is to remove them from their blended, narrow counterparts.

Initial position arrays for each of the parameters are generated containing 100 values which are sampled from a normal distribution around the initial guess. There are an equivalent number of walkers which are assigned one of these values to begin a 'walk' along their chain. The standard deviation, σ, of each normal distribution is selected based on how certain I am about the initial position and how much it is expected to vary between different

galaxies. For instance, the velocity dispersion is expected to differ significantly between sources, therefore a σ of 10 km s^{-1} is set. The standard deviation does not significantly impact the results, however it does influence how quickly the walkers converge around an estimate, this is referred to as the burn-in which should be minimised to obtain more samples for the posterior distribution. The profile peaks has a σ set to the corresponding standard error in RMS array, the velocity offset is set to 0.5 km s^{-1} and the broad line centroids to 0.05 Å.

The model assumes that the errors in the RMS array have been underestimated by an unknown fractional error, f, which is to be considered along with the known standard errors. This additional parameter will be used in the MCMC fitting algorithm for both the continuum and the emission line modelling. This is a nuisance parameter and will not be used in any further calculations once it is recovered. It is not sensible to set a uniform prior on f as it is unknown and and could hold any value between 0 and 1. A prior should be used that is insensitive to scale, therefore I will be using the logarithm of f. This means smaller fractio will be sampled with the same probability as larger values; essentially meaning that it has a uniform probability distribution in log space. Table 1 displays the priors, initial guesses and σ for each of the continuum parameters.

	log f	A_v	N_b	N_r
Min:	-6	0	0	0
Max:	1	10	3	3
Initial:	log(0.3)	0.5	*	*
σ:	0.5	0.3	0.3	0.3

Table 1: List of the maximum and minimum priors, the initial guesses and σ for the four continuum parameters. Where there is an *, the median of the continuum flux divided by the template flux in that spectrum will be used.

5.6 Statistics

Within the OPR3 files there are 16,874 targets with 2 fits files for the blue and red regions of the spectra. Of these radio-selected targets, 7273 are star-forming galaxies and the rest are AGN with redshifts that range from 0.012 to 6.96. After filtering out the AGN and those with redshifts within the specified ranges ($z > 0.448$ and $0.077 < z < 0.187$) there are 1471 remaining targets with all the BPT-NII lines available for fitting. All the relevant information required for the fitting of each target's spectrum is listed below:

- Tag : This refers to the name of the file

- Flux : The combined arrays of flux values for the blue and red arm

- Wavelength : The combined arrays of wavelength values for the blue and red arm (every 0.25 Å)

- RMS array : The combined arrays of the flux standard errors for the blue and red arm

- z : Redshift of the associated target

- Hβ side: Whether the Hβ emission lines fall within the wavelength range of the blue or red arm

- SNR: The SNR of the masked spectrum, the Hβ region and the Hα regions (taken within ± 35 Å of the outermost emission lines)

5.7 Testing the algorithm

There are input line luminosities and SFRs available for the OPR3 spectra to which I will compare with my results. This will provide some idea of how well the MCMC fitting algorithm can return the input values after experiencing absorption from the atmosphere, seeing effects, instrumental noise and other processes which result in a loss of photons. I will also test how accurately my algorithm can retrieve the model parameters by running it on spectra I have built using my own input parameters. These will consist of Gaussian line profiles, Gaussian noise, dust attenuation and a BC03 continuum template compiled together. This will enable me to isolate and fix issues and also ensure confidence in the algorithm. It is important to note that these basic model spectra will in no way compare to the sophistication of the OPR3 simulation, and their only purpose will be to validate my algorithm. In this way, I can trust the BPT and SFR results have been accurately determined, with well estimated uncertainties.

To quantify the goodness of the fit I will calculate the reduced chi-squared, χ_ν^2, which is represented in Eq.18. It is otherwise known as the chi-squared per degree of freedom. The chi-squared, χ^2, is a weighted sum of the squared difference in the observed and expected data over the square of the standard error; this is represented in Eq.17 where σ_i^2 is the variance, O is the observed data and E is the expected data. The number of degrees of freedom is the number of observations minus the number of fitted parameters ($v = n - m$).

$$\chi^2 = \sum_i \frac{(O_i - E_i)^2}{\sigma_i^2} \tag{17}$$

$$\chi_\nu^2 = \frac{\chi^2}{v} \tag{18}$$

In general, when the $\chi_\nu^2 \gg 1$, this indicates the estimated parameters poorly model the observed data and if $\chi_\nu^2 > 1$, then the model has not fully captured the data and it is overfitting it. When the $\chi_\nu^2 = 1$ then the match between the expected data and the observed data is in accordance with the variance. This statistic alone is not ideal to use for spectral fitting as it does not provide enough information about the quality of the fit. A χ_ν^2 close to 1 informs us that the model has fit the data, however it does not tell us if the emission is contaminated by, for instance, skylines or continuum features which the model failed to subtract from the spectrum. Nevertheless, it still has value and will be used alongside other statistics such as the SNR and parameter uncertainties.

6 Method

6.1 Continuum fitting of the entire spectrum

As mentioned, I began the modelling of the continuum by masking the spectral lines and attempting to fit the entire WEAVE wavelength range of the continuum with a BC03 template and the Calzetti attenuation curve. The MCMC fitting algorithm takes into account the RMS array for each spectrum and outputs a posterior probability distribution for each of the parameters; the mean values of these distributions are used for the continuum fit. The algorithm produces 13 sampler results for the different templates; the optimum set of parameters is determined by whichever fit results in a χ_ν^2 closest to 1.

I initially tested the fitting algorithm on a high SNR spectrum with a redshift of 0.012. The ssp: 100 Myr template proved to be the optimal fit, with the lowest χ_ν^2 of 19.3 which is unexpectedly high considering the BC03 templates were used by the OPR3 simulation to build the spectra. The optimal fit using the ssp: 100 Myr template is plotted against the spectrum with masked and unmasked spectral lines in Fig.18a and 18b respectively. It is clear that the algorithm was unable to find parameters that adequately modelled the spectrum of the blue arm since the best-fit in this wavelength range does not align with the spectrum. There are two possible reasons to explain why the full spectral fitting method was unsuccessful: either the model does not represent the spectrum or there is an unidentified error in the algorithm. If it is the latter then there exists a set of parameters for the current model which sufficiently fits one of the BC03 templates to the data. After investigating this issue, I concluded that the model did not correspond to the data due to an inconsistency in the flux calibration which has distorted the shape of the spectrum and significantly impacts the bluer end. Fig.18c plots the best-fits for all 13 of the templates against the spectrum. The shapes of all but three of the templates at the blue end are sloped in the same direction as the spectrum, however the remaining templates are redder and require a negative A_v. This is unphysical, therefore to prevent the issue occurring a prior has been set on A_v such that it cannot become negative. The projected posterior distributions of A_v push up against this prior for all the fits using the BC03 templates in Fig.18c, including ssp: 100 Myr, whereas the samples for the other three parameters successfully formed Gaussian distributions.

Fig.19 presents the continuum subtracted spectrum using the unmasked data in Fig.18b. The continuum is unsuccessfully subtracted at the bluer end of the spectrum which is noticeable in Fig.19c and evident around the Hβ region in Fig.19a as the continuum subtracted flux does not align with zero along the x-axis. Fig.19b shows a successfully subtracted area at the redder end of the spectrum around the Hα region, where only emission lines and skyline absorption features remain.
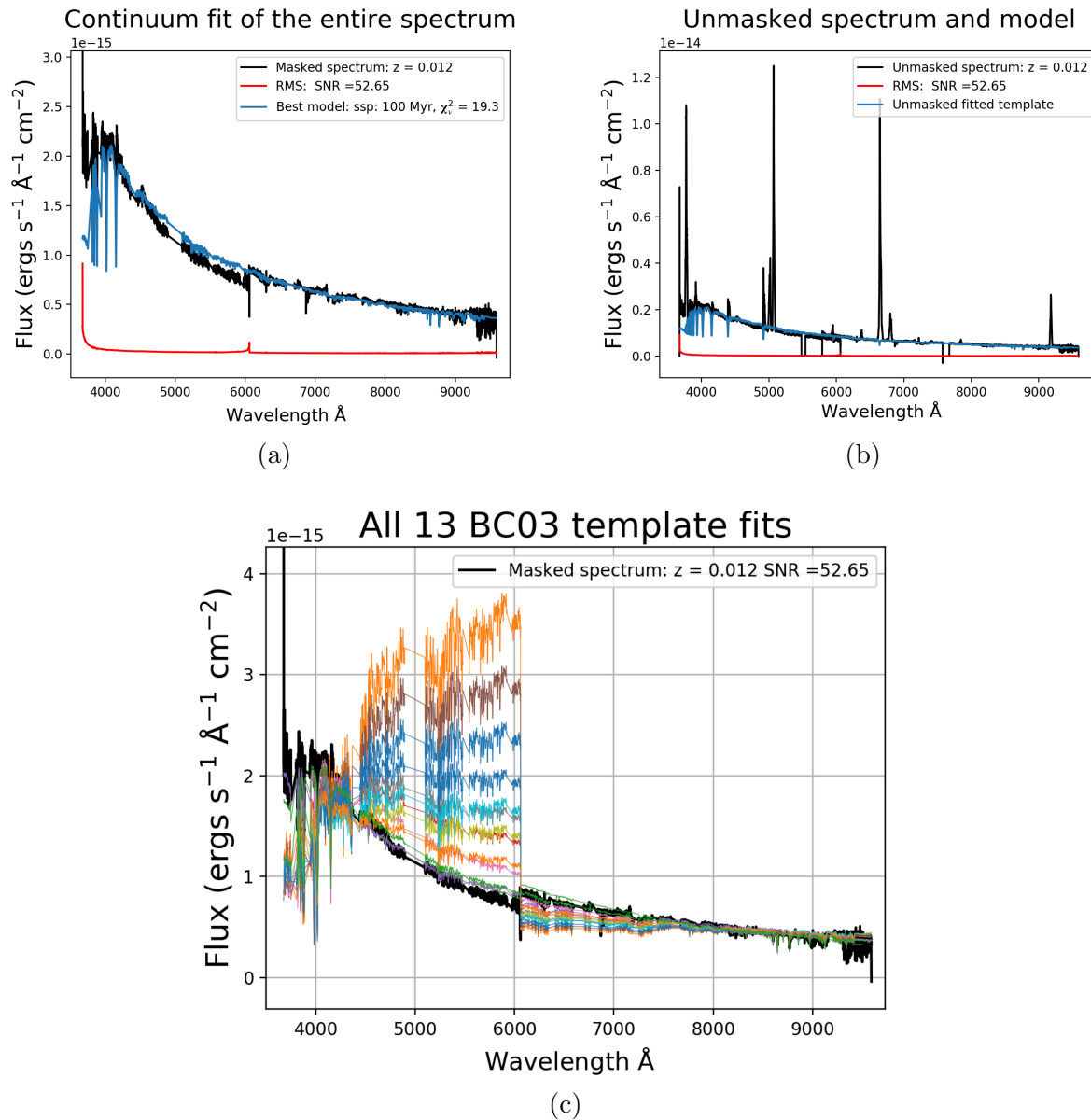
Figure 18: A spectrum (black) is plotted in each of the figures along with continuum fits using an MCMC fitting algorithm. The spectral lines in Fig.18a are masked, therefore the spectrum only consists of the continuum. The best-fit template of the masked data, with a χ^2_ν of 19.3, is plotted in blue and with the RMS array in red. Fig.18b plots the unmasked version of the data. And Fig.18c plots the best-fit models for all 13 of the BC03 templates.

(a) Hβ region

(b) Hα region
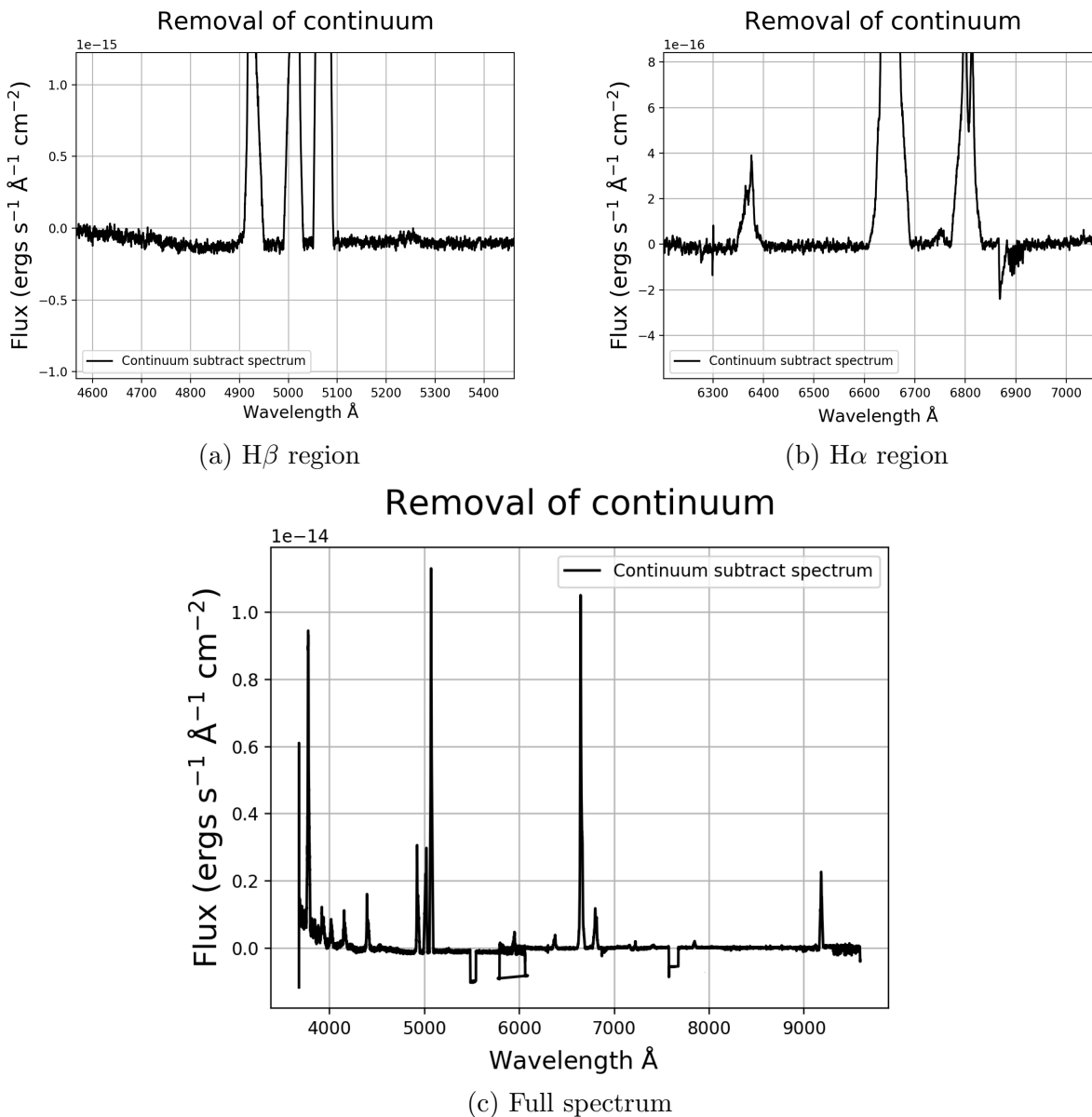
(c) Full spectrum

Figure 19: The continuum subtracted spectrum using the fitted model from Fig.18b is presented. Fig.19c shows the full continuum subtracted spectrum, Fig.19a shows the continuum subtracted section around the Hβ region and Fig.19b around the Hα region. It is most successfully subtracted at the redder end of the spectrum, however much of the continuum remains in the blue and there are several areas where it has been over subtracted.

Despite the evidence that suggests the model does not represent the data, it is important to check that the algorithm is otherwise functioning as expected. Before I obtained the parameter estimates used in the above fits, I reduced the data in the MCMC chains by determining the burn-in. This is done by plotting the chains which shows the position of each walker as a function of the number of steps in the chain. The chains of the four parameters used to determine the continuum model in Fig.18a are presented in Fig.20. There are 100 walkers so each of the parameters contains 100 chains which begin to sample values at the

given initial positions. After a period of time, the sampling converges in the region of highest probability. At this point the chain has essentially 'forgotten' where it started and this is defined as the burn-in. Visually speaking, it is where all of the chains converge around a smaller region of values in Fig.20, hence we choose to discard the first 200 steps for burn-in. The algorithm for the WEAVE spectra must be automatic with minimal interference, therefore it is wise to set a high burn-in and a high number of steps if you are not limited by CPU time or resources. As such, I specified a chain length of 5000 steps and a burn-in of 1000 for the full spectral fitting of the continuum.
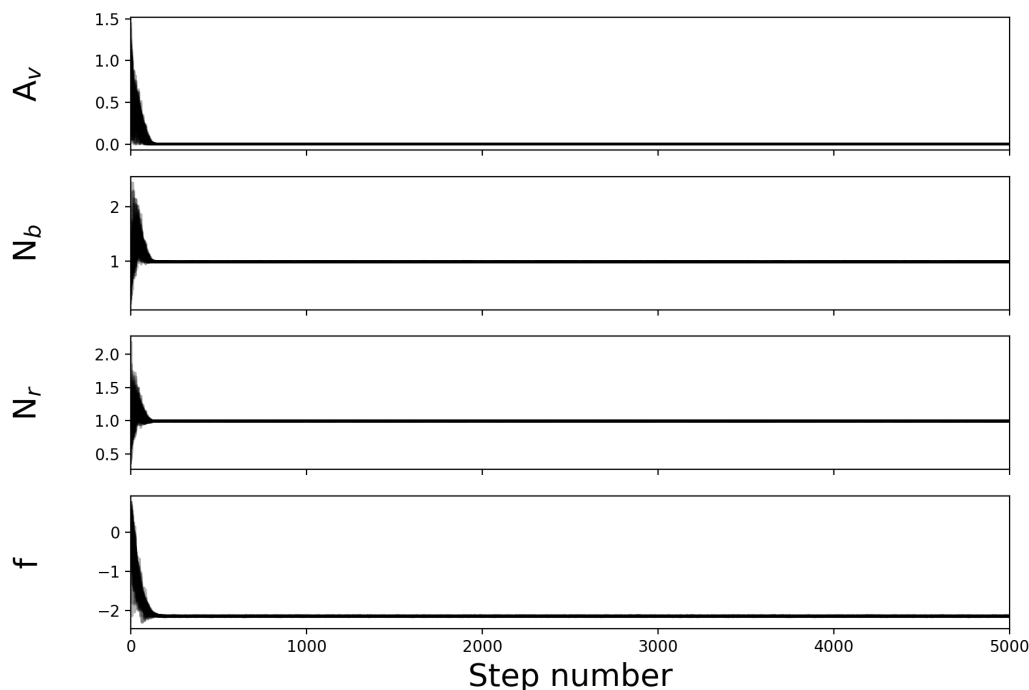
Figure 20: The positions of each walker as a function of the number of steps in the chain. The walkers start at their assigned initial position, as listed in section 5.5, and begin to explore the full posterior distribution. All the walkers quickly start to converge around an estimate for each parameter, at this point the samples are described as well burnt-in. The burn-in is complete around 200 steps for each parameter.

The chains give no reason to be concerned about the algorithm as all the walkers for each of the parameters have tightly converged around the same region after a short burn-in of 200 steps. This suggests the algorithm has successful located the best-fit sample of parameters to model the continuum. Fig.21 displays the corner plot of the one and two dimensional projections of the posterior probability distributions for each parameter. This is useful because it demonstrates all of the co-variances between parameters. Each given parameter estimate are represented by the blue lines in Fig.21, these are the mean values of these posterior distributions, and their uncertainties are equivalent to one standard deviation. These

one-dimensional errors do not assume Gaussianity as it takes half the difference between the 16th and 84th percentile of the parameters posterior distributions.
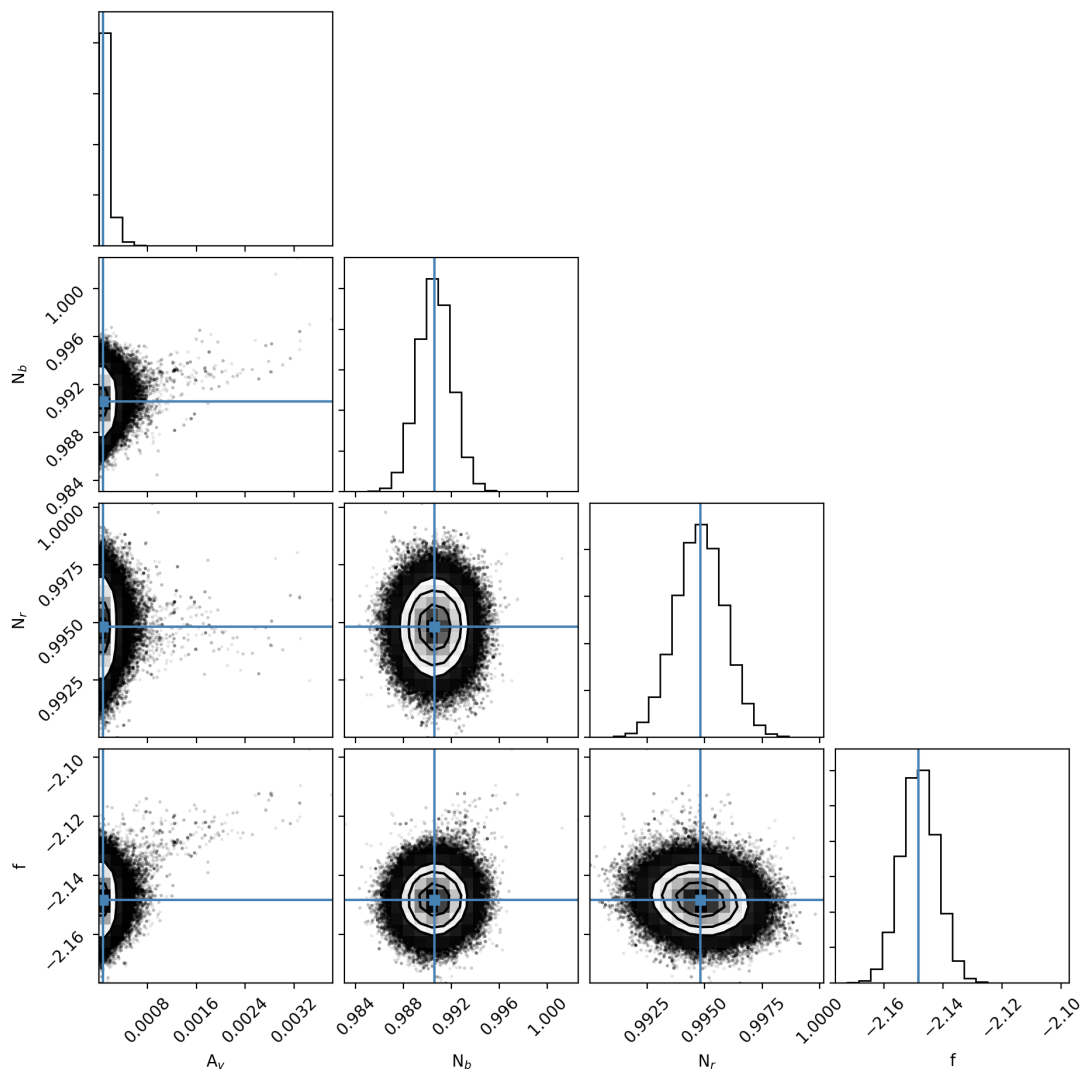
Figure 21: The one and two dimensional projections of the posterior probability distributions for each parameter. This corner plot shows the marginalised distribution for each parameter independently in the histograms along the diagonal and the marginalised two dimensional distributions in the other panels (Foreman-Mackey et al., 2013). The blue lines are the mean posterior estimates of each parameter which were used for the models in Fig.18.

It is clear from the posterior probability distribution of A_v in Fig.21 that the optimum fit of the spectrum using ssp: 100 Myr most likely requires a negative A_v as the walkers push up against the prior. The histograms of the marginalised distributions of the other parameters form a Gaussian profile around the mean of the sample which suggests that the algorithm is functioning as intended and the templates coupled with the Calzetti attenuation curve are simply poor models for the continuum which has been distorted. This indicates that there is

an issue with the flux calibration methodology, which is causing the shape of the blue arm to require negative A_v. This will also affect the real WEAVE data, hence it must be corrected.

To circumvent this global calibration issue, I will focus on fitting the continuum in the intermediate wavelength ranges around the emission lines of interest in the Hα and Hβ regions, so that I can still proceed with the extraction of emission line fluxes. Since the shape is less restrictive, it should result in much lower χ^2_ν values and the continuum surrounding the emission lines can be adequately removed so only the emission lines remain. The drawback, however, is that the probability distribution will be larger for a wider range of parameter values. The main three parameters influence the shape of the model and hence masking the majority of the spectrum will increase their degeneracy. The MCMC algorithm will sample values along the correlation between each of the parameters. It will not be able to distinguish between the parameters since the shape of the template will be harder to pick out, especially at low SNR. This is a fundamental limitation of the approach which will be accepted since the primary goal of modelling the continuum is to remove it and not to determine precise extinction parameters. Before using the revised model on the OPR3 spectra I tested it on simplified model spectra, built using the BC03 templates and the Calzetti attenuation curve. This enables me to monitor the limitations of the algorithm and ensures it is capable of outputting sensible posterior distributions for the parameters.

6.2   Building simplified model spectra

The model spectra were built by selecting a BC03 template, superimposing emission lines using the Gaussian function, applying the Calzetti dust attenuation curve (Fig.22a), modelling the fractional amount the standard errors are underestimating the noise (Fig.22b), adding Gaussian noise (Fig.22c) and applying an offset between the blue and red spectra (Fig.22d). Each of these steps are visualised in the five plots in Fig.22. The continuum parameters for this model are set to: $A_v = 0.693$, $N_r = 0.6435$ ($S_{cr} = 1$, $S_t = 0.6435$), $N_b = 0.4719$ ($S_{cb} = 0.7334$) and f = 0.1.

The 'ssp: 25 Myr' template has been selected as it has one of the bluest continua, therefore is of the subset of relatively unobscured star-forming galaxies which are the focus of this project. S_{cr} has been set to 1 as I am assuming the flux in the red spectrum has been correctly calibrated. The known emission wavelengths for the narrow lines and the estimated centres for the broad lines were used as the mean in the Gaussian function. Heights were chosen to be in the range of fluxes consistent with those from the corresponding lines in the OPR3 model spectra. The widths were derived using a given velocity dispersion of 150 km s^{-1} and 400 km s^{-1} for the narrow and broad lines respectively and velocity offsets were set to 0 km s^{-1} in accordance with the OPR3 model spectra. A redshift of $z = 0.1$ was applied to the synthetic spectrum to ensure that the model redshifting algorithm is implemented correctly. This redshift places the Hβ region comfortably within the blue spectrum.

The multiplicative factor, f, accounts for the underestimates of the uncertainties in the model data. This is applied by adding a random Gaussian distribution to the flux, where $\sigma = (\text{f} \times \text{flux})$ and $\mu = 0$. A synthetic array of standard errors were generated using a uniform distribution with $\mu = 4.2 \times 10^{-17}$ and $\sigma = 10^{-18}$. These numbers were selected to produce a standard error array which results in a SNR close to the average SNR of the OPR3 sample (6.85) with little variance to replicate the relatively smooth RMS curve of the

OPR3 spectra. The noise is applied to the spectrum by drawing samples from a random normal distribution with $\mu = 0$ and $\sigma =$ standard errors and adding it to the flux. As previously explained, the purpose of these simple simulations is to further ensure that the model is functioning as expected. In this way, I can trust the BPT and SFR results have been accurately determined, with well estimated uncertainties.
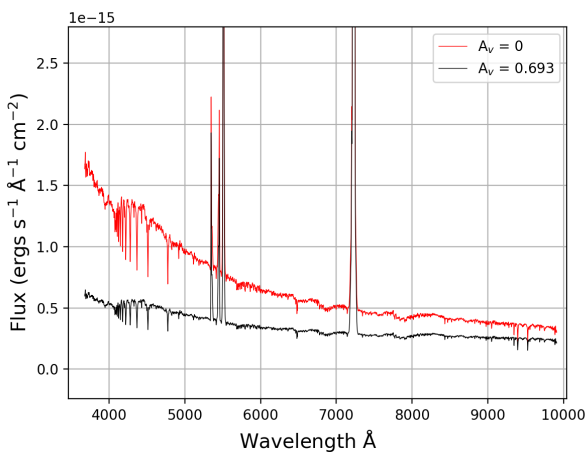
(a) Continuum is reddened with $A_v = 0.693$
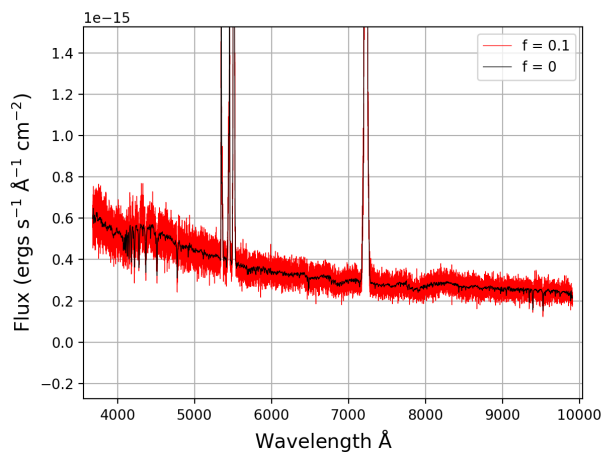
(b) Multiplicative factor (f = 0.1) applied
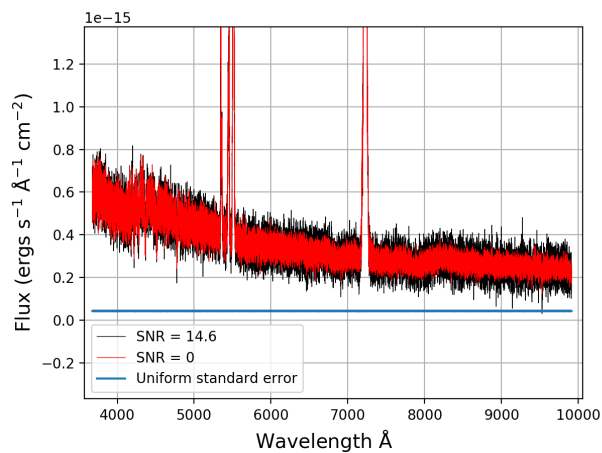
(c) Uniform standard error array applied to flux with a normal distribution
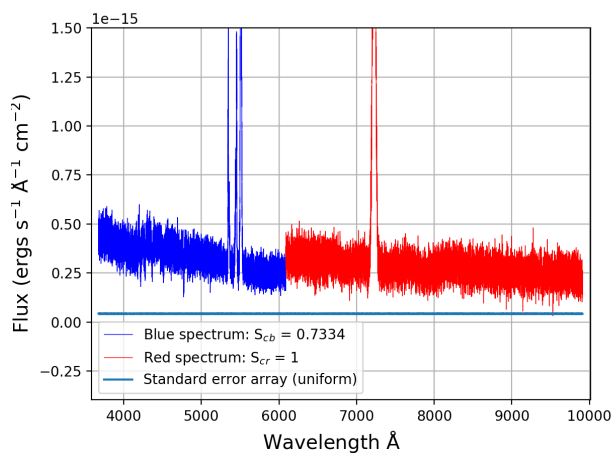
(d) Offset of $S_{cb} = 0.7334$ applied
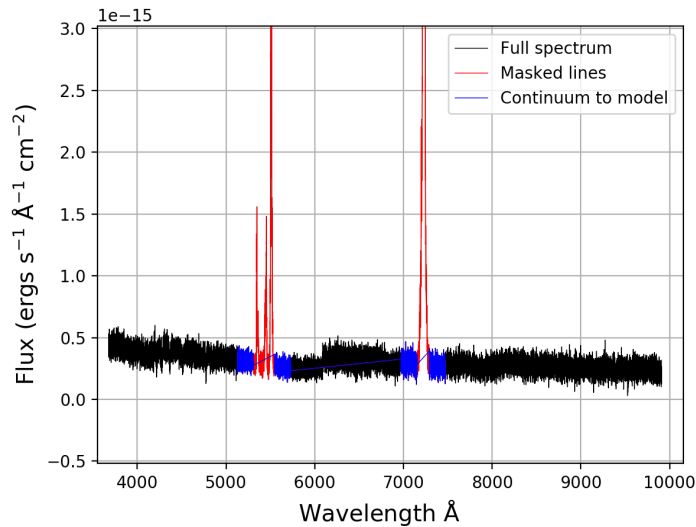
(e) Three main sections of the spectrum

Figure 22: Visualisation of the process undertaken to build the synthetic spectra. The red spectrum in Fig.22a shows the redshifted ssp: 25 Myr template with superimposed Gaussian emission lines. The black spectrum in this figure is the result of applying the Calzetti starburst attenuation curve with an A_v of 0.693. The same black spectrum is plotted in Fig.22b and the red spectrum is the outcome of applying f = 0.1 to it (i.e. the fractional amount that the standard errors are underestimating the noise in the spectrum). This is again plotted in Fig.22c alongside the noisy version of spectrum in black and the standard error array in red. Fig.22d demonstrates the offset between the blue and red spectrum (N_b/N_r = 0.7334). Fig.22e indicates the three main sections of the spectrum which are relevant to the fit: the black represents the masked continuum, the blue section will be used to fit the continuum and the data in the blue and the red sections will be used to fit the emission lines once the continuum has been subtracted.

6.3   Continuum fit of simplified model spectra

The initial values and priors for the continuum fitting of the simplified model spectra are set to those listed in section 5.5 for the OPR3 spectra. I have decreased the number of steps from 5000 to 3500 as this will be more than sufficient for the fitting of a much smaller section of the continuum and it will reduce the CPU time and dependence on resources. The χ^2_ν of all 13 template fits for this synthetic spectra fell between 1 and 1.4, which is a vast improvement from the full spectral fitting of an OPR3 spectrum with a best-fit χ^2_ν of 19.3. The BC03 template selected as the best-fit for the spectrum is also the same one used to build it, which is very encouraging. It is not essential to select the correct template if it is still able to adequately remove the continuum in the wavelength range around the emission lines, but it is a good indicator that the algorithm is working as intended. The four templates with χ^2_ν closest to 1 are presented in Fig.23. Despite the fact that the other three poorer fits used a template which was not actually used to build the spectra, they still manage to sufficiently model the continuum in order to remove it from the emission lines.
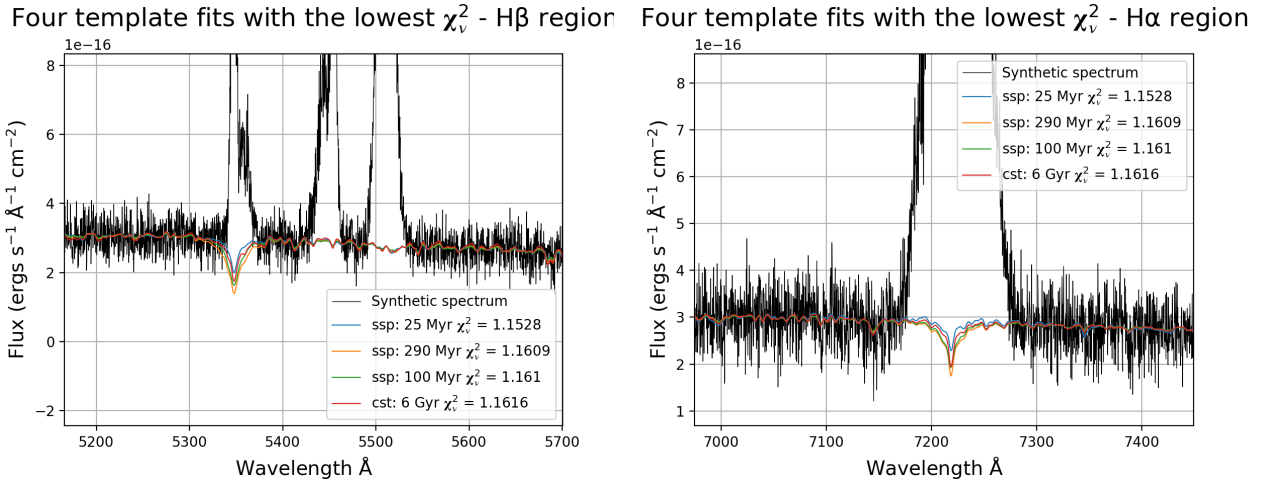
Figure 23: Four continuum fits of the Hβ and the Hα regions that resulted in the lowest χ_ν^2. The templates plotted are the ssp: 25 Myr with a $\chi_\nu^2 = 1.1528$ (blue), ssp: 290 Myr with a $\chi_\nu^2 = 1.1609$ (orange), ssp: 100 Myr with a $\chi_\nu^2 = 1.161$ (green) and cst: 6 Gyr with a $\chi_\nu^2 = 1.1616$ (red). Unsurprisingly, each of these templates have very similar shapes as illustrated in Fig.6.

Fig.24 presents the continuum subtracted spectra derived from subtracting the best-fit model from the synthetic spectrum. The flux that remains is now dominated by noise or emission line features. This indicates that the algorithm has so far performed as intended. The subtracted spectrum of the Hβ and Hα regions will be used to fit the Gaussian model to the emission lines once they have been corrected for the offset caused by the flux calibration issue.
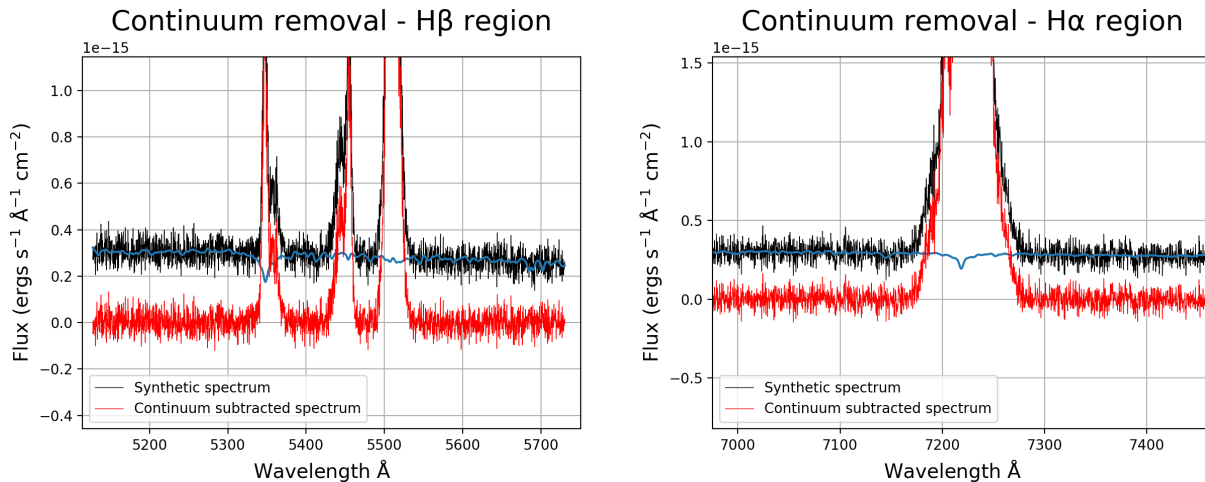
Figure 24: The continuum subtracted spectrum is represented by the red line which is derived from subtracting the model (blue line) from the synthetic spectrum (black line). The Hβ and Hα regions are presented in either plot; the Gaussian model will be fit to these two areas of the spectrum to retrieve emission line parameter estimates.

The chains in Fig.25 for each of the 100 walkers in the sample converge from their initial starting positions by 750 steps, therefore the burn-in is now set to 1000 steps. The corner plots for all four parameters are presented in Fig.26, where the blue lines indicate the true values used to build the continuum. The one dimensional marginalised distributions of A_v, N_b and N_r form approximately Gaussian histograms with means close to the true values. This means that the algorithm has managed to recover values consistent with the input values once the uncertainties are taken into account. The two dimensional plots between these three parameters all show very tight positive correlations, which is as expected as they all influence the shape of the continuum. The estimation of the parameter log f is acceptable as it is a nuisance parameter so we inherently don't care what value it takes and it will not be used in any further calculations. This parameter does not correlate with any of the other parameters and its projected posterior distribution is non-Gaussian. I would only expect a Gaussian distribution where the model is linear in the parameter.
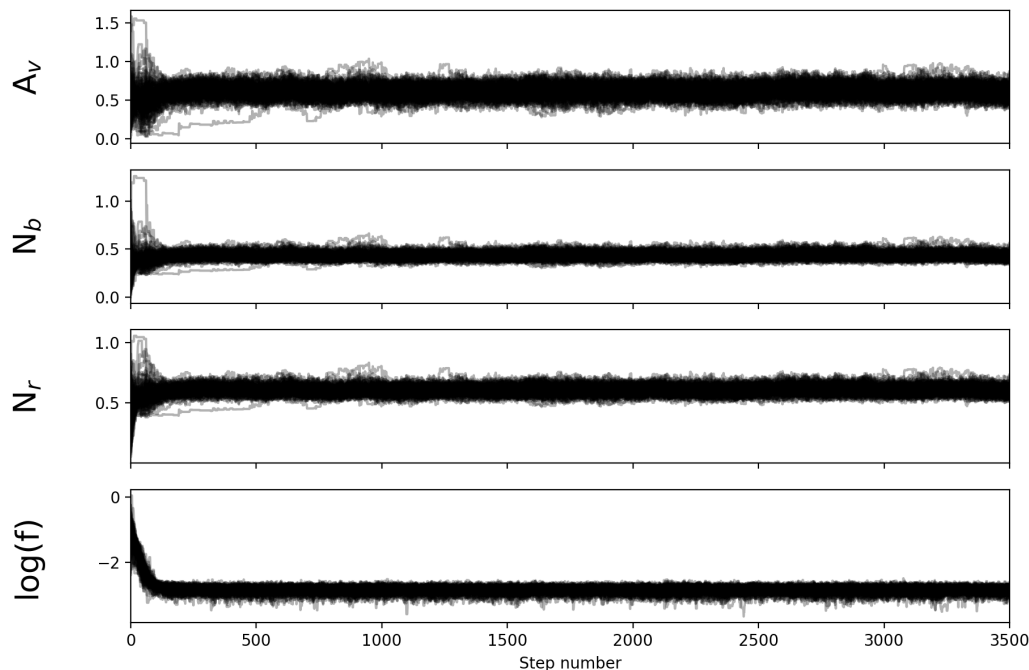
Figure 25: The positions of each walker as a function of the number of steps in the chain for the continuum model using the ssp: 25 Myr template in Fig.23. The walkers start at their assigned initial position, as listed in section 5.5, and begin to explore the full posterior distribution. The walkers are well burnt-in around 750 steps, therefore the first 1000 steps are removed from the sample.

.
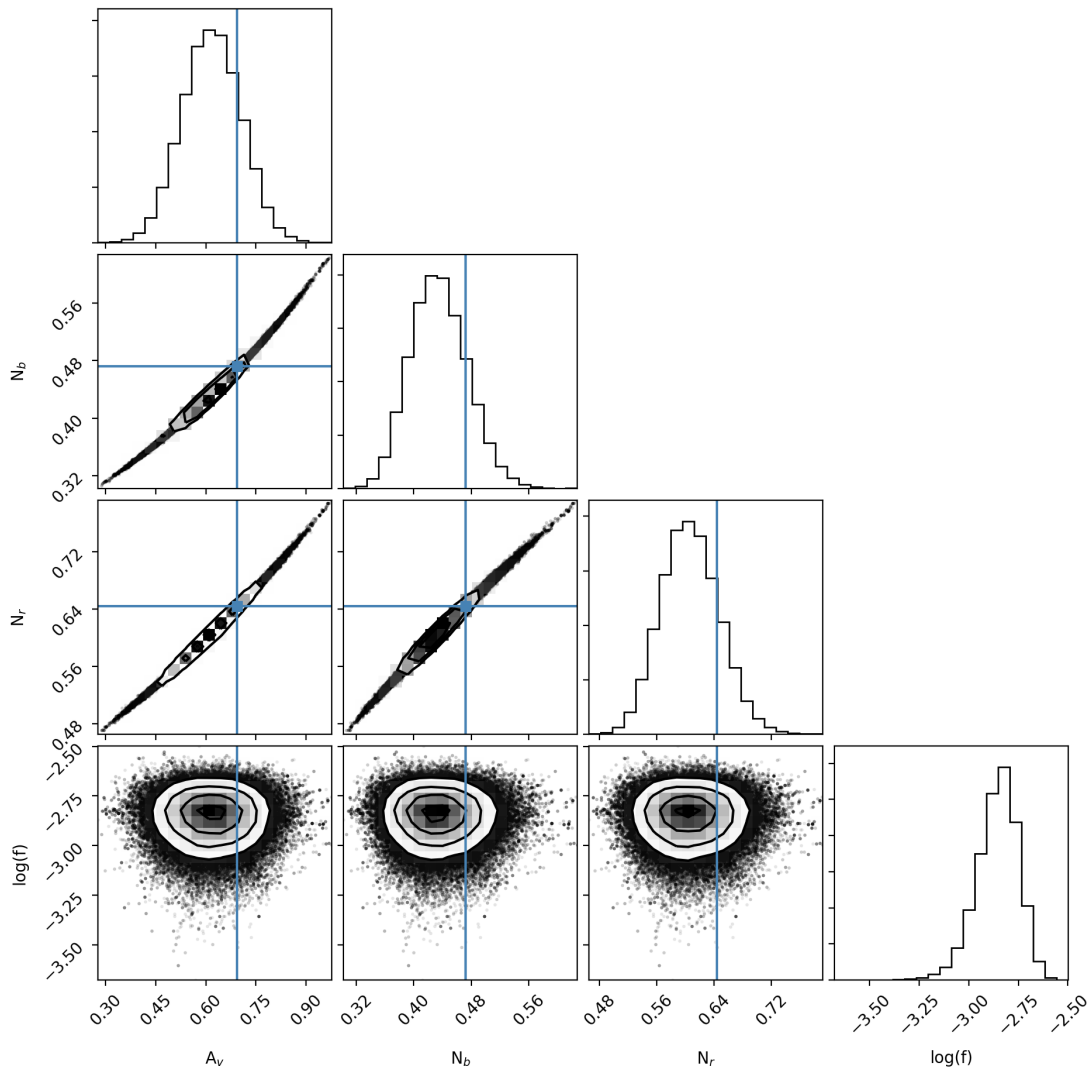
Figure 26: Corner plots of the posterior probability distribution for all four parameters (as is in Fig.21). The blue lines are the true values for each of the parameters which were used to build the spectrum. The main three parameters show a much stronger correlation than they did in Fig.21. The true values for the parameters fall along these two-dimensional correlations which verifies the MCMC fitting algorithm's ability to retrieve sensible estimates. The posterior distributions for each of the parameters appear approximately Gaussian, except for log f which is as expected as it is non-linear.

.

The results so far indicate the algorithm is performing as intended and the shape of the masked spectrum is much simpler to model. In order to test if the redshift has any unintentional impact of the model I repeated this simulation, but this time assuming a source at redshift 0 (i.e. the emitted spectrum). Fig.27 shows the best-fit model around the $H\beta$ and $H\alpha$ regions for both $z = 0.1$ and $z = 0$. For a fixed range of velocity relative to the emission line centre, the higher redshift source will span a larger wavelength range in the

observed frame. This should be the only difference in the data between the two redshifts, hence the algorithm should return very similar parameter estimates.

(a) Best model of the Hβ region for $z = 0.1$

(b) Best model of the Hα region for $z = 0.1$

(c) Best model of the Hβ region for $z = 0$

(d) Best model of the Hα region for $z = 0$
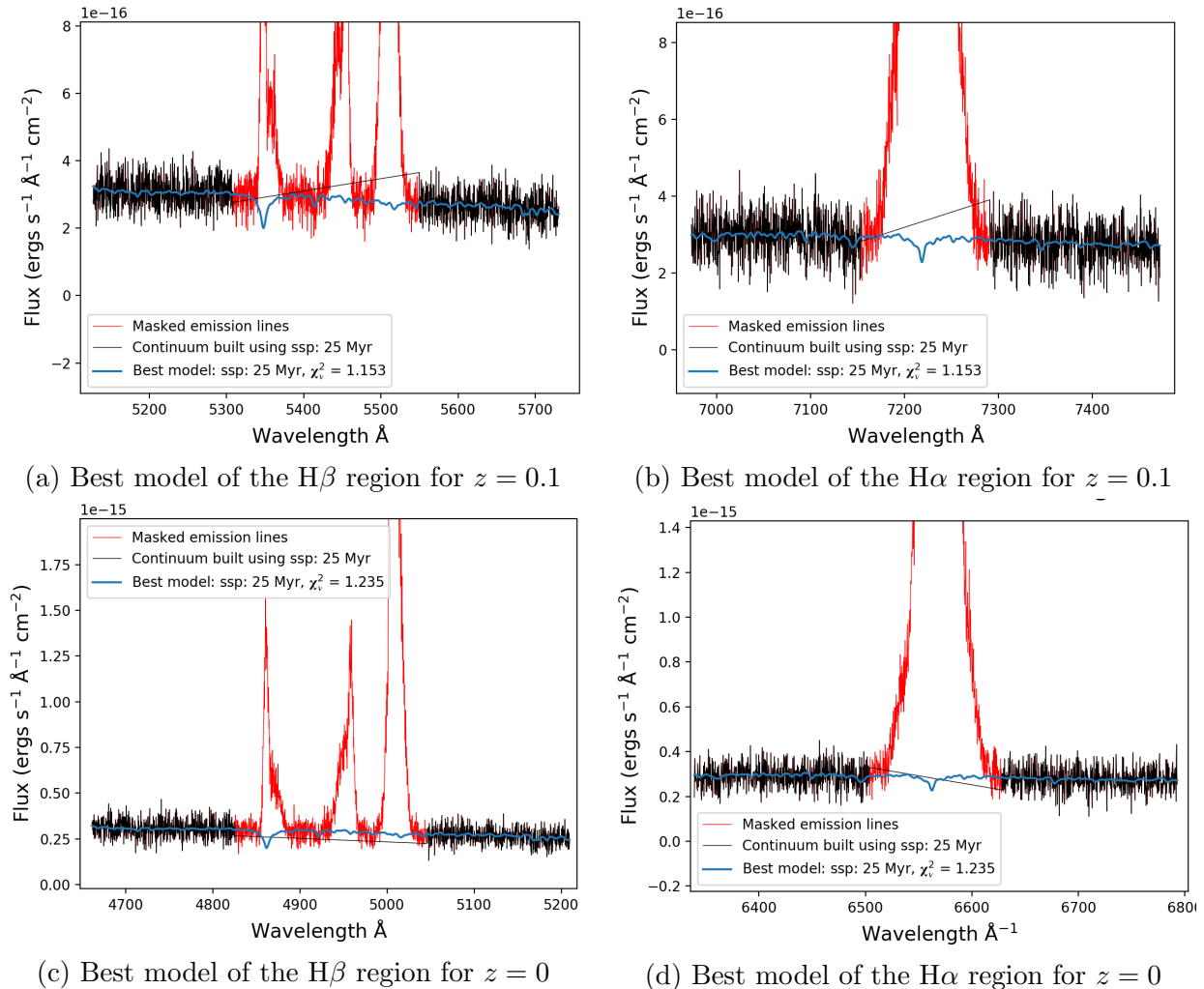
Figure 27: Fig.27a shows the Hβ region for $z = 0.1$, Fig.27b shows the Hα region for $z = 0.1$, Fig.27c shows the Hβ region for $z = 0$, and Fig.27d shows the Hα region for $z = 0$. The best-fit model is represented by the blue line in each figure, the OPR3 spectrum is plotted in black and the masked emission lines (i.e. the data which is not used to fit the continuum) are plotted in red. The OPR3 spectrum is a line plot, hence the straight black line which crosses the masked region does not represent structure, it simply connects two scatter points either side of the masked region.

The χ_ν^2 for both $z = 0$ (1.235) and $z = 0.1$ (1.153) indicate that both the fits adequately model the continuum in these regions. The redshifting has been correctly applied, since the template has been correctly shifted and the mean posterior parameter estimates for both the fits are in agreement. Table 2 presents the parameter estimates for the best-fit model of $z = 0$ and $z = 0.1$ along with the true values. The parameter estimates for both the redshifts are in agreement as they fall within 1σ of each other, and the fractional uncertainty is at most 0.1, further indicating that the redshift has been correctly applied.

z	A_v	N_b	N_r	log f
0	0.725 ± 0.097	0.4862 ± 0.048	0.6596 ± 0.0477	-2.571 $\pm$ 0.069
0.1	0.705 ± 0.0947	0.4777 ± 0.0413	0.6496 ± 0.0427	-2.609 $\pm$ 0.0728
True:	0.693	0.4719	0.6435	-2.303

Table 2: Mean posterior estimates of the parameters of the best-fit template for $z = 0$ and $z = 0.1$ along with their uncertainties. The true values are presented in the last row for comparison.

There are three more aspects to consider; the reproducibility of the parameters, their uncertainties and the local minimum test. The starting values of the walkers are normally distributed around a given value and σ, and each walker converged and formed a Gaussian for the main three parameters, so I am already confident that the algorithm is not being effected by local minima. Nevertheless, I have perturbed the starting positions of the parameters to see if it significantly changes the outcome of the algorithm. Fig.28 presents the fits of four models using the same template (ssp: 25 Myr) with different initial positions for all four parameters. Factors (I_f) of 0.6, 0.8, 1.2 and 1.4 of the initial values are used. All four fits in Fig.28 are consistent with each other and have the same χ^2_ν as the original fit (1.1528).
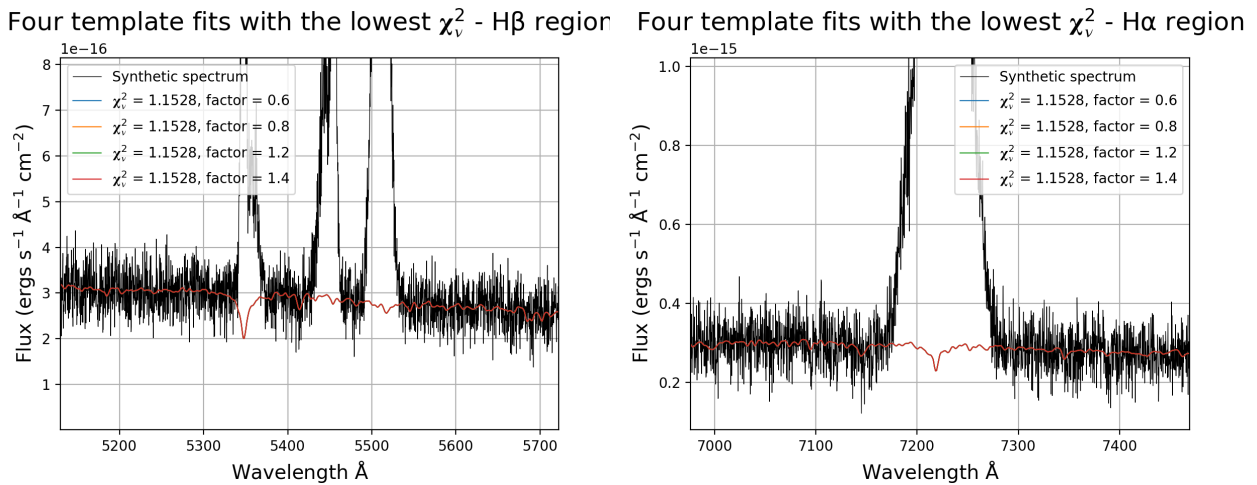
Figure 28: Four continuum fits around the Hβ and Hα regions with different initial positions for the parameters. Each of the fits are indistinguishable from each other at the relative scale of the continuum. Therefore changing the initial value has a negligible effect on the fit; this is quantitatively reflected in the χ^2_ν values which are all equal to 4 decimal places. The parameter estimates for each fit are presented in table 3.

The results of the four fits in Fig.28 are presented in table 3, along with the results of the original fit and the true values. The estimates for each parameter for all five of the fits are in agreement with each other as they fall within range of their 1σ uncertainties. The fractional uncertainty for each estimate is 0.1, which indicates they are representative of the true values since their probability distributions have tightly converged around each posterior mean. The majority of the true values for the main three parameters fall within 1σ of the

I_f	A_v	N_b	N_r	f
0.6	0.617 ± 0.089	0.4335 ± 0.0399	0.6053 ± 0.0408	0.058 ± 0.006
0.8	0.614 ± 0.090	0.4321 ± 0.0403	0.6039 ± 0.0411	0.058 ± 0.006
1	0.618 ± 0.088	0.4336 ± 0.0398	0.6054 ± 0.0406	0.058 ± 0.006
1.2	0.616 ± 0.091	0.4330 ± 0.0410	0.6049 ± 0.0419	0.058 ± 0.006
1.4	0.618 ± 0.089	0.4338 ± 0.0403	0.6056 ± 0.0411	0.058 ± 0.006
True:	0.693	0.4719	0.6435	0.1

Table 3: Mean posterior estimates of each parameter and their uncertainties for different factors of the initial positions (I_f): 0.6, 0.8, 1.2 and 1.4. The true values are given in the final row for comparison.

posterior means estimate, and all of them fall within 2σ (excluding f). These results suggest that the algorithm is unlikely to be affected by changes to the initial values, it is not getting stuck in local minima, the parameter estimates are reproducible for the same set of data and the uncertainties indicate that the results are reliable.

Further tests were completed to verify the MCMC algorithm: higher z values, a range of SNRs, Hβ and Hα regions which both fell on the red spectrum and using other templates to build the spectrum. A test was done where the input values remained the same and the only difference was the template used to build the spectrum. I attempted to fit each template to all 13 of the synthetic spectra, and all but one, ssp: 2.5 Gyr, selected the best-fit template as the one used to build it. ssp: 2.5 Gyr is one of the reddest templates, which means that, with a large enough A_v and a low enough SNR, most the other templates could be used to better model it. If an incorrect template is used to remove the continuum then the main drawback is that A_v will not be correctly returned. Unfortunately there is no way of knowing which is the correct template for the OPR3 spectra, nor the real data. This is already a consequence of fitting a partial spectrum since one of the implications of increasing the degeneracy of the optimisation problem is a lower probability of returning the real parameters.

A_v is very strongly correlated with N_b and N_r, therefore an incorrect template could have a significant effect on all three parameters and consequently on the offset correction of the blue spectrum. There is no way at this point to avoid that problem. If it turns out to have a considerable impact on the results, any spectra where the Hβ region falls on the blue spectrum can be cut from the sample. The line ratios from these samples can still be used for the BPT-NII diagram, however their SFRs cannot be corrected for dust using the Balmer decrement as the Hβ line is required.

6.4 Line fitting of simplified model spectra

Once the continuum has been removed an attempt is made to correct the blue spectrum and its standard error array for inconsistent flux calibration using the estimated N_b/N_r ratio (0.7372) in preparation for the fitting of the emission lines. The error in the ratio dominates the systematic errors in the standard error array, therefore it is accounted for after the line fitting once the integrated fluxes are calculated. The corrected spectrum is displayed in Fig.29; these data will be used to fit the lines. 96% of the noise in the corrected spectrum

falls within a 2σ error which indicates the continuum has been correctly removed, especially considering σ is underestimated by f = 0.1.
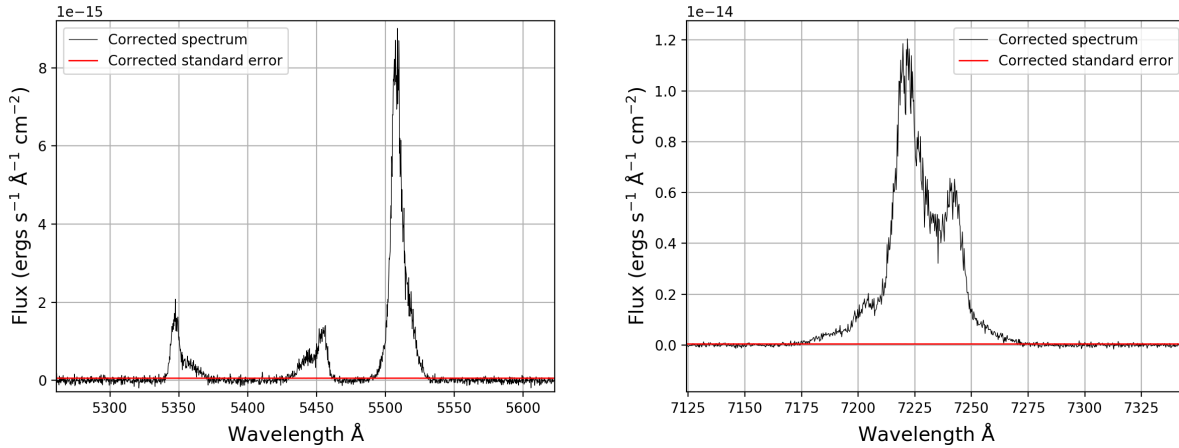
Figure 29: Continuum subtracted and offset corrected (offset as a result of the flux calibration issue) synthetic spectrum in the Hβ and Hα regions, represented by the black line and the red line is the offset corrected standard error array.

Fitting the emission lines simultaneously is a 22-dimensional optimisation problem, hence the number of steps in a chain is now increased to 5000 as a much longer burn-in is expected for the parameters to converge. The best-fit model for the corrected spectrum in Fig.29 is presented in Fig.30; where a corrected spectrum is defined as continuum subtracted and the N$_b$/N$_r$ ratio is applied to the blue spectrum to remove the offset caused by the inconsistent flux calibration.
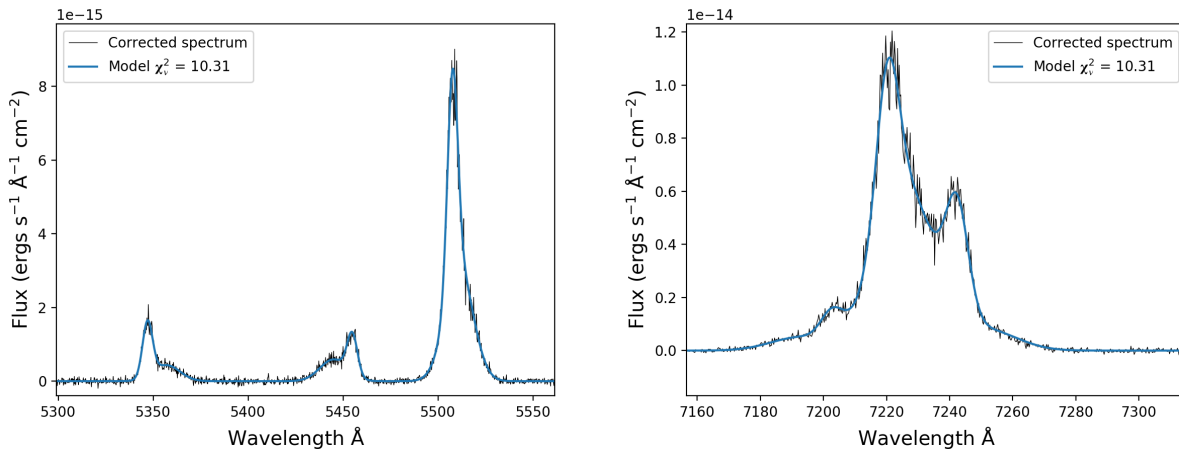
Figure 30: Emission-line fitting of the Hβ and Hα regions; the model is represented by the blue line and the corrected spectrum by the black line. The χ^2_ν of the best-fit model is 10.31.

The χ_ν^2 for the line fitting is larger than the continuum fitting due to the strength of the lines influencing a larger underestimation of the noise in the standard error array. The SNR(Hβ) is 9.8 with a χ_ν^2(Hβ) of 8.46 and the SNR(Hα) is 47.44 with a χ_ν^2(Hα) of 64.06; where (Hα) and (Hβ) refers to the immediate wavelength range of $\pm 35 \times (1 + z)$ around the emission lines in each of the regions. The flux was normally distributed with σ equal to a tenth of the flux (refer to Fig.22b) in order to model the standard errors underestimation of the noise. Since a factor of the flux is used to distribute the data and the synthetic standard error array is independent of wavelength or signal strength, the noise underestimation will correlate significantly with the strength of the emission lines. Consequently, the χ_ν^2(Hα) is much larger than the χ_ν^2(Hβ) as the difference between the data and the model is more significant and cannot be accounted for by the standard errors. The RMS array for the OPR3 spectra is significantly more sophisticated than the standard error array produced for this synthetic spectrum; therefore, I expect the χ_ν^2 of the emission lines in both the regions of the OPR3 spectra to be more in agreement. The χ_ν^2 statistic is not always an informative way of determining whether a fit is acceptable, therefore, taking the above statements into consideration, a χ_ν^2 of 10.31 for the entire fit is reasonable. Furthermore, from a visual perspective, the fit clearly models the spectrum as it falls between the data points. I would not expect the average χ_ν^2 of the OPR3 spectra to be as high as 10.31 as the RMS array is not expected to underestimate the noise by such a large factor and the uncertainties will correctly account for the strength of the lines.
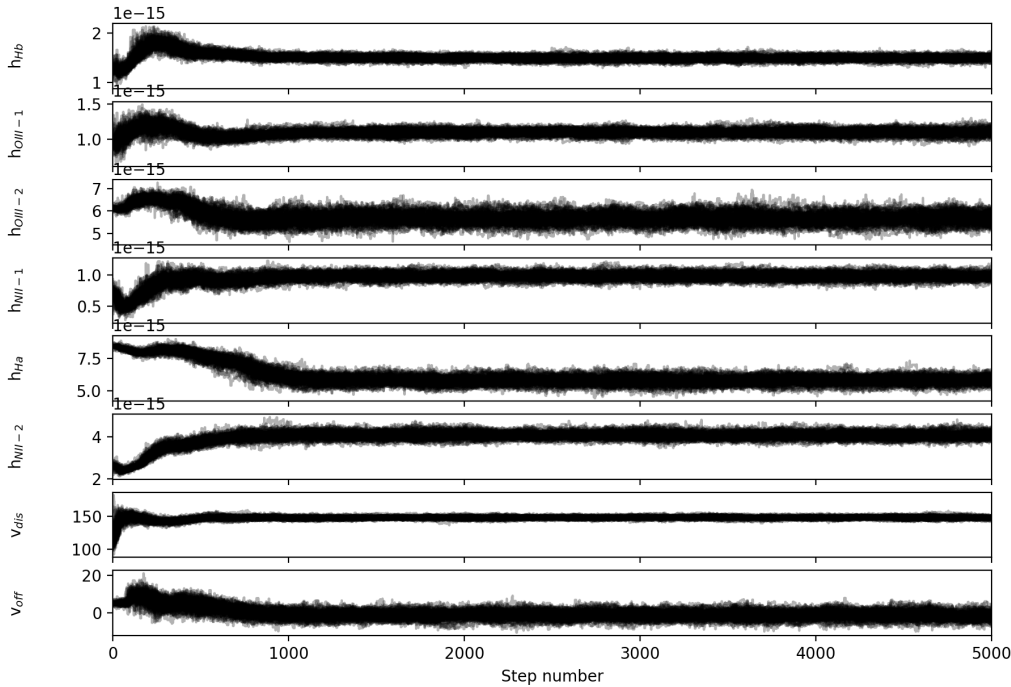
(a) Sampler chains of the emission line parameters.
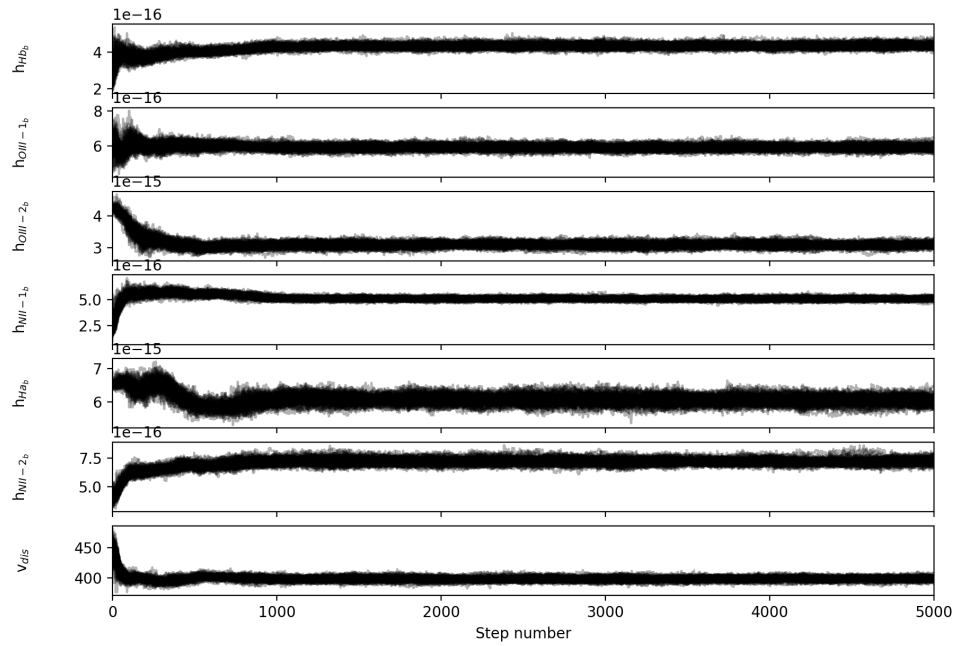
(b) Sampler chains of the broad line parameters.
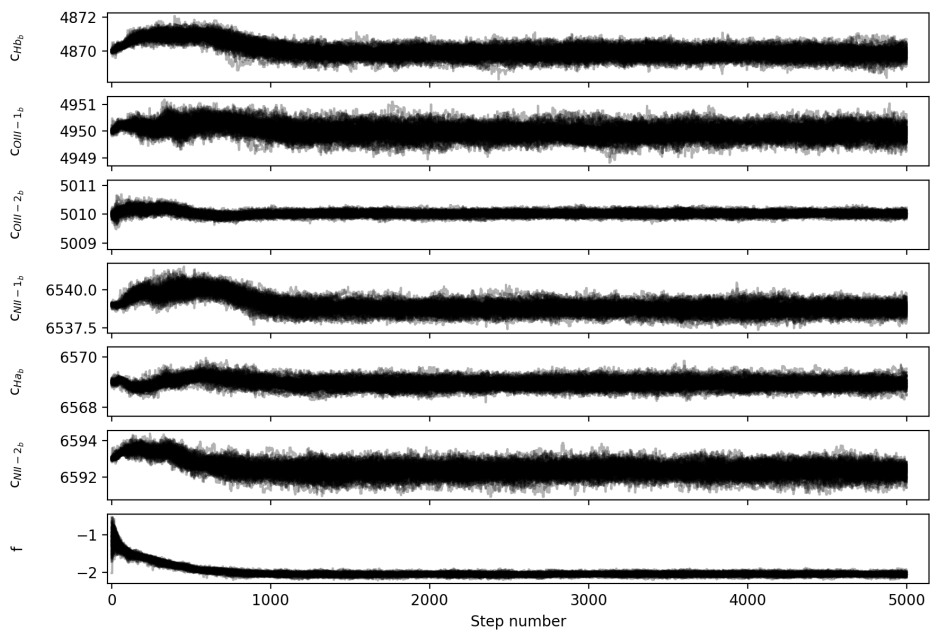
(c) Sampler chains of the broad line centres and log f.

Figure 31: The positions of each walker as a function of the number of steps in the chain. The walkers start of at their assigned initial position, as listed in section 5.5, and begin to explore the full posterior distribution. Each sample is well burnt-in by 1000 steps; a higher factor of 2000 is removed from the sample of 5000 steps.
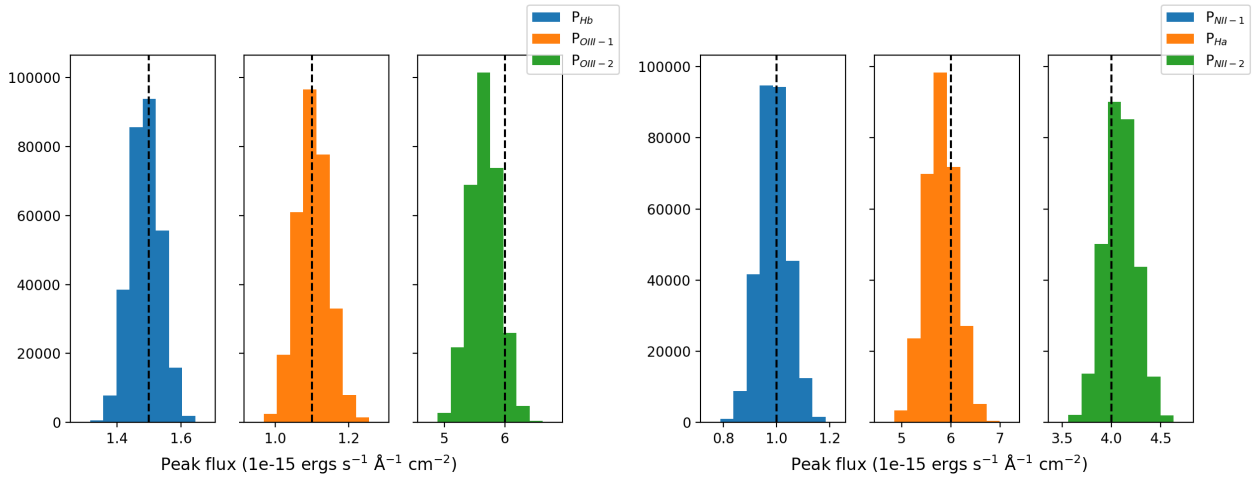
(a) Peaks for Hβ, OIII-1 and OIII-2.

(b) Peaks for NII-1, Hα and NII-2.
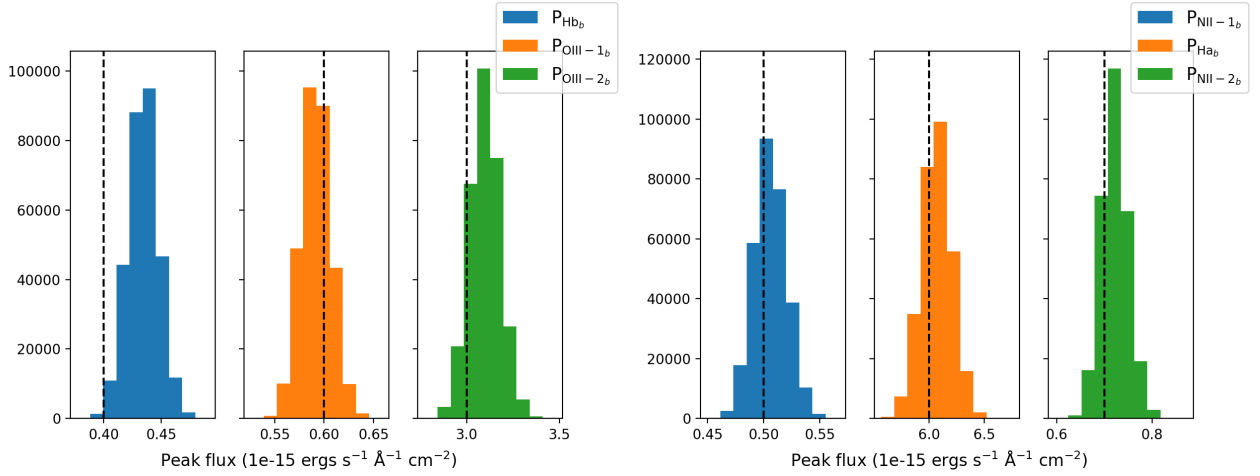
(c) Peaks for broad Hβ, OIII-1 and OIII-2.

(d) Peaks for broad NII-1, Hα and NII-2.
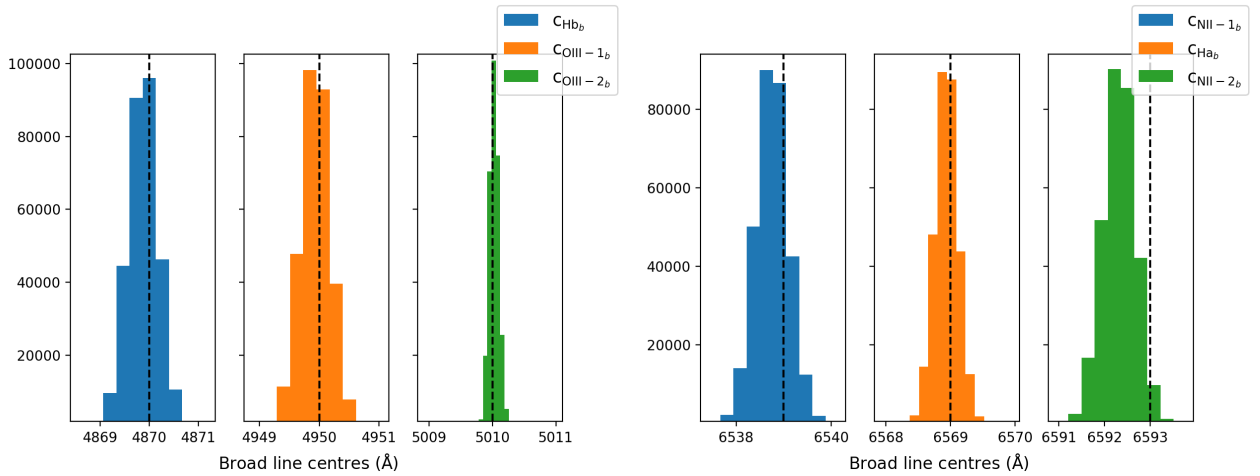
(e) Centres for broad Hβ, OIII-1 and OIII-2.

(f) Centres for broad NII-1, Hα and NII-2.
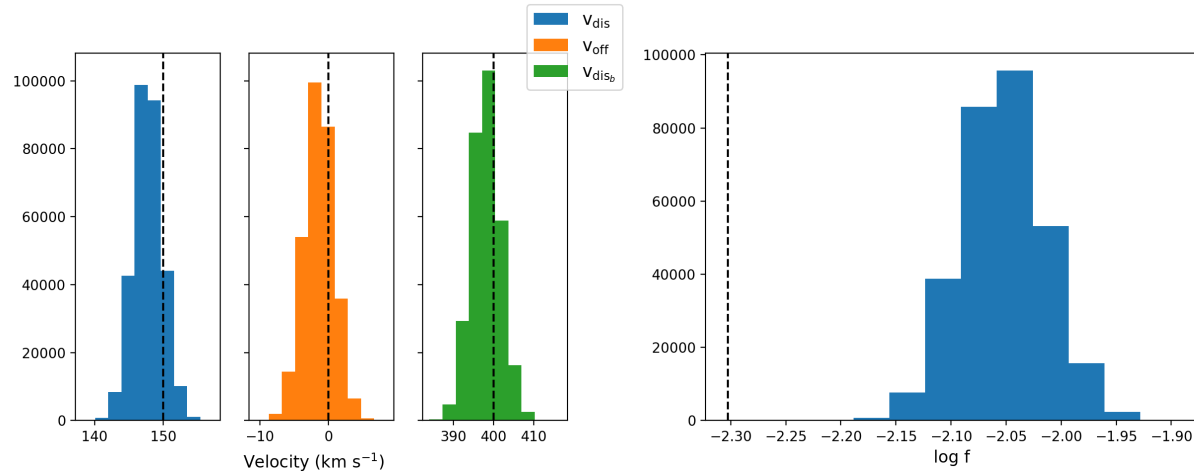
(g) σ_{v}, v and σ_{v_b} for the narrow and broad lines. (h) Fraction underestimated by the error, log f.

Figure 32: Posterior distributions are displayed for the Gaussian peaks of the emission lines (a, b), the Gaussian peaks of the broad lines (c, d), their line centres (e, f), the velocity dispersion for the narrow and broad components, the velocity offset of the emission lines (g) and log f (h). The dashed black lines overlaid on each of the histograms are the true input values for the parameter.

As can be seen in Fig.31, a burn-in of 1000 steps would be adequate for this particular fit, however I selected a standard automatic burn-in of 2000 steps for the line fitting algorithm due to the high dimensionality of the optimisation problem. Despite the dimensionality, all of the 22 parameters successfully managed to converge around an estimate and sample values within a close proximity. A corner plot is not the best way of presenting the marginalised distributions of such a large quantity of parameters. Instead, the histograms of the one-dimensional distributions for each parameter are displayed in Fig.32.

All of the distributions appear Gaussian and do not come into conflict with their priors. The true values for each parameter, excluding log f, fall within the 99% credible intervals of their posterior distributions. The algorithm has been able to return the true value for 18 of the parameters within a 1σ credible interval; this is very encouraging as it indicates the MCMC fitting algorithm is capable of handling the 22-dimensionality optimisation problem. The line fitting algorithm was repeated with various initial positions and, just like the continuum fitting algorithm, MCMC returned parameter results for each fit which were in agreement. The algorithm was also tested with a range of redshifts, SNRs and templates as well as Hβ and Hα regions which both fell on the red spectrum; they all resulted in reproducible and reliable results.

7   OPR3 spectrum fitting

7.1   Continuum fit of the OPR3 spectra

I made use of the University of Hertfordshire's high-performance computing facility to fit the continuum of all 1471 spectra in my sample using the multiprocessing module in Python. The continuum fitting algorithm was provided with the masked spectrum, the RMS array, redshift, index which separates the two regions and the spectrum $H\beta$ is situated on. The script saves the sampler, mean and 1σ of the posteriors, χ^2_ν and the best-fit template of the continuum.
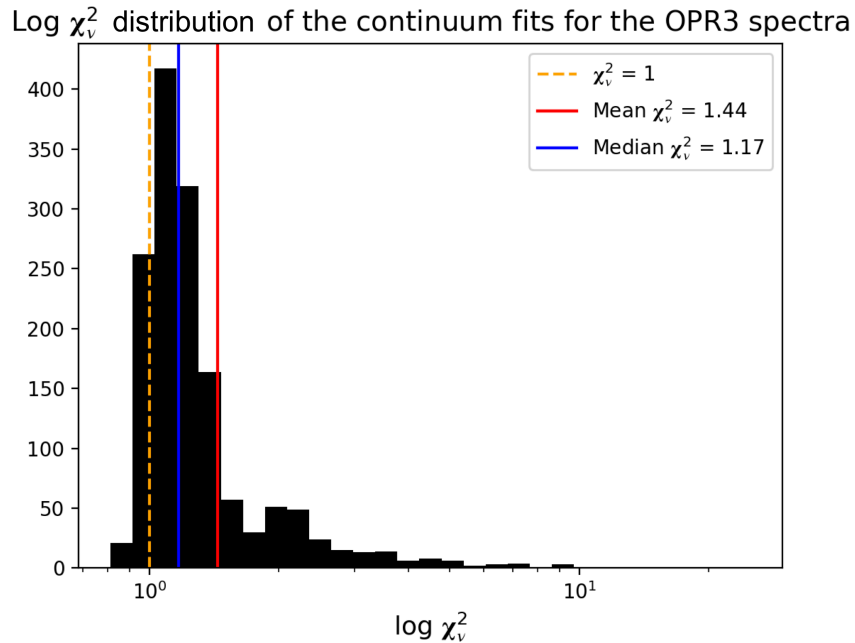
Figure 33: The logarithmic distribution of the χ^2_ν of each of the continuum fits in the OPR3 sample. The largest $\chi^2_\nu = 25.02$ and and the smallest $\chi^2_\nu = 0.81$.

The logarithmic distribution of the χ^2_ν for all the OPR3 continuum fits is presented in Fig.33. The distribution skews towards high values and has many outliers beyond $\chi^2_\nu = 5$, influencing a larger mean. The median is a better representation of the central tendency as it is unaffected by large numbers which makes the mean misleading. Nevertheless, both statistics show an encouraging average for the fits. There are only 20 spectra out of the 1471 with a $\chi^2_\nu > 5$. During my investigation of these high χ^2_ν fits I found a number of structures which were not masked or modelled by the continuum: these include the rare presence of the OI 6300 Å emission line in the $H\alpha$ region, skylines at 5890 Å (Na), 6300 Å (OI), 6365 Å (OI) and between 6865 - 6920 Å and skyline reduction issues at long wavelengths leaving behind high signal residuals. Any spectra where these structures have not been correctly subtracted and are superimposed on top of emission line flux are removed from the sample.
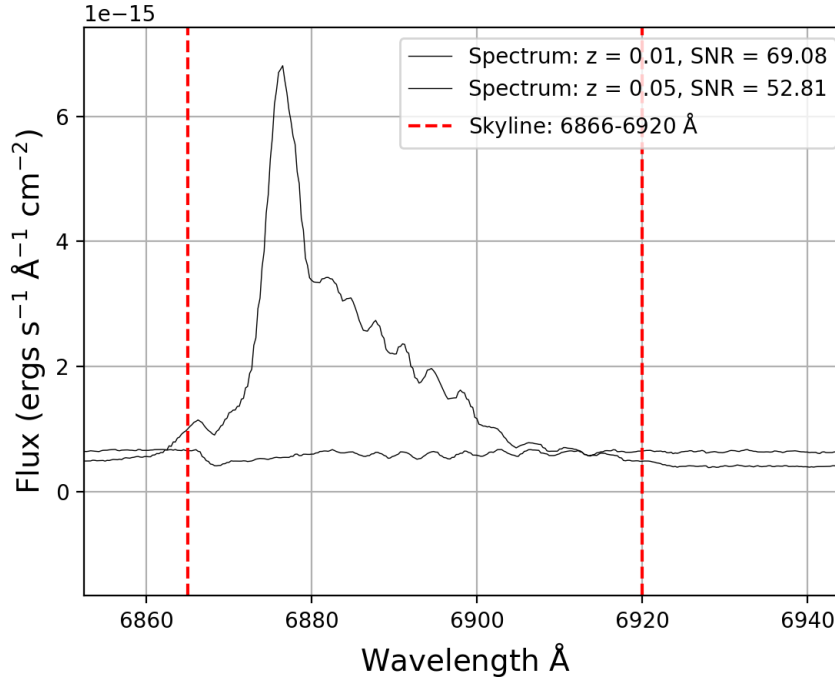
Figure 34: Wavelength range of the skylines between 6865 - 6920 Å for two spectra. One has a redshift ($z = 0.01$) which places the skylines in the continuum to the right of the emission lines in the Hα region, and the other has a redshift ($z = 0.05$) which superimposes the emission lines on top of the absorption features. Both of the spectra have a large SNR which indicate that the skylines have a large signal and are not the result of noise.

Fig.34 illustrates two spectra where the skylines between 6865 - 6920 Å are strong and have not been correctly subtracted. The redshift of one of the targets places the Hα emission lines within this wavelength range; these absorption features have a significant impact on the emission line flux and their Gaussian profiles, hence any spectra with $0.036 < z < 0.06$ were removed from the sample. The only feature which will be ignored is the OI nebular emission line which very rarely appears in the spectrum at a rest-frame wavelength of 6300 Å. As shown in Fig.35, the fit around the OI line has attempted to model its emission as part of the continuum, resulting in a poor continuum fit and a high χ_ν^2. This region should be masked before fitting the continuum, however due to time restrictions it was not possible to return to the preparation stage. After inspecting fits of spectra which contained a strong nebular OI line, I found it was not required to re-run the algorithm. The algorithm's ability to model the continuum surrounding the emission line flux of the relevant lines is not impacted by the presence of the OI line as it is not within a close proximity to them. As such, the continuum fit will still be subtracted from these spectra and they will remain in the sample. In future work this line should be either modelled along with the other emission lines or masked if possible.
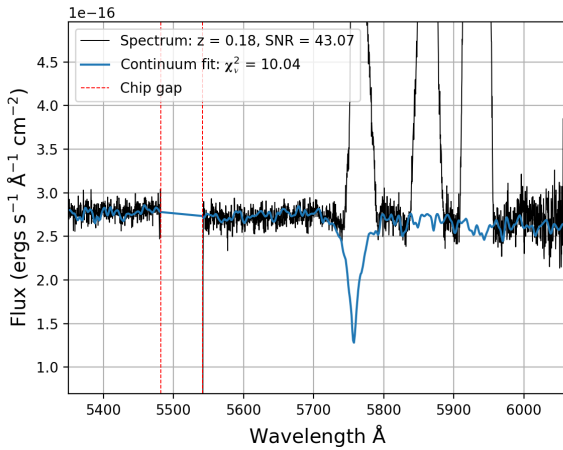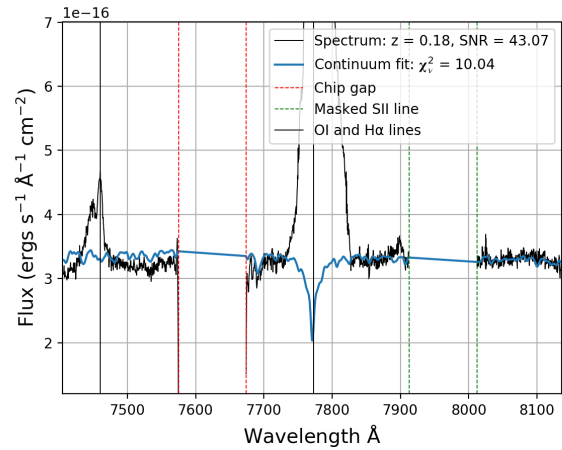
(a) Hβ region of the spectrum. (b) Hα region of the spectrum.

Figure 35: Fig.35b shows the Hα region of a spectrum which contains a strong OI nebular emission line. The observed wavelength of the OI line, which also has a narrow and broad component, and the Hα emission line are indicated by a black vertical line. The chip gap between 7575 and 7676 Å is also present in this region to the left of the Hα line (red dashed lines) and the SII line has been masked out to the right of this region (green dashed lines). The fit around the OI line has attempted to model it as part of the continuum, resulting in a poor fit and a high χ_ν^2. The rest of the continuum has been modelled adequately for both the Hα and the Hβ region in Fig.35a. The other chip gap between 5482 and 5542 Å is also present in this figure.

Fig.36 illustrates two spectra with large residuals from the sky subtraction at high optical wavelengths. These will still be used in the line fitting process and their fits will be analysed once it is understood how the residuals affect the modelling of the emission lines.
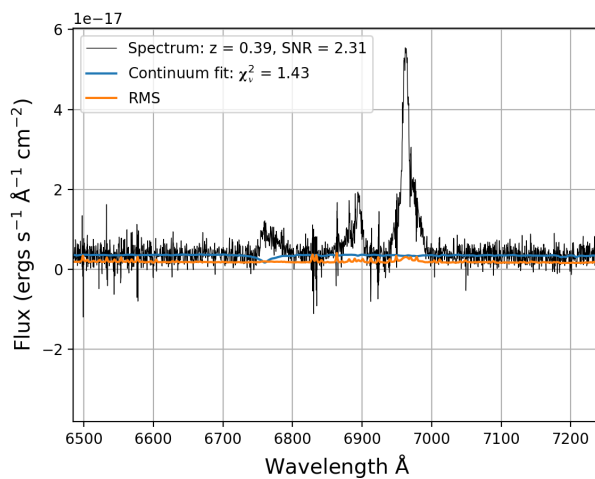
(a) Hβ region of a spectrum with SNR = 2.31. (b) Hα region of a spectrum with large residuals and a SNR = 2.31.
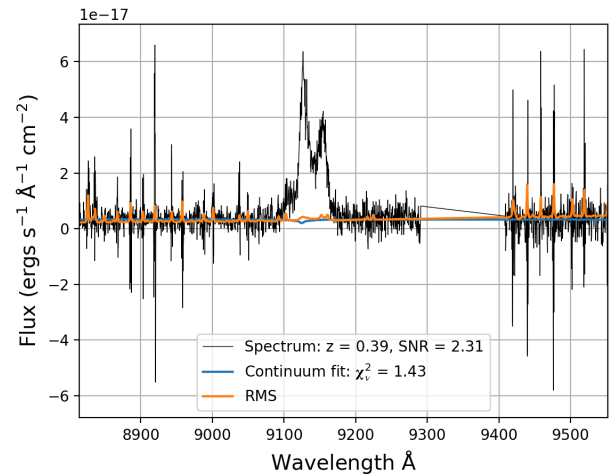
(c) Hβ region of a spectrum with SNR $= 3.59$.

(d) Hα region of a spectrum with large residuals and a SNR $= 3.59$.
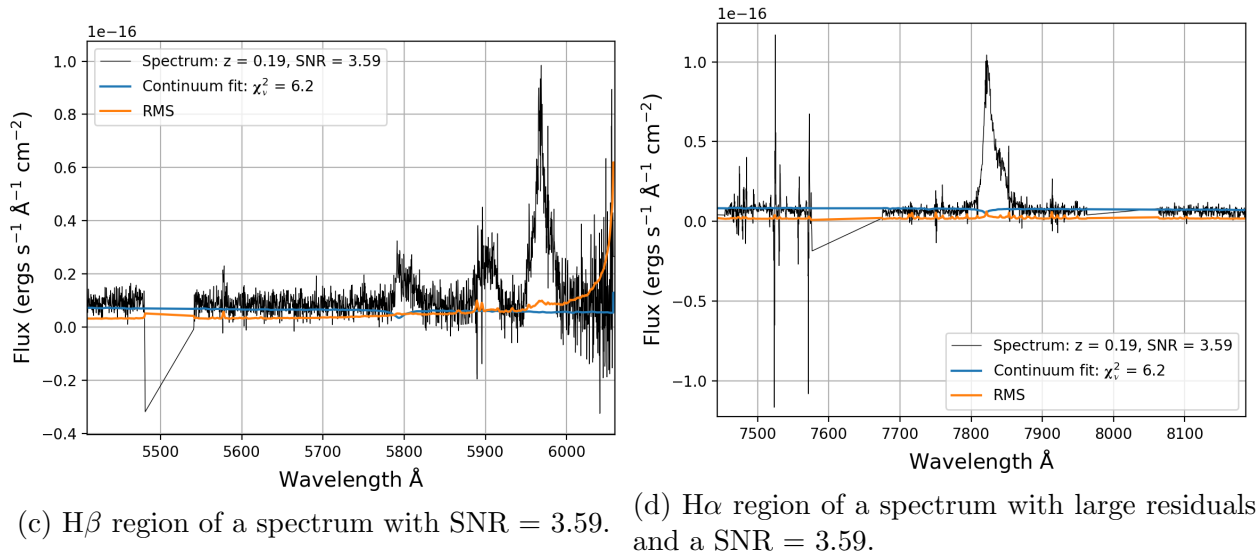
Figure 36: The Hα and Hβ regions of two spectra where the skylines, which are prominent at high optical wavelengths, have not been correctly subtracted, leaving large residuals in the spectrum which are not accounted for in the RMS array. The RMS array of the spectrum in Fig.36a&b accounts for more of the skyline flux than the spectrum in Fig.36c&d, hence it has a lower SNR and χ^2_ν. The Hβ regions do not contain large residuals; however, they are included to demonstrate there are no other features which significantly influence the SNR or the χ^2_ν of the fits.

Once all the normalisation parameters for the continuum fits have been estimated, the distribution of their ratios in the red and blue arms can be analysed. Fig.37a plots the log distribution of these ratios. It does not form a log-normal distribution around a mean value which is either due to low SNR spectra causing the spread or it suggests the cause of the offset affects each spectrum differently and there is no constant correction factor. The majority of the ratios furthest from 1 have a low SNR (< 10), as can be seen in Fig.37b. This suggests that either the noise has a significant influence over the shape of the continuum fitting model or that the calibration issue is somehow related to the noise; whether the offset is linked to a low SNR, or the miscalculation consequently results in low SNR, is not clear. The colour-map of the SNR in Fig.37c on the plot of z (< 0.2) vs the ratios reiterates these findings and localises the smallest ratios to the largest redshifts. The SNR is naturally a lot weaker at high redshifts as these targets are further away and a low SNR can distort the shape of the continuum and consequently return normalisation parameters that are not representative of the offset caused by the calibration. If this is happening then it cannot be avoided, but it can be accounted for by propagating the error of N_b/N_r to the error on the line fluxes.

(a)

(b)

(c)
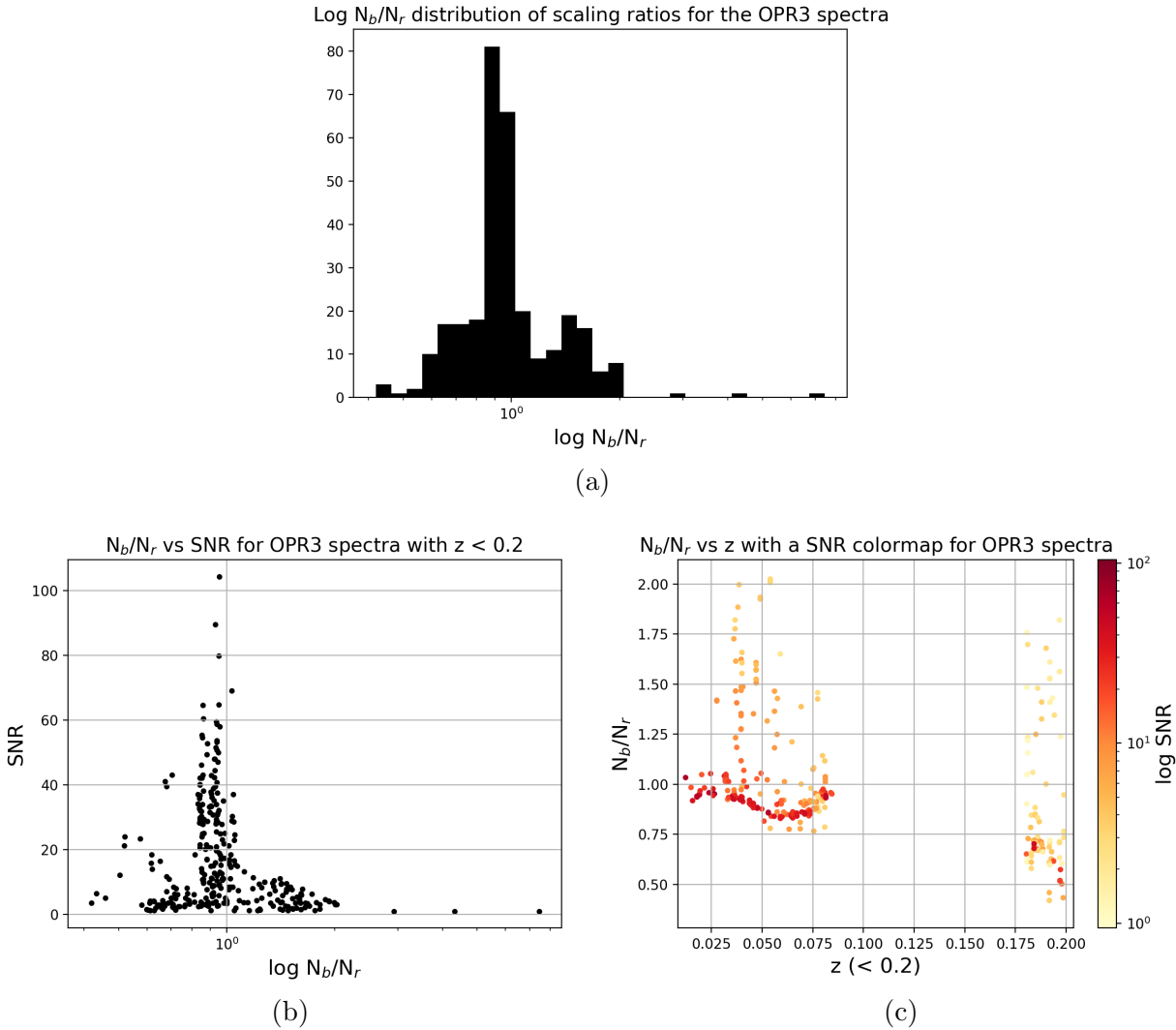
Figure 37: Logarithmic distribution of the N_b/Nr scaling ratios is shown in Fig.37a, it is plotted against the SNR in Fig.37b, and against the redshift in Fig.37c with a colour map of the SNR. The redshift gap in Fig.37b is due to the emission lines aligning with the chip gaps. The Hβ region crosses the overlap between the blue and red spectra when $z > 0.2$, hence the ratios are not calculated for these targets; only 307 of the spectra required an offset correction for the blue spectra.

In summary, the spectra which have so far been removed are those with emission lines contaminated by skylines between 6865 - 6920 Å and the OI skylines at 6300 and 6365 Å. Spectra are filtered based on their redshift falling within the following ranges: $0.0363 < z < 0.0590$ where Hα is contaminated by the 6865 - 6920 Å skylines, $0.2517 < z < 0.2614$, $0.2710 < z < 0.2713$, $0.2940 < z < 0.2986$ and $0.3070 < z < 0.3094$ where OIII-2, OIII-1 and Hβ are intermittently contaminated by the OI skylines. The templates for the 1305 spectra of the 1471 which have not been filtered from the sample are subtracted and offset corrected in preparation for the emission line fitting algorithm. Fig.38, 39, 40 and 41 present the continuum fit and subtraction of four example spectra with varying SNRs.
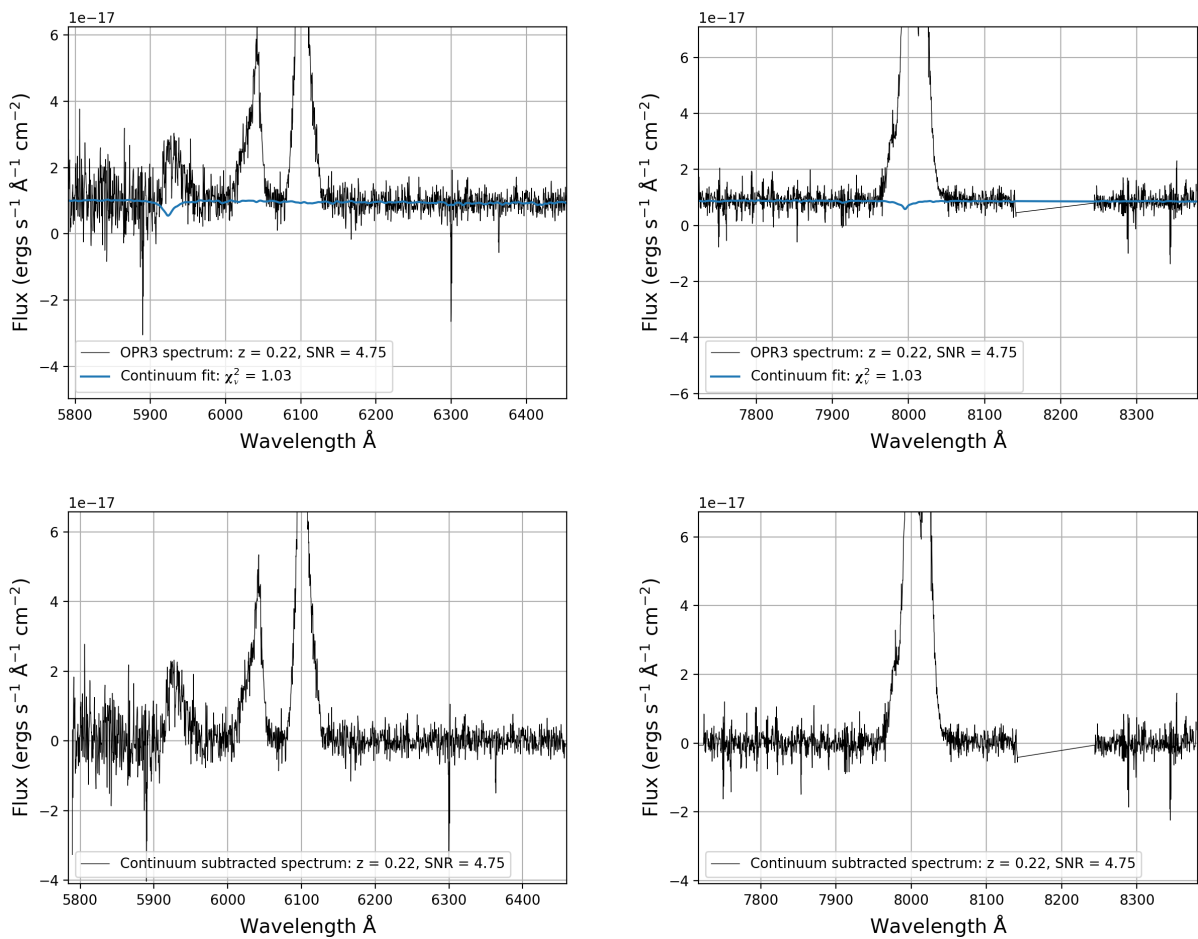
Figure 38: Continuum fit and subtraction of a spectrum with SNR = 4.75. The upper two figures present the best-fit of the continuum in the Hβ and Hα regions respectively. The lower two figures present the continuum subtracted spectrum in these two regions. The masked wavelength range to the right of the Hα lines used to contain the SII emission line.
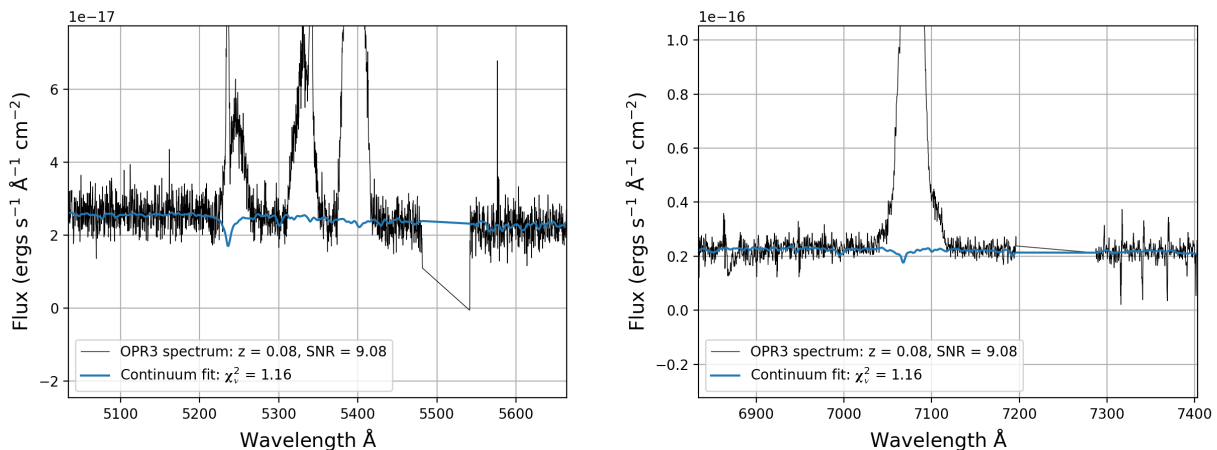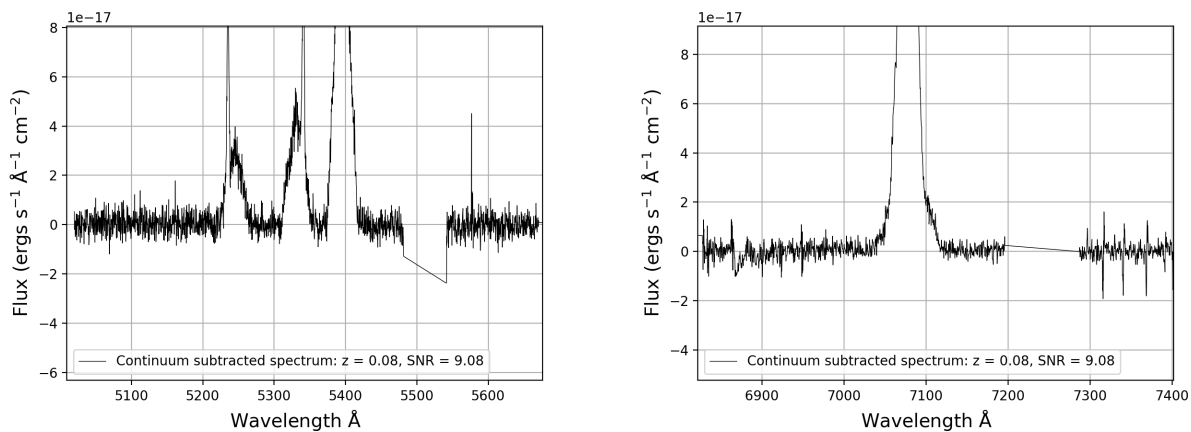
Figure 39: Continuum fit and subtraction of a spectrum with a high SNR of 9.08. The masked wavelength range to the right of the Hα lines used to contain the SII emission line. The masked wavelength range to the right of the OIII-2 line is the CCD chip gap in the blue arm.
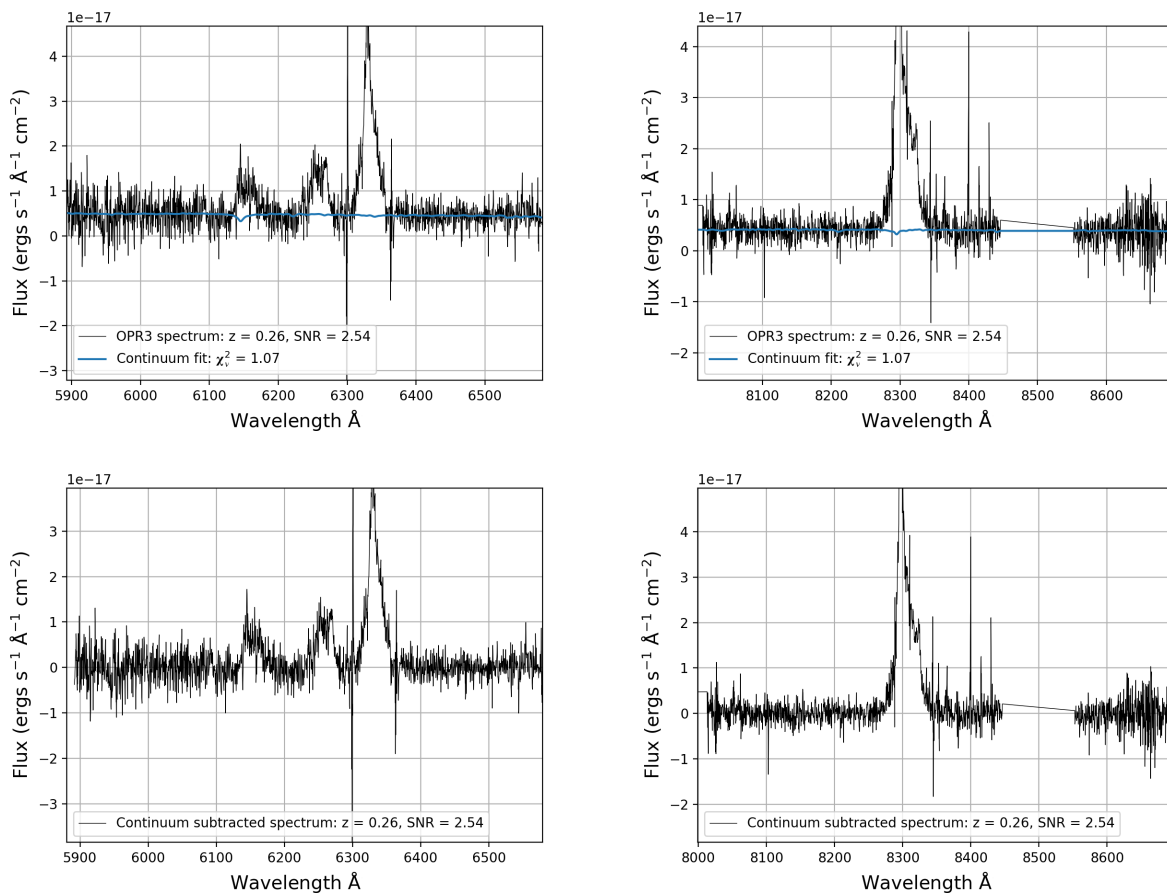
Figure 40: Continuum fit and subtraction of a spectrum with a low SNR of 2.54. The masked wavelength range to the right of the Hα lines used to contain the SII emission line.
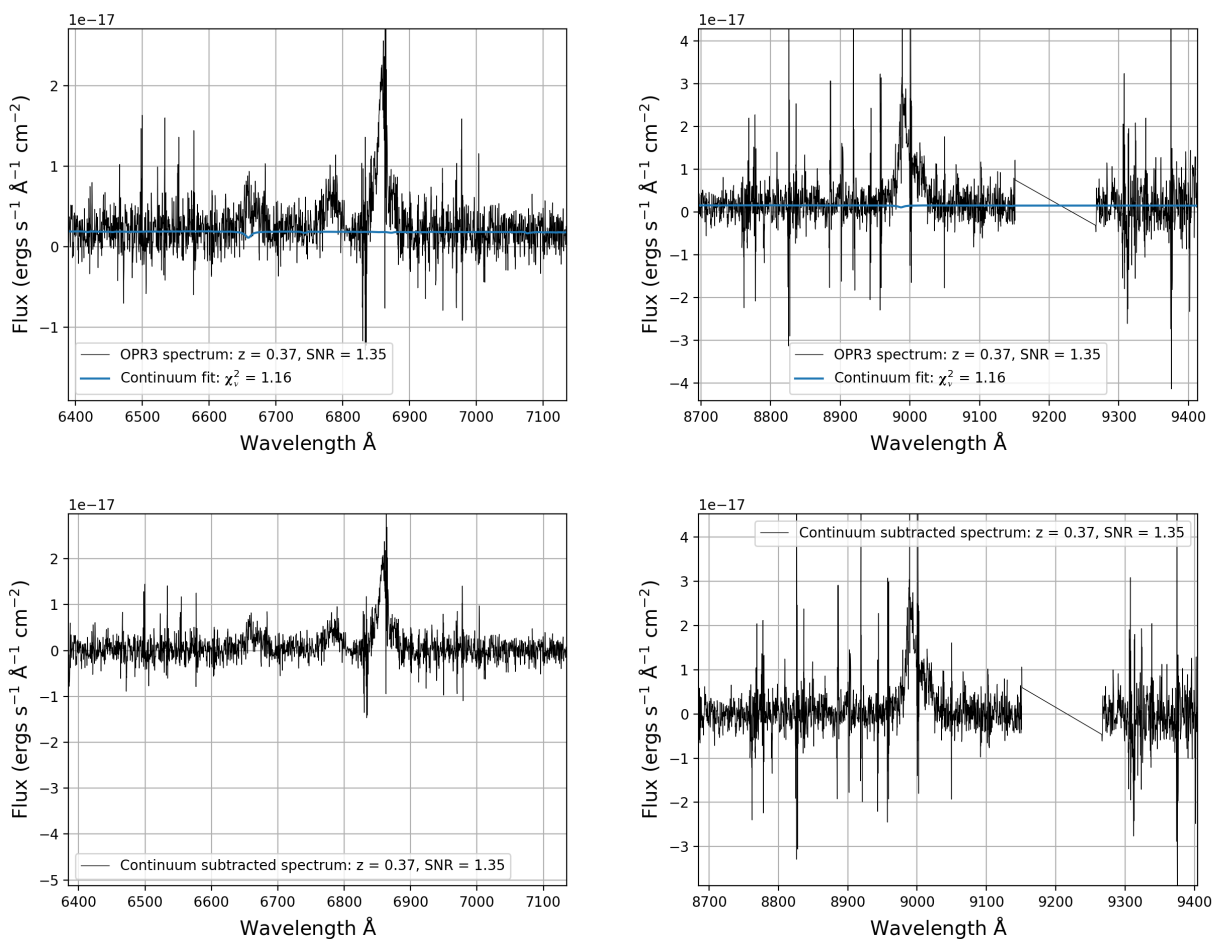
Figure 41: Continuum fit and subtraction of a spectrum with a low SNR of 1.35. The masked wavelength range to the right of the Hα lines used to contain the SII emission line

7.2   Line fit of the OPR3 spectra

Before running the MCMC emission line fitting algorithm on the University of Hertfordshire's high-performance computing facility, I tested it on four high SNR OPR3 spectra to see if I had correctly modelled the broad lines. I became convinced they were non-Gaussian after fitting the lines to these spectra which are shown in Fig.42. All the fits have unsuccessfully managed to model both the broad and narrow components. Instead of a Gaussian-bell shape, the broad lines appear triangular, with flat edges and pointed peaks. This is particularly evident for the peaks and edges of the broad Hβ and broad OIII-1 lines in Fig.42b, the straight edge of the broad OIII-2 line in Fig.42c and the slope of broad Hα line between the Hα and NII-2 narrow emission lines in Fig.42a. The pointed peak of the broad Hα line can also be seen in the bottom left plot in Fig.42a, where a bell shaped Gaussian failed to adequately model its sharp peak and flat edges but successfully modelled its narrow component. It is evident that the MCMC fitting algorithm has managed to retrieve the best parameter estimates for the broad lines using the Gaussian model, but a more suitable model is required for a better fit.
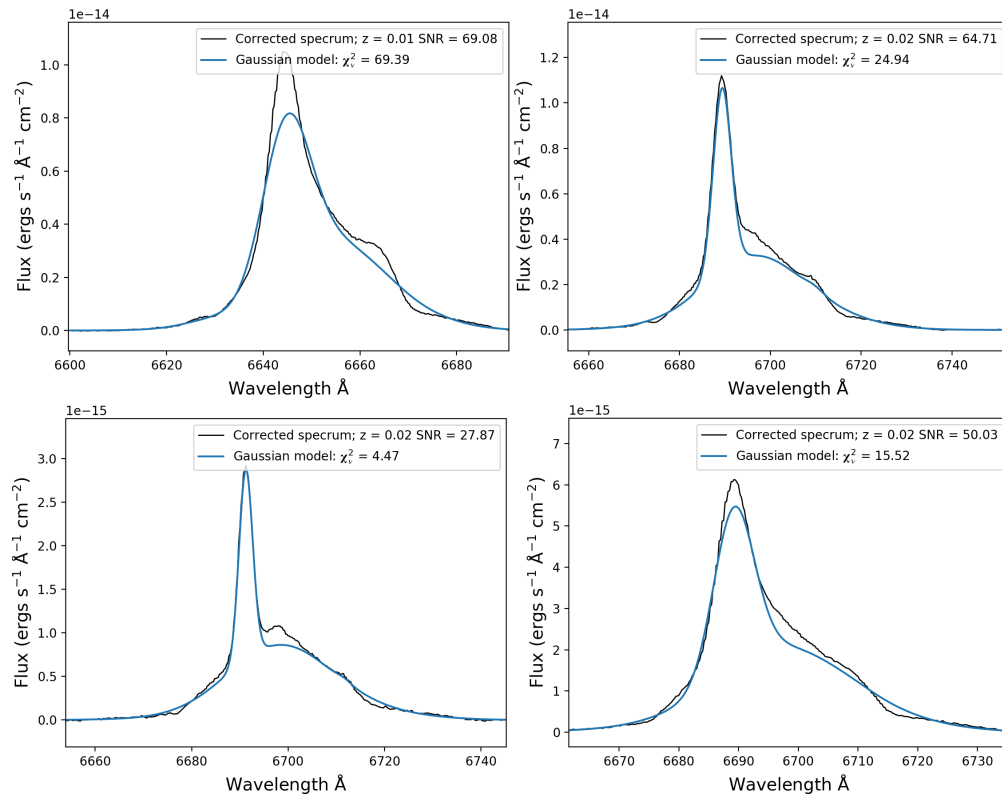
(a) Hα region of the four high SNR spectra (black) and the best-fit (blue) using the Gaussian model for the broad lines.
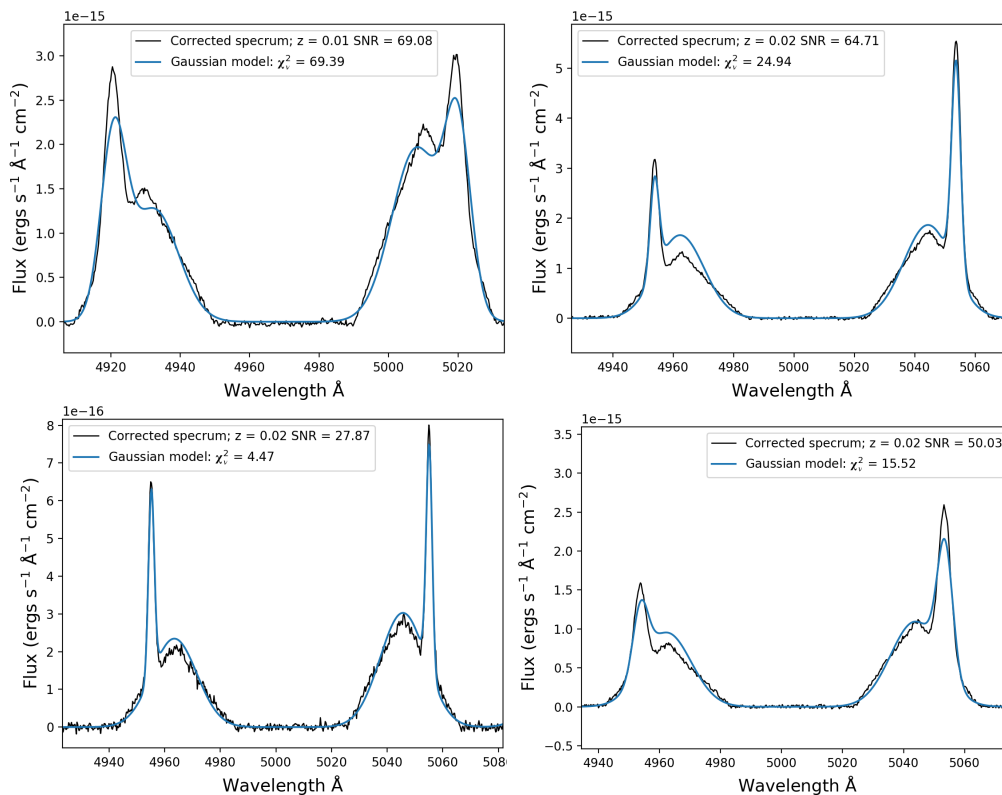
(b) Hβ and OIII-1 narrow and broad components of the four high SNR spectra (black) and the best-fit (blue) using the Gaussian model for the broad lines.
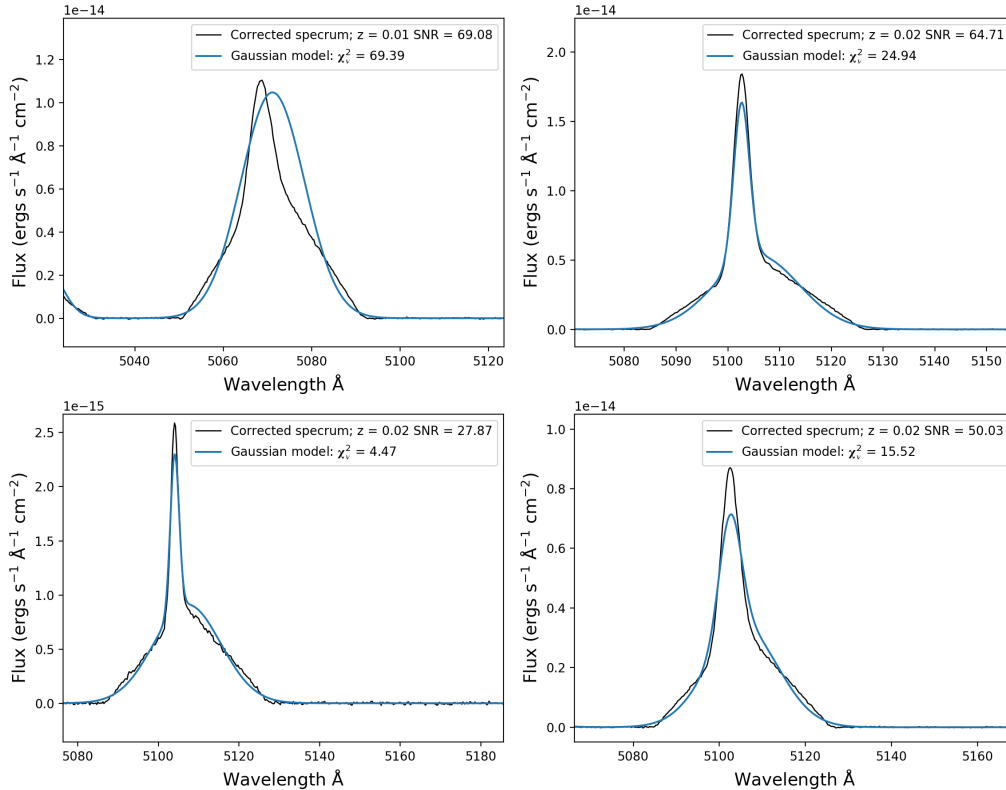
(c) OIII-2 narrow and broad components of the four high SNR spectra (black) and the best-fit (blue) using the Gaussian model for the broad lines.

Figure 42: Displayed are the best-fits of four high SNR spectra using a Gaussian function to model the broad line structures; SNR = 69.08, 64.71, 27.87 and 50.03. The Hα regions of each of the spectra are enhanced in Fig.42a, the Hβ and OIII-1 components are presented in Fig.42b and the OIII-2 components in Fig.42c.

The SNR and the χ_ν^2 for the line fitting has henceforth been calculated using the immediate wavelength range of $\pm 35 \times (1 + z)$ Å from the outer emission lines in each region; in this way the wavelength range primarily targets the emission lines with minimal continuum so that any incorrectly subtracted continuum features, unmasked OI lines or skylines have no influence over the χ_ν^2. The statistics directly measure the data surrounding the narrow and broad lines.

Unlike in the real universe where there are physical explanations for the intrinsic velocity profiles of emission lines that we observe, in the simulations any line profile is theoretically possible. Numerous potential sources of the triangular features were investigated, including the sky subtraction and the flux calibration routines. These broader emission components are dependent on the source redshift, just like their narrow counterparts and the continuum. This is a key feature which can be used to isolate the cause of their production in the OPR3 simulation. As such, this rules out the possibility of their production within the sky subtraction procedure, which is independent of the galaxy's redshift. In order to flux calibrate the spectrum the flux counts must be multiplied by the sensitivity function. This is determined from the spectrum of the calibration targets (white dwarfs) and will first need

to be redshifted before applying it to the galaxy's spectrum. Therefore, the flux calibration procedure is a possible source for the broad line components, as well as the production of the continuum and the narrow emission lines. Following discussions with the people who built the input simulated spectra, we are unable to explain how they have the observed shape, and we therefore make the pragmatic decision to adopt a triangular model. The flux of the broad lines hold no relevant information about the nebular emission, hence it is not necessary to physically interpret them. The only purpose of modelling these structures is to prevent them from influencing the results by selecting the model which results in the best-fit and χ^2_ν.

The fits using the Gaussian model for the four high SNR spectra, shown in Fig.42 are visually and statistically very poor fits. During the fitting process, the priors on each of the parameters were adjusted to provide both a more constrained and relaxed area of parameter space for the walkers; less restrictive priors proved to result in the best-fits. The posterior distribution of the parameters for the majority of the Gaussian model fits followed a normal distribution, hence the set priors were not preventing a more optimal fit. The few cases where a posterior distribution pushed up against the parameters prior were mainly due to a single Gaussian attempting to model two emission lines within close proximity. This most frequently occurred for the narrow and broad line components of OIII-2 since their emission lines centres are only 3 Å apart, thus resulting in the height of one Gaussian peaks parameter tending towards 0 ergs s^{-1} Å^{-1} cm^{-2}. The upper left fit of the OIII-2 narrow and broad emission lines in Fig.42c is an example of a single Gaussian attempting to model both the components; the peak flux posterior distributions of both the components are displayed in Fig.43.
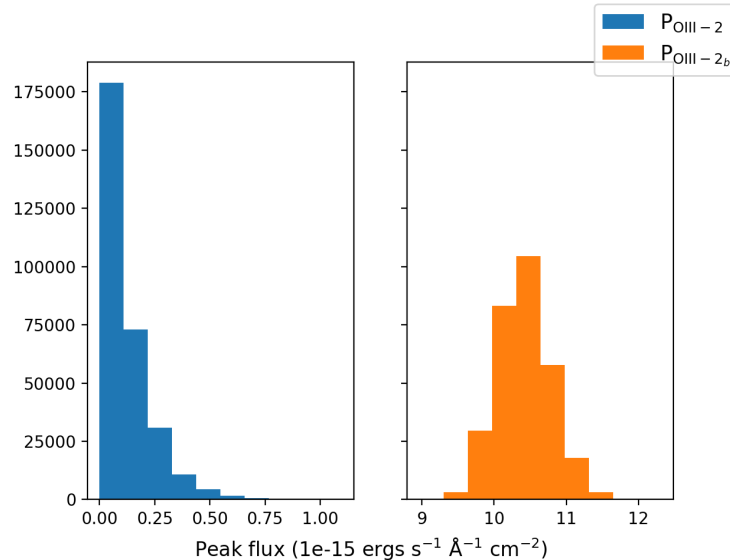
Figure 43: Posterior distribution of the peak flux parameters for the OIII-2 components in the upper left plot in Fig.42c. OIII-2 is pushed up against the zero flux prior which prevents the fit modelling an absorption feature. Due to their close proximity, the Gaussian which is intended to model the broad OIII-2 line has modelled both the components as a singular structure.

The Hβ and OIII-1 broad components in Fig.42b are blended the least with their narrow

counterparts and provide the clearest indication that their line profiles are non-Gaussian. The NII doublet are weak structures and the peaks of their narrow and broad lines cannot be located due to flux blending of all six lines in the Hα region. The only evidence they provide for a triangular profile are the steady linear slopes which trail off from the base of the NII emission lines towards the zero flux point.

The triangular model requires the same number of parameters as the broad Gaussian model; assuming the triangles are congruent (corresponding angles and sides are equal). Other than the function itself, the only difference is that the parameter for the widths (σ) will now be in the unit of Å instead of km s^{-1}, and is instead modelling the width of the triangle at its base (zero flux). The model fits a linear function to either edge of the triangle using the following coordinates ($\lambda_o - \sigma, 0$), ($\lambda_o, 1$), and ($\lambda_o + \sigma, 0$). The two coefficients of a linear equation are extracted, scaled using the peak parameters and used to model the six triangles in the spectrum. The priors for the width are set between 0 and 1000 Å from the initial guess, which is set to 20 Å.

Comparison plots of the two models for the four spectra in the previous figures are presented in Fig.44. The fits using the mean posterior estimates for each model are presented in each plot along with their χ^2_ν. There is a vast improvement visually using the triangular model, which is reflected in the χ^2_ν, as it better models the narrow and broad components in each of the spectra. This test was performed on a further 6 high SNR spectra and 20 low SNR spectra; some of these fits are displayed in Fig.46. The posterior probability distribution comparisons for the two models in Fig.44c are presented in Fig.45. The median value of each distribution is subtracted from the sample so that, if the histogram is Gaussian, the mean of the distribution will align with 0. In this way, their shapes and the spread of the probability distribution can be compared for the two models. The variance in all but two of the posterior distributions are a lot tighter for the triangular model. The peak parameter of NII-1 for the Gaussian model came into conflict with its prior and was clearly modelled by its broad counterpart; the triangular model has successfully managed to differentiate between the two structures. This also appears to be the case for the non-Gaussian NII-2 distribution. The plots clearly show that the triangular function is consistently a much better model for the spectrum throughout every parameter.
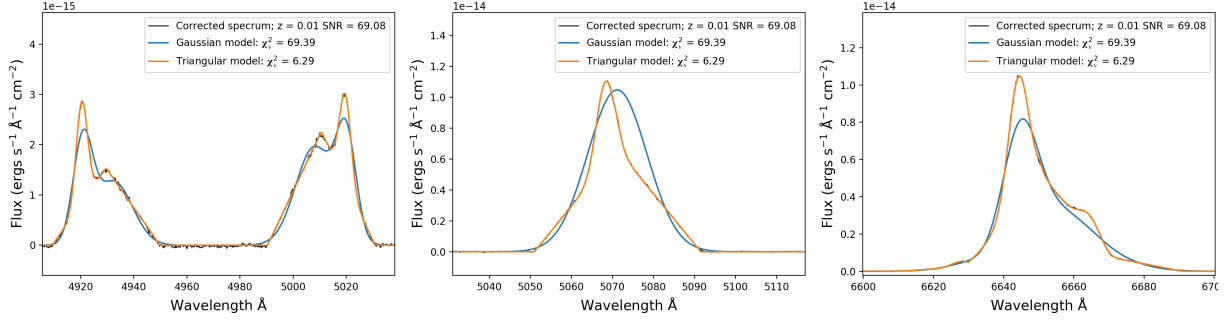
(a) Spectrum: SNR = 69.08, $z = 0.01$. Gaussian model: $\chi_\nu^2 = 69.39$. Triangular model: $\chi_\nu^2 = 6.29$
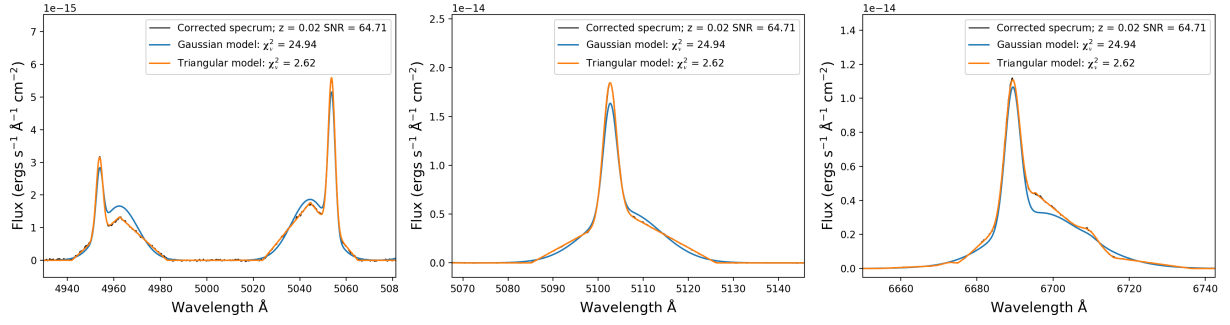
(b) Spectrum: SNR = 64.71, $z = 0.02$. Gaussian model: $\chi_\nu^2 = 24.94$. Triangular model: $\chi_\nu^2 = 2.62$
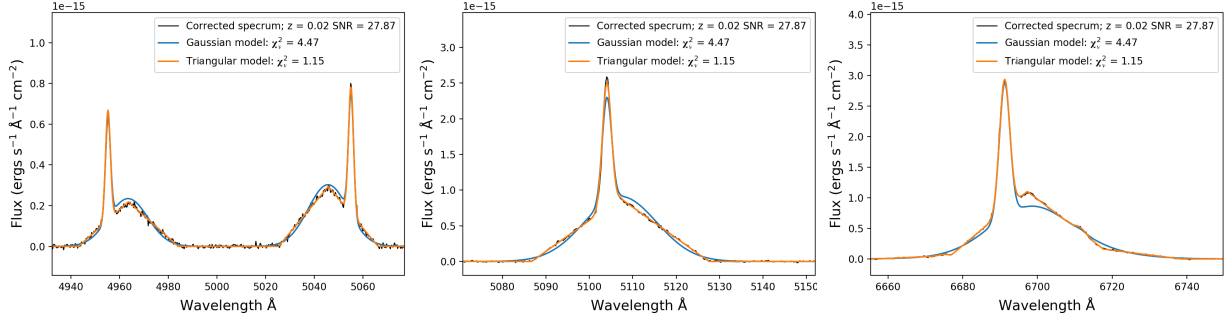
(c) Spectrum: SNR = 27.87, $z = 0.02$. Gaussian model: $\chi_\nu^2 = 4.47$. Triangular model: $\chi_\nu^2 = 1.15$.
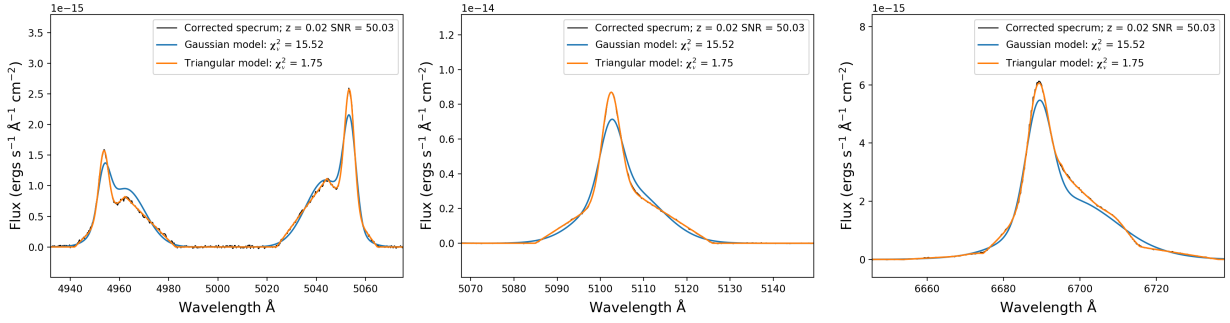
(d) Spectrum: SNR = 50.03, $z = 0.02$. Gaussian model: $\chi_\nu^2 = 15.52$. Triangular model: $\chi_\nu^2 = 1.75$

Figure 44: Four high SNR spectra (black) with line profile fits using the Gaussian model (blue) and the triangular model (orange) for the broad lines. From left to right the plots show the narrow and broad components of the Hβ and OIII-1 lines, the OIII-2 line and the NII-1, Hα and NII-2 emission lines.

(a)

(b)

(c)

(d)
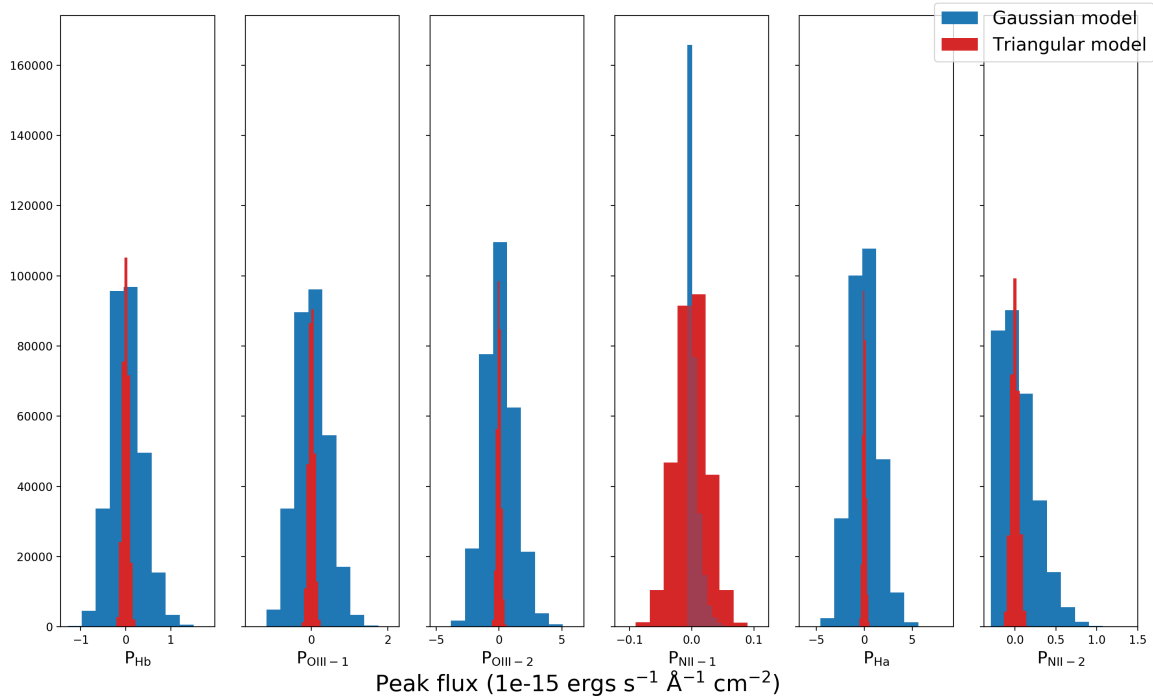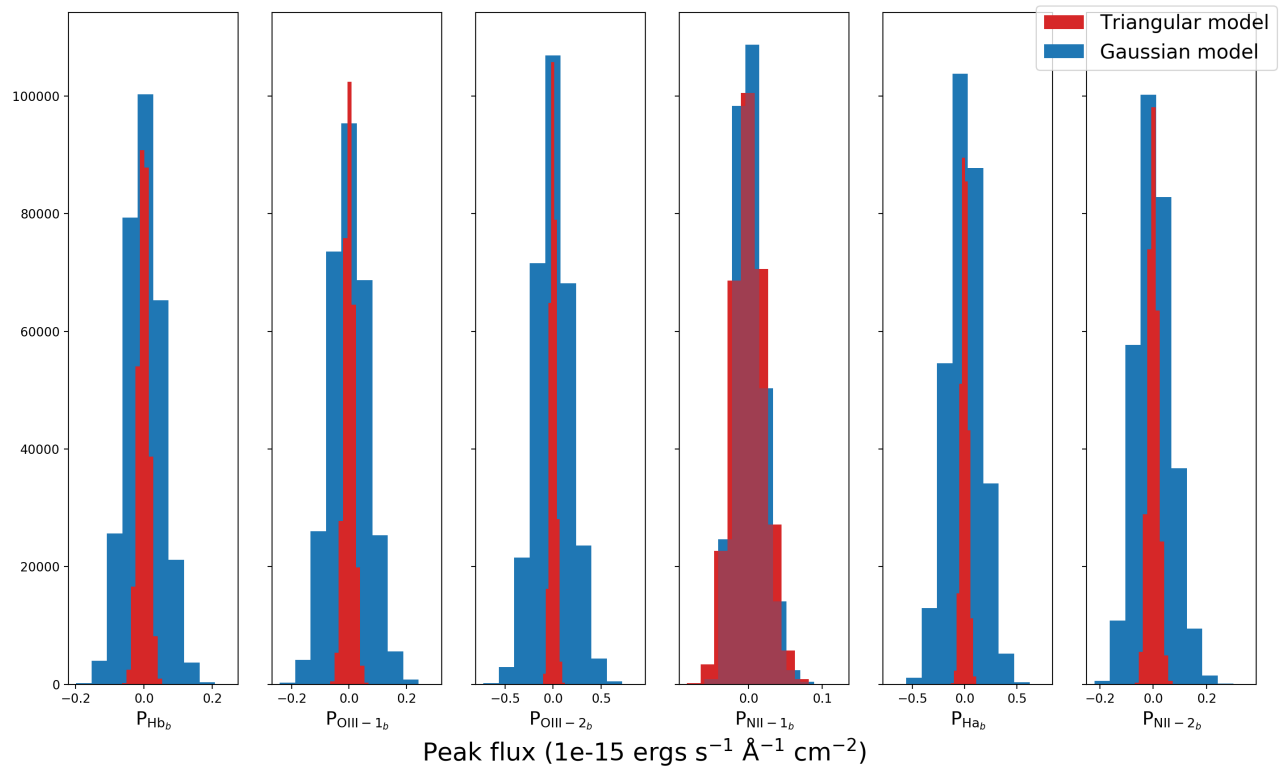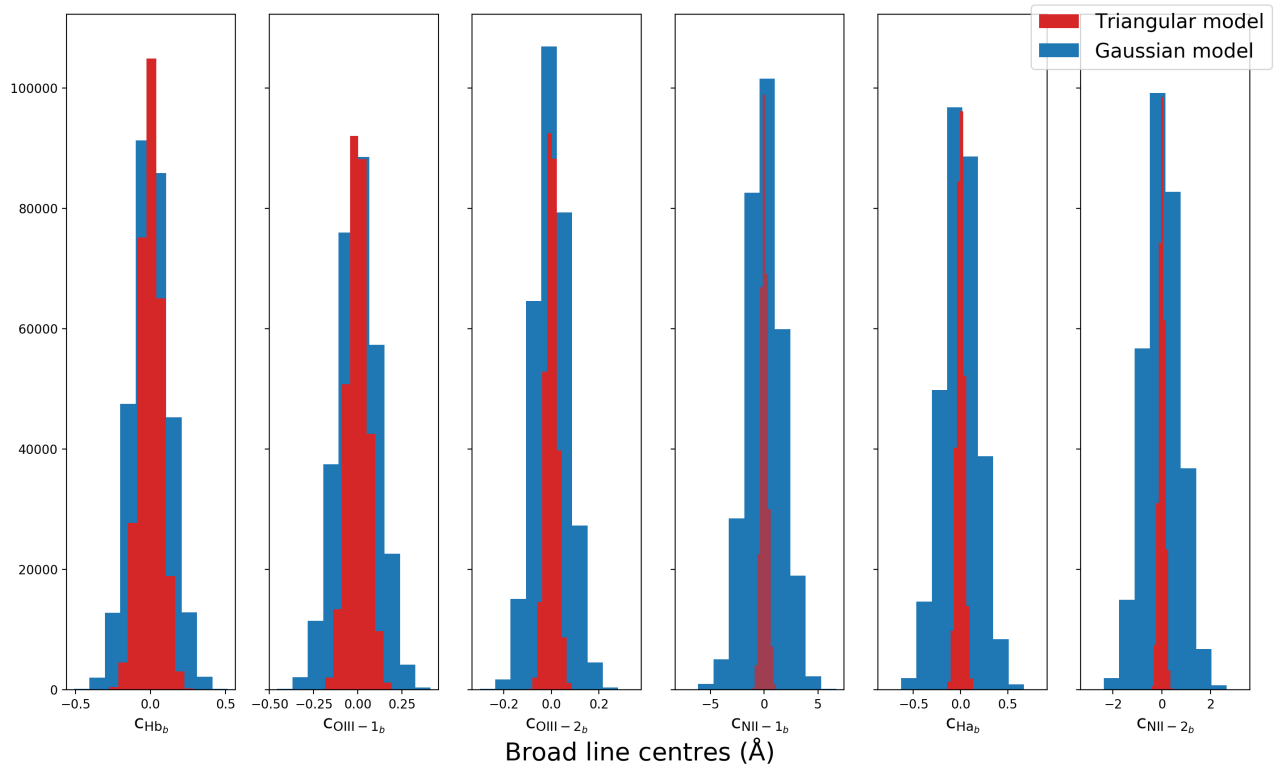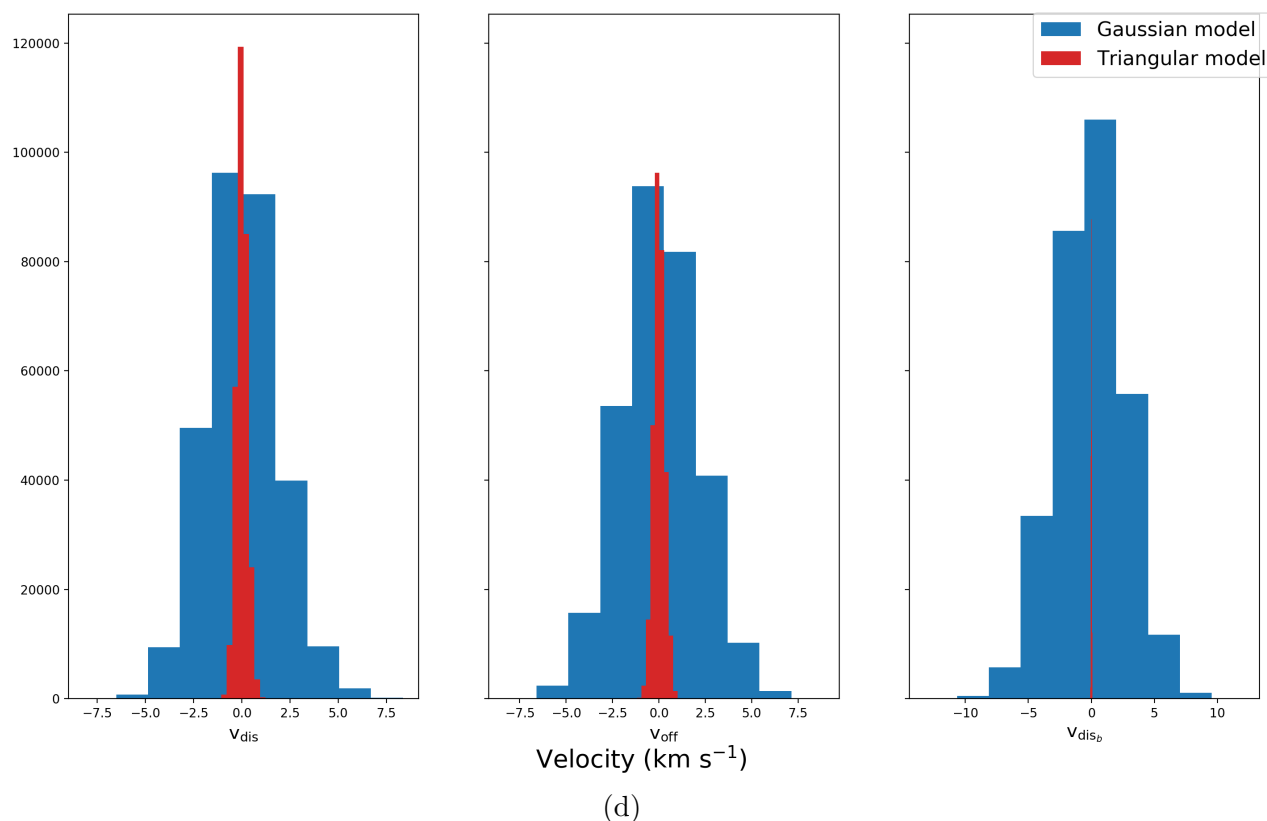
Figure 45: Posterior probability distributions of the main 21 parameters for the spectrum in Fig.44c. The mean posteriors are subtracted from each of the distributions so that the histograms are centred around 0 km s^{-1}. The model which applied a triangle function to the broad structures is represented by the red histograms and the Gaussian function model is represented by the blue. Fig.45a plots the sample distribution of the peak flux parameters for the emission line components, Fig.45b plots the peak fluxes for the broad-structure components, Fig.45c plots the broad line centre estimates and Fig.45d plots the velocity parameters.

(a)   (b)   (c)

(d)   (e)   (f)
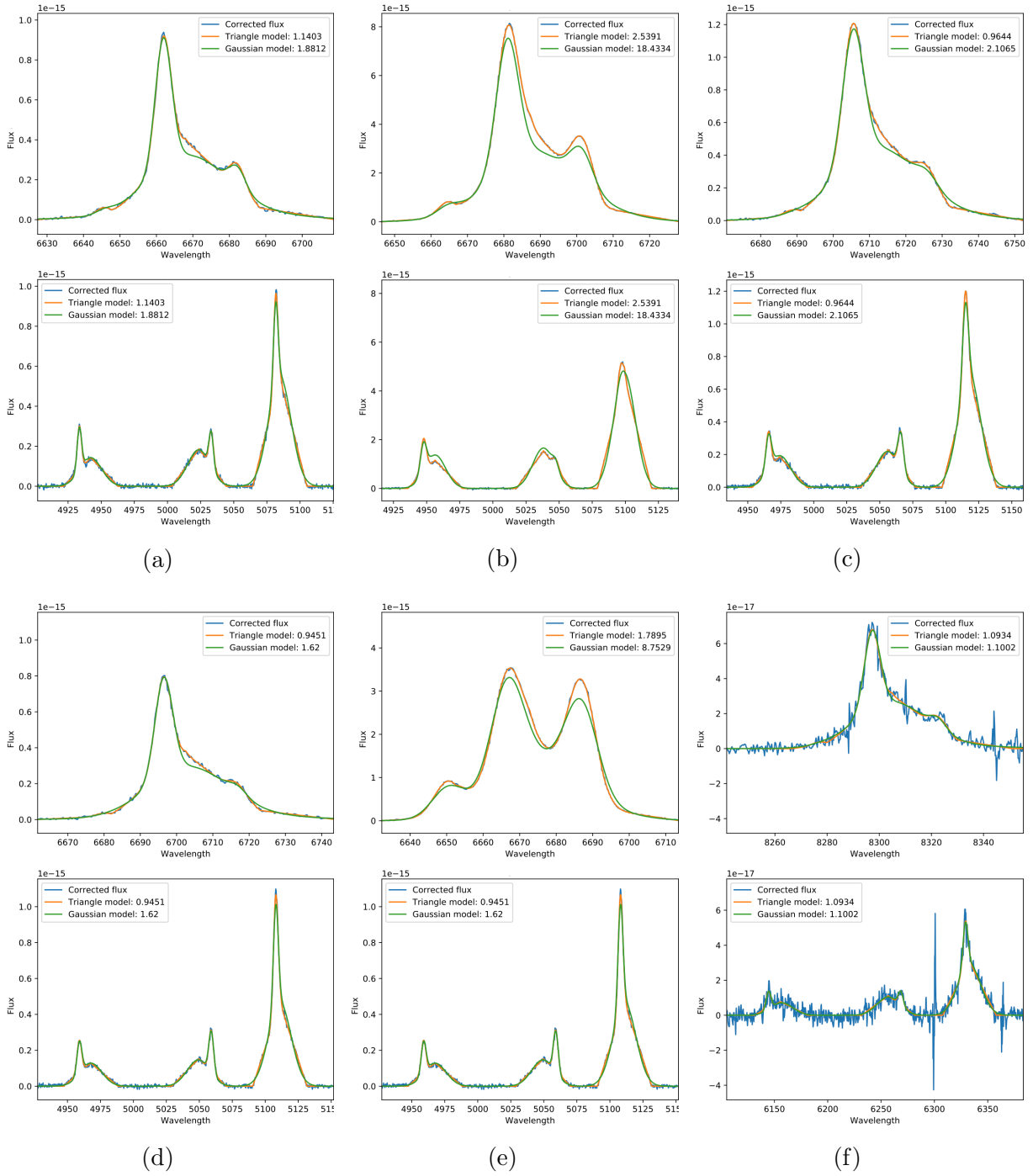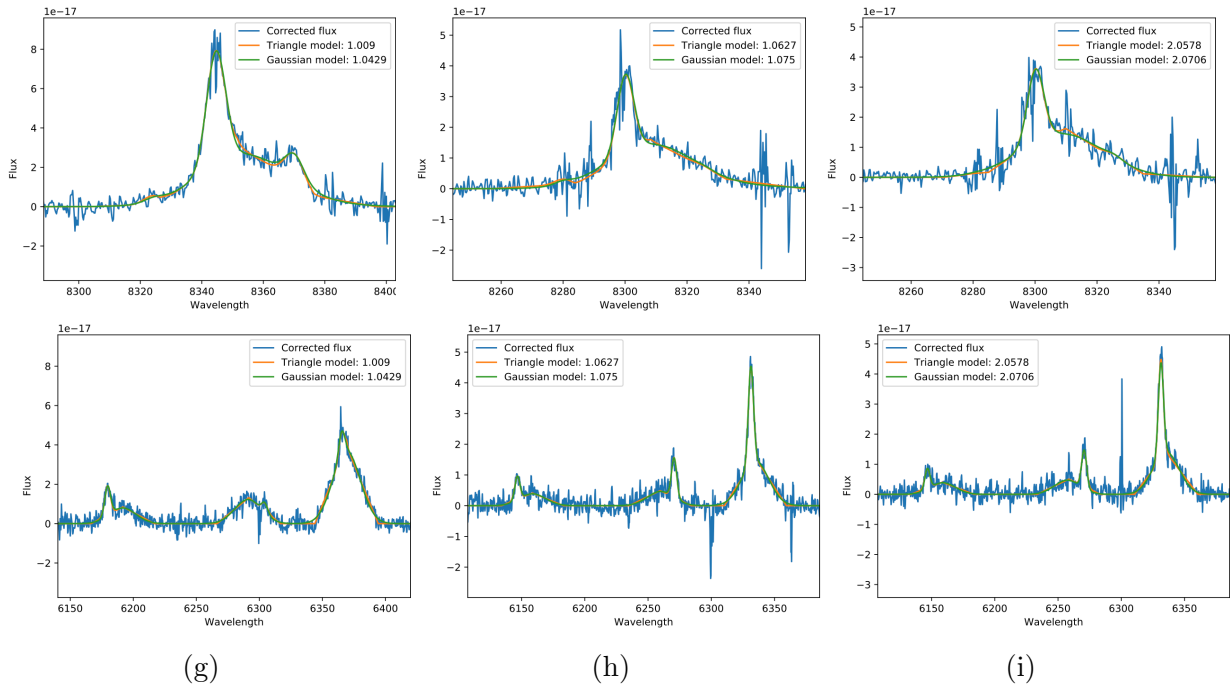
Figure 46: Nine OPR3 spectra (blue) of varying SNRs with line profile fits using the Gaussian model (green) and the triangular model (orange) for the broad lines. Each figure contains the fits around the emission lines in the Hα region (top) and the Hβ region (bottom). The legends in each plot displays the χ^2_ν for both the models.

I again made use of the University of Hertfordshire's high-performance computing facility to fit the emission lines of the 1305 continuum subtracted spectra using the multiprocessing module in Python. Upon investigation of the fits of high redshift spectra ($z > 0.33$), I decided to further filter the sample to exclude fits that have a $\chi^2_\nu > 2$. There are a large number of skylines that litter the longer wavelength range of the optical spectrum and there are a number of incidents where the algorithm has modelled a skyline residual as nebular emission. For example, in Fig.47 a skyline at 9313.7 Å overlaps with the NII-1 emission line and the algorithm has mistakenly modelled it as part of the emission line. The χ^2_ν is also quite low, therefore it is hard to quantitatively identify when this happens. χ^2_ν is low due to low SNR at higher redshifts and the fact the skyline is part of the spectrum used to calculate the χ^2_ν; a χ^2_ν close to 1 informs us that the model has fit the data, however it does not tell us if the emission is contaminated by a skyline. The $\chi^2(\lambda)$ spectrum (green) is displayed in the lower panel in Fig.47 which is strongest around the two skyline residuals. This indicates that, in this case, the spectrum is poorly modelled around the skylines. A requirement of a $\chi^2_\nu < 2$ for any spectrum with $z > 0.33$ avoids filtering out the entire high redshift region of the sample; 102 of the spectra did not meet this requirement and were cut from the sample.
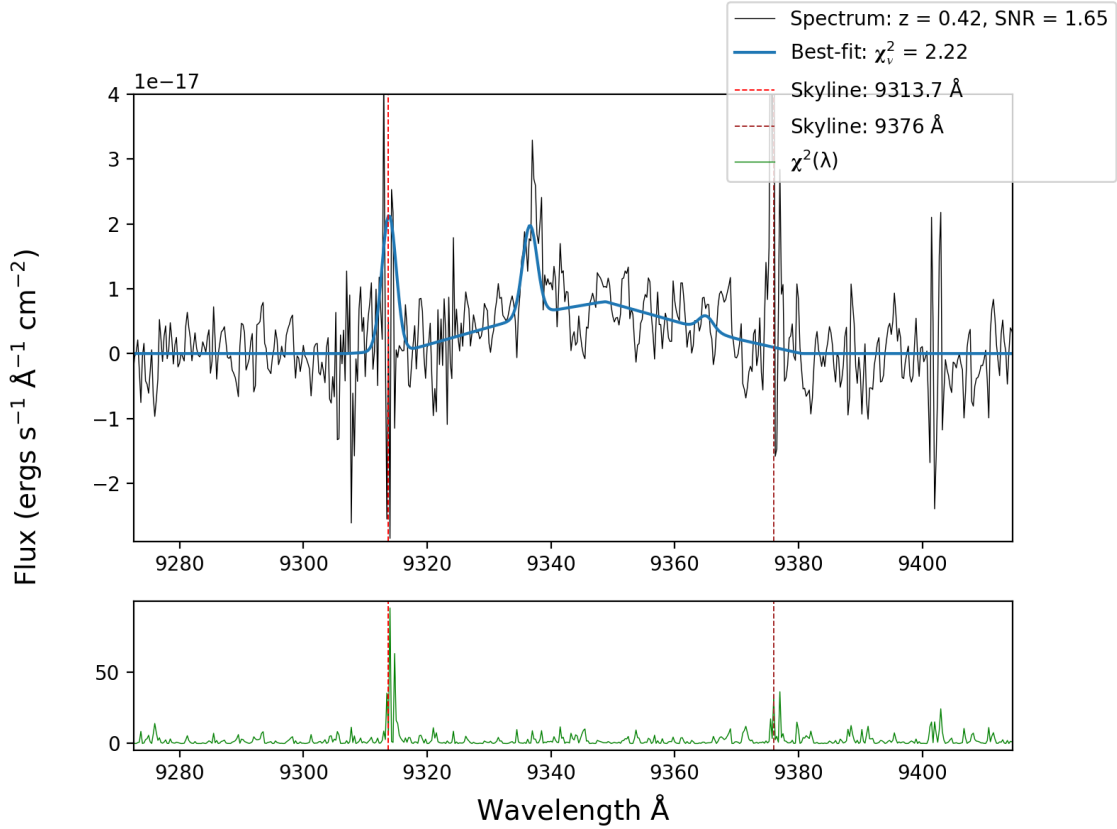
Figure 47: Example of a high redshift spectrum (black) where the skylines interfere with the modelling of the Hα region (blue). Skylines at 9313.7 and 9376 Å are represented by a red and brown dashed line respectively. The skyline at 9313.7 Å was mistakenly modelled as part of the redshifted NII-1 emission line. The $\chi^2(\lambda)$ spectrum (green) is displayed in the lower plot.

The χ^2_ν for the rest of the sample are plotted against their redshifts in Fig.48 with the SNR of the same area overlaid in a colour map. The largest χ^2_ν are either due to a skyline resulting in a significantly underestimated RMS, or the 6300 and 6363 Å OI skylines contaminating the continuum between the emission lines in the Hβ regions. Considering the high dimensionality of the optimisation problem and the complexity of the data (i.e. the flux calibration issue and irregular broad line profiles), the MCMC fitting algorithm has performed outstandingly well with the largest χ^2_ν as low as 3.23. The fits of the Hβ regions for the two largest χ^2_ν are displayed in Fig.49 along with their $\chi^2(\lambda)$ arrays. Both of these spectra contain the 6300 and 6363 Å emission lines which only contaminate the broad lines, hence why they were left in the sample. It is clear that these skylines give rise to a much higher χ^2_ν as the $\chi^2(\lambda)$ array peaks at the emission wavelengths.
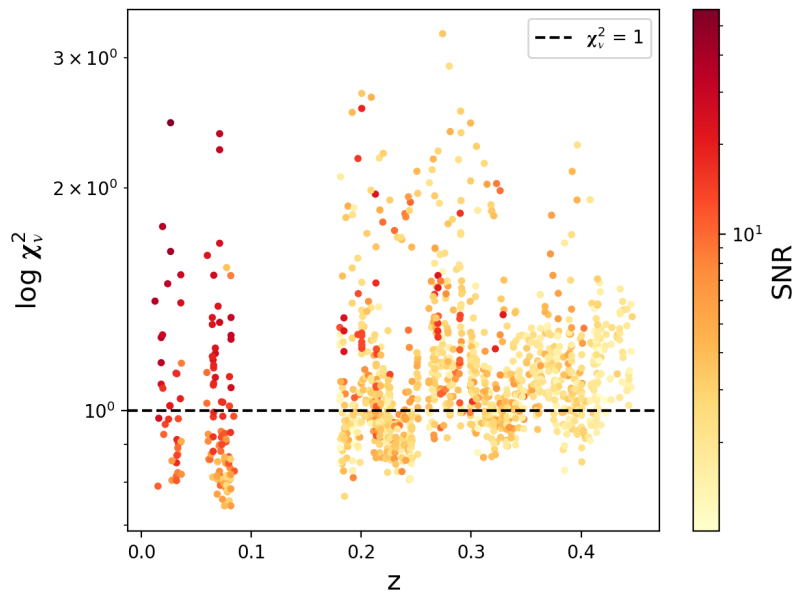
Figure 48: Plot of the redshifts against the log χ^2_ν of the line fitting for a sample of 1305 OPR3 spectra with a logarithmic colour map of the SNR. The wavelength range used to calculate the χ^2_ν and the SNR of the Hα and Hβ excluded the continuum, taking between $\pm 35 \times (1+z)$ Å of data either side of the outer emission lines. The redshift gap between 0.1 and 0.2 is due to the redshifted emission lines falling in range of the blue and red arm CCD chip gaps. The redshift gap at 0.05 is due to the 6865 - 6920 Å skylines crossing the emission lines in the Hα region.
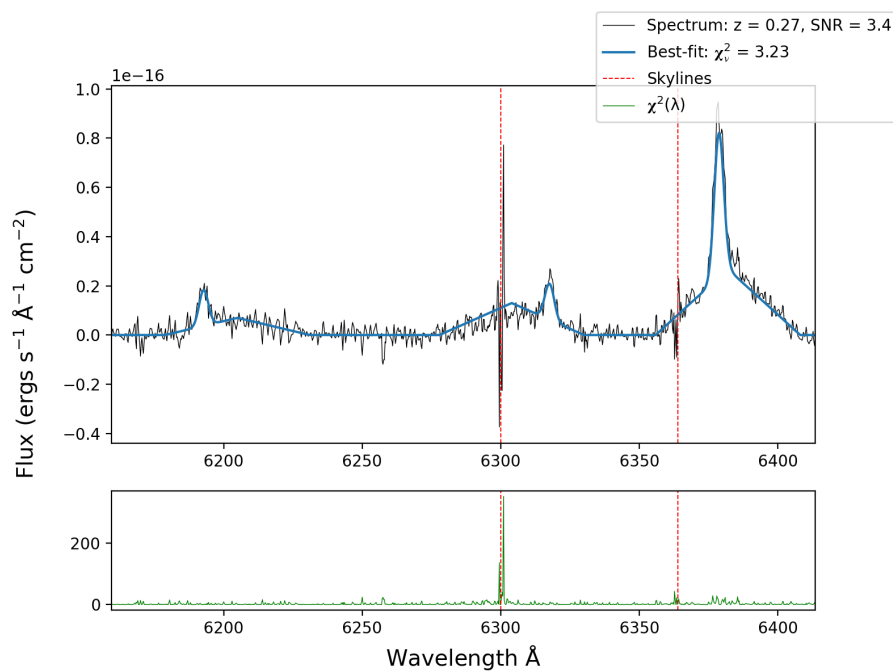
(a) Largest χ^2_ν for the line fitting model.
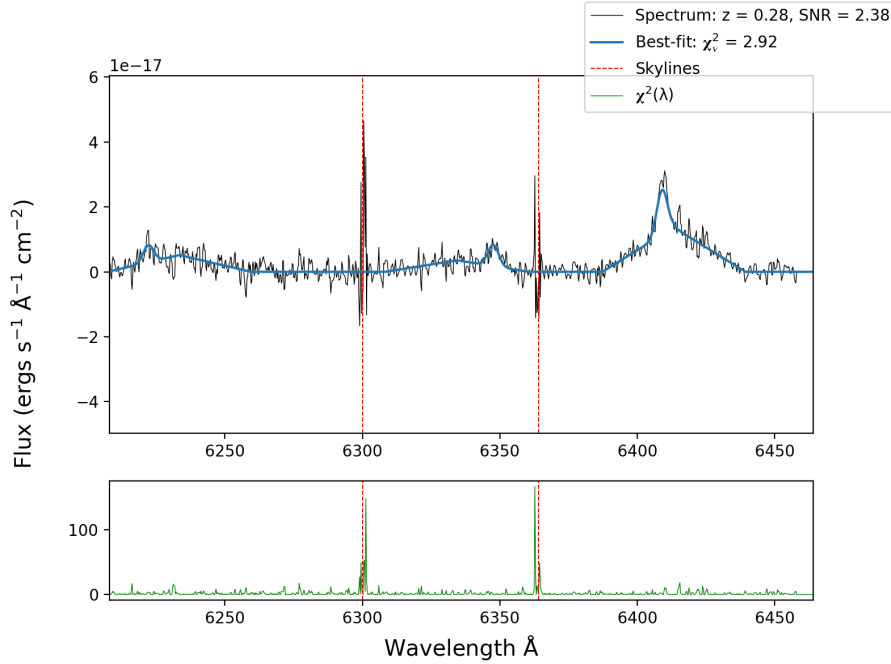
(b) Second largest χ^2_ν for the line fitting model.

Figure 49: Two Hβ region fits which resulted in the largest χ^2_ν of the entire sample. The best-fit (blue) is overlaid on top of the spectra (black) with the two red dashed lines indicating the presence of two skylines (6300 and 6363 Å). The χ^2 array is represented by the green line in the lower plot for each figure. The peaks in this array align with the two skylines which indicated that these structures are causing a larger χ^2_ν for the entire fit.

With the sample complete and sufficient evidence to have confidence in the algorithm, the line fluxes can be calculated. Using the mean posterior estimates for the emission line parameters, the line fluxes are derived by integrating over their Gaussian profiles and the errors are propagated through accordingly. The offset ratio error is also applied to the integrated flux uncertainties for any emission line which fell on the blue spectrum; 216 spectra have redshifts which places the Hβ region within the wavelength range of the blue arm.

8   Input flux comparison results

A total of 9 spectra were further filtered out from the sample as their integrated flux ratios of $F_{H\beta}/F_{H\alpha}$ are lower than the dust free Case B recombination value of 2.86; this is further discussed in section 8.3. 31 spectra containing line flux estimates which were consistent with zero were also removed from the sample. The sample used in the following analysis contains 1163 spectra of which 192 spectra contain emission lines in the Hβ region which fall within the wavelength range of the blue arm; throughout the analysis these will also be investigated separately to the main sample to determine if the flux calibration offset was modelled correctly and whether more work is required before they can be considered reliable

measurements.

Each of the line flux measurements have been corrected for seeing effects. The seeing is a measurement of the sharpness of telescope, it is dependent on the amount of turbulence in the Earth's atmosphere as this sets a limit on the resolution of the telescope and distorts the diffraction limit (Porter et al., 2006). The seeing is quantified in terms of the FWHM of the photon distribution across the fibres: WEAVE's fibres are 1.3" in diameter, therefore a spectrum with a seeing of 1.3" would require a large correction factor. The OPR3 simulation modelled the seeing between 0.4 - 1.2". The correction factor is calculated by first converting the seeing (FWHM) to a standard deviation and dividing the fibre radius (0.65") by this value, as described by Eq.19. The correction multiplicative factor is then calculated using Eq.20 which is directly applied to the integrated flux estimates. The seeing correction assumes a Gaussian profile, however galaxies are not perfectly spherical, and their shapes vary vastly. Hence, the seeing corrections will be dependent on the morphology of the galaxy for the real WEAVE-LOFAR data.

$$R = \frac{0.65 \times 2\sqrt{2\ln(2)}}{\text{FWHM}} \tag{19}$$

$$C = \frac{1}{1 - \exp(-R^2/2)} \tag{20}$$

The point spread function (PSF) of the instrumentation has not been taken into account in my calculations as the seeing dominates the intrinsic PSF. The seeing and the PSF act as two convolving Gaussians, therefore the intrinsic FWHM of the instrumental PSF can be added in quadrature to the seeing. This means that there is slightly more emission scattered out of the fibre than is accounted for by the seeing alone. The intrinsic PSF of the telescope can be determined using the Rayleigh criterion, as described in Eq.21, where θ is the FWHM at a given wavelength (λ) for a telescope with a diameter D. The WHT is a 4.2m telescope, therefore at a wavelength of 6564 Å (the rest frame wavelength of Hα) the FWHM of the PSF is a hundredth of an arcsecond. Since the seeing is completely dominant, I will not be accounting for the instrumental PSF in my analysis.

$$\theta = 1.22\frac{\lambda}{D} \tag{21}$$

8.1   Input line flux comparison

The MCMC flux estimates for the narrow lines are compared with the flux values from the input spectrum in Fig.50. The input spectrum is the total emission before entering the Earth's atmosphere; it includes all the effects of redshifting and dust attenuation. The comparison essentially demonstrates how well the MCMC fitting algorithm can return the input values after experiencing absorption from the atmosphere, seeing effects, instrumental noise and other processes which result in a loss of detected emission photons. The input luminosities for each emission line have been provided and I converted them to fluxes using the distance luminosity relation in Eq.22; where $F(\lambda)$ is flux at a given wavelength range, $L(\lambda)$ is the corresponding luminosity and $D_L(z)$ is the luminosity distance given the known

redshift (z) of the target and assuming a cosmology consistent with a ΛCDM, $H_0 = 70$ km s^{-1} Mpc^{-1}, $\Omega_m = 0.3$ and $\Omega_\Lambda = 0.7$.

$$F(\lambda) = \frac{L(\lambda)}{4\pi \times D_L^2(z)} \tag{22}$$

The integrated fluxes of each of the emission lines required for the BPT diagram are plotted against the known input fluxes in Fig.50; these include Hα, Hβ, OIII-2 λ/5007 Å and NII-2 λ/6584 Å. Alongside the error-bar plots, a logarithmic colour-map using the SNR is also plotted which verifies that the SNR is correctly correlated with the flux of the lines and their errors. Scatter is present which increases as the flux gets weaker, as is true for the errors on the flux. It is evident that the observed flux of all four emission lines form a linear relationship with the known input values. A 1:1 reference line is plotted in blue for each of the comparison plots, which the MCMC estimates all fall short of. Any signal lost between the atmosphere and detection should be taken care of by the flux calibration if this is done correctly, except in the case where the source light profile differs significantly from the calibration source. It is important to quantify how much the MCMC estimates underestimate the input flux in order to ensure that the algorithm is performing as intended and the flux calibration inconsistency has been correctly accounted for and to gauge how well we can recover fluxes using WEAVE. Correction scales (C_s) have been calculated to quantify this underestimation, where C_s = MCMC flux estimated / input flux. The correction scales between the two sets of data for each emission line all fall within 0.73 ± 0.01, each with fractional uncertainties of 10^{-5}. MCMC flux estimates have been corrected for the seeing, the C_s factors all fall within a narrow range and the algorithm and model have been tested and statistically proven to return good fits for the OPR3 spectra. Since there is enough statistical and visual evidence to prove that the MCMC fitting algorithm is performing as intended and outputting reliable and reproducible results, then the C_s factors derived above suggest that there is a systematic offset in the simulation, most likely due to the flux calibration inconsistency.
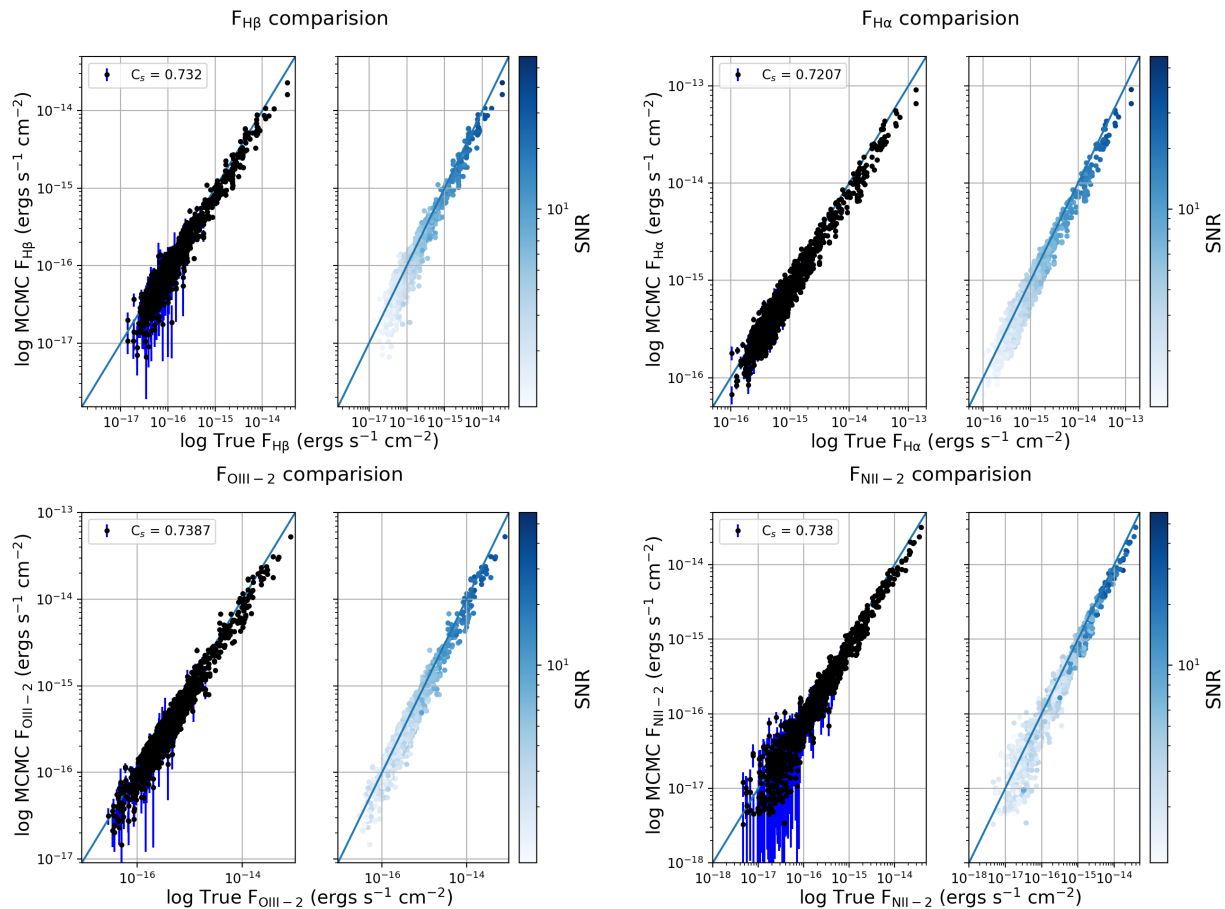
Figure 50: Comparison plots of the true input flux values vs the MCMC estimates for the Hβ, Hα, OIII-2 λ/5007 Å and NII-2 λ/6584 Å emission lines. The left figure in each plot contains an error-bar scatter plot of the MCMC estimates, the 1:1 reference line (blue) and the C_s factors in the legends. The right figure plots a logarithmic SNR colour-map over the fluxes.
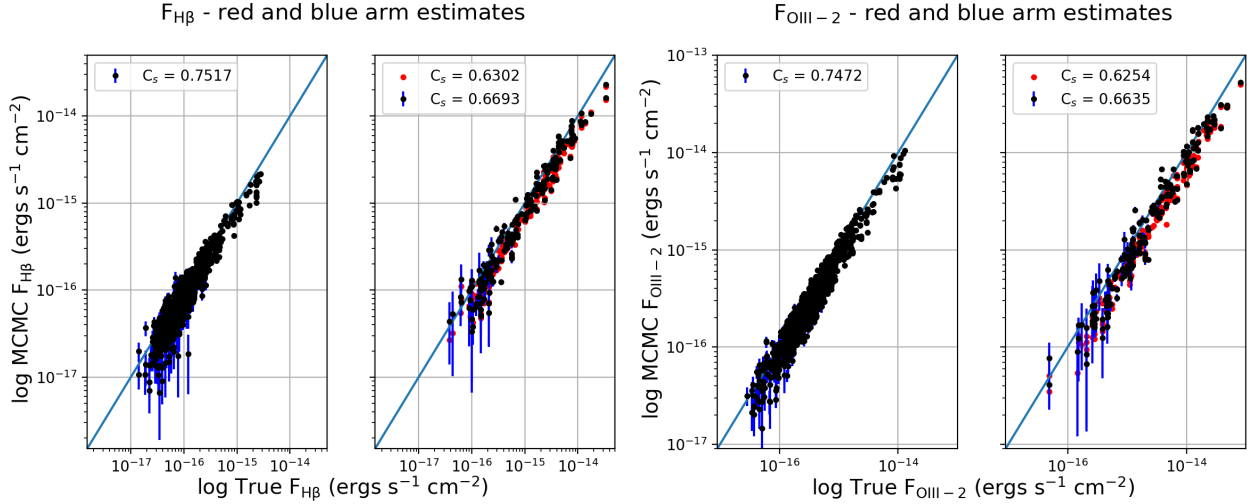
Figure 51: A comparison of the MCMC flux estimates with the known input values for Hβ and OIII-2 are displayed above. Each figure contains two plots: the left contains the measurements using the red arm and the right contains those taken from the blue arm. The C_s factors for each set of data compared to the known input values are displayed with each plot. The red markers in the blue arm plots indicate the MCMC derived flux estimates prior to the applying the normalisation ratios (offset correction); the C_s factor of this set of data is also displayed, where C_s = uncorrected MCMC fluxes/input fluxes = 0.6254.

The blue and red arm flux estimates for the Hβ and OIII-2 emission lines are displayed separately in Fig.51. The relevance of this comparison is to analyse whether the flux calibration inconsistency has been correctly accounted for. Any line measured by the blue arm has been scaled by the normalisation ratio of the two arms (N_b/N_r) and any measurements from the red arm are assumed to be unaffected by the flux calibration issue. It is difficult to identify problems with the flux calibration by comparing the measurements from each arm as the conditions are very different; the blue arm detects low-redshift, high-SNR targets and the red arm detects high-redshift, low-SNR targets. Furthermore, there are far more measurements taken in the red arm compared to the blue: 971 spectra have observed emission lines in the wavelength range of the red arm and 192 within that of the blue arm. Therefore any conclusions drawn from this comparison would require more blue arm measurements as evidence. The C_s factors indicate that the red arm estimates are $\sim 8\%$ more in agreement with the known input values (i.e. difference in the C_s factors). The blue arm flux measurements prior to applying the normalisation ratio (red points in Fig.51) are $\sim 3\%$ less in agreement with the data than those with the offset correction applied. This is encouraging as it indicates that the calibration correction is improving the results in comparison to the input fluxes. Combining the uncorrected values with the red arm estimates changes the C_s factor of the OIII-2 emission lines from 0.7387 to 0.7348 and the Hα emission lines factor from 0.7320 to 0.7227. The calibration offset essentially has a negligible effect on the scaling difference between the MCMC estimates and the input values. In conclusion, I am unable to verify whether the calibration offset solely affects the blue arm, the red arm or both. This could be further directly addressed in future work by using both arms to fit the data where the Hβ region falls within the overlap of the blue and red spectra.

Fig.52 presents a colour-map plot of the posterior mean A_v estimates using the MCMC fitting algorithm for the continuum in comparison to the input A_v values. The discrete colour-map indicates which template number was used for the optimal fit of the continuum. There is a strong correlation between the chosen BC03 template and the factor by which the MCMC estimates of A_v are over or underestimated. The lower the given template number the bluer it is; therefore, the MCMC/input factor for A_v also appears to correlate with the blueness of the template. Both these relationships indicate that the flux calibration inconsistency is resulting in bluer continua, which ultimately means the MCMC algorithm is unable to return correct values of A_v. Consequently, the normalisation parameter estimates, which model the calibration offset in an attempt to correct it, are most likely also incorrect since they both strongly correlate with A_v since all three parameters model the shape of the continuum. However, it is very positive that I find for a given template the gradient appears close to a 1:1 relationship.
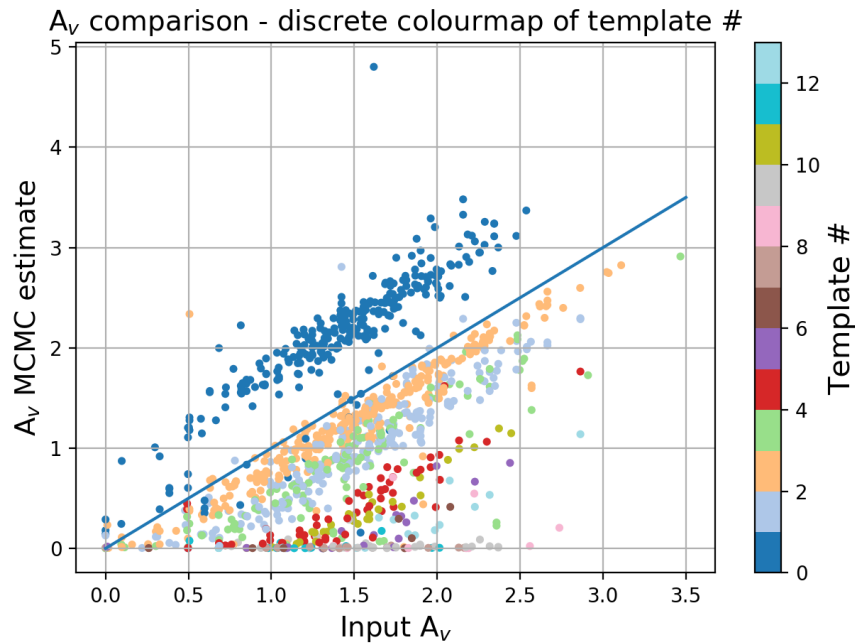
Figure 52: Comparison of the A_v MCMC estimates and the input values with a discrete colour-map of the template number overlaid. The template numbers correspond to the following BC03 templates: 0: 'ssp: 5 Myr', 1: 'ssp: 25 Myr', 2: 'ssp: 100 Myr', 3: 'ssp: 290 Myr', 4: 'cst: 6 Gyr', 5: 'ssp: 640 Myr', 6: 't9e9: 12 Gyr', 7: 'ssp: 900 Myr', 8: 't5e9: 12 Gyr', 9: 'ssp: 1.4 Gyr', 10: 'ssp: 2.5 Gyr', 11: 'ssp: 5 Gyr', and 12: 'ssp: 11 Gyr'.

Fig.53 displays the luminosity comparison plots between the MCMC estimates and the input luminosities. The MCMC fluxes are converted to luminosities using their target's known redshifts in the distance luminosity relation in Eq.22. The relationship between the two sets of data is as expected in Fig.53: there is a strong linear relation and the uncertainties are larger for weaker luminosities. This plot is very encouraging for WEAVE as it indicates that we are recovering all the basic relationships that we would expect.
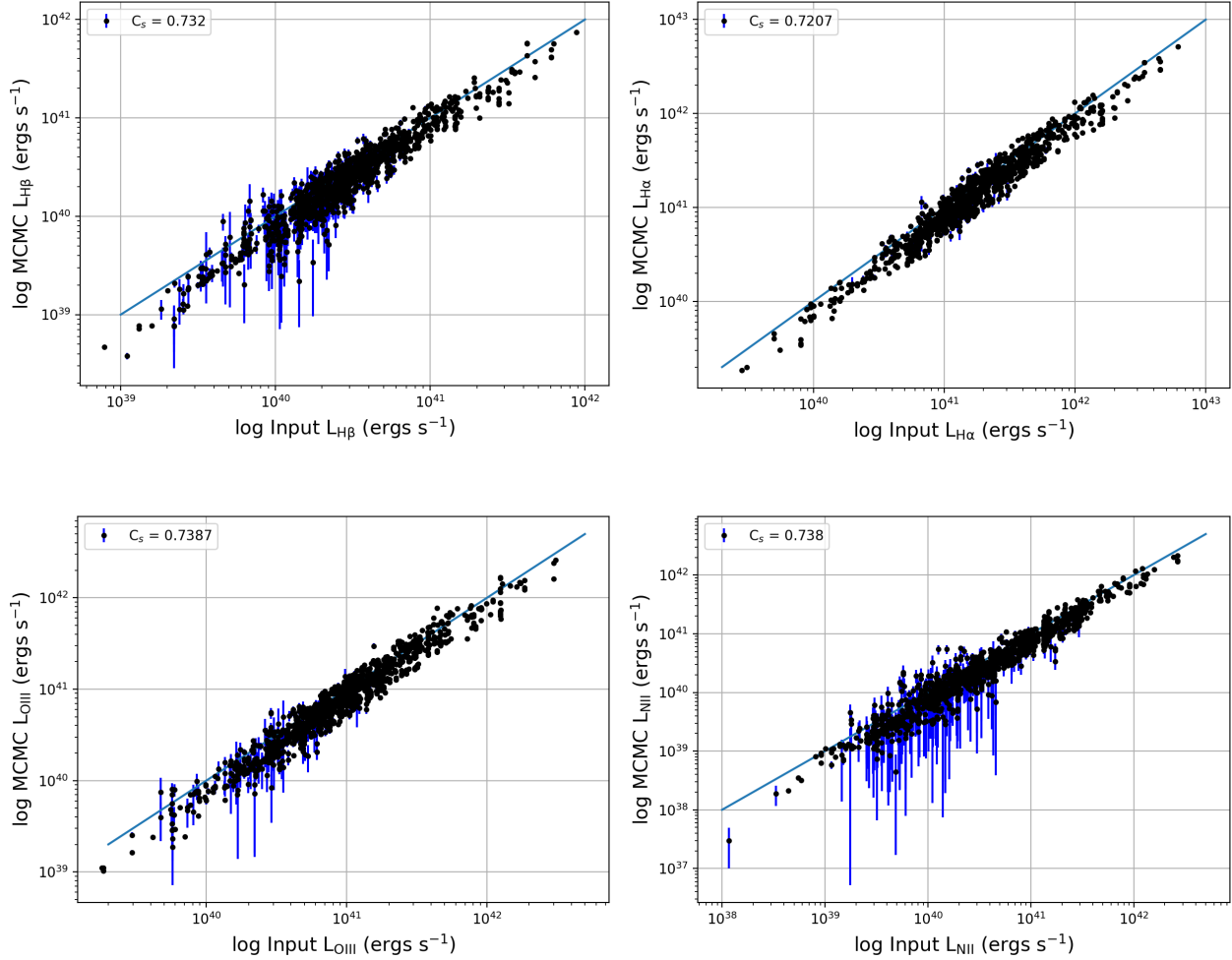
Figure 53: Comparison plots of the input luminosities (ergs s^{-1}) with those derived from the MCMC flux estimates for Hβ, Hα, OIII-2 and NII-2.

8.2   BPT-NII comparison

The BPT diagram uses flux ratios for lines which are close in wavelength. This means the ratios are independent of reddening effects and any potential systematic offset since the C$_s$ factors are all consistent with each other and so should not exert significant influence in the ratios. The BPT-NII comparison plot of the MCMC estimates against the known input line ratios is shown in Fig.54, along with logarithmic colour-maps of the SNR and of the errors in log F$_{[OIII]}$/F$_{H\beta}$ and log F$_{[NII]}$/F$_{H\alpha}$. The MCMC algorithm has managed to correctly classify 89% of the targets into star-forming or AGN galaxies based on the Kauffmann et al. (2003) demarcation curve (blue dashed line); 2.5% were incorrectly classified as star-forming galaxies and 8.5% were incorrectly classified as AGN.
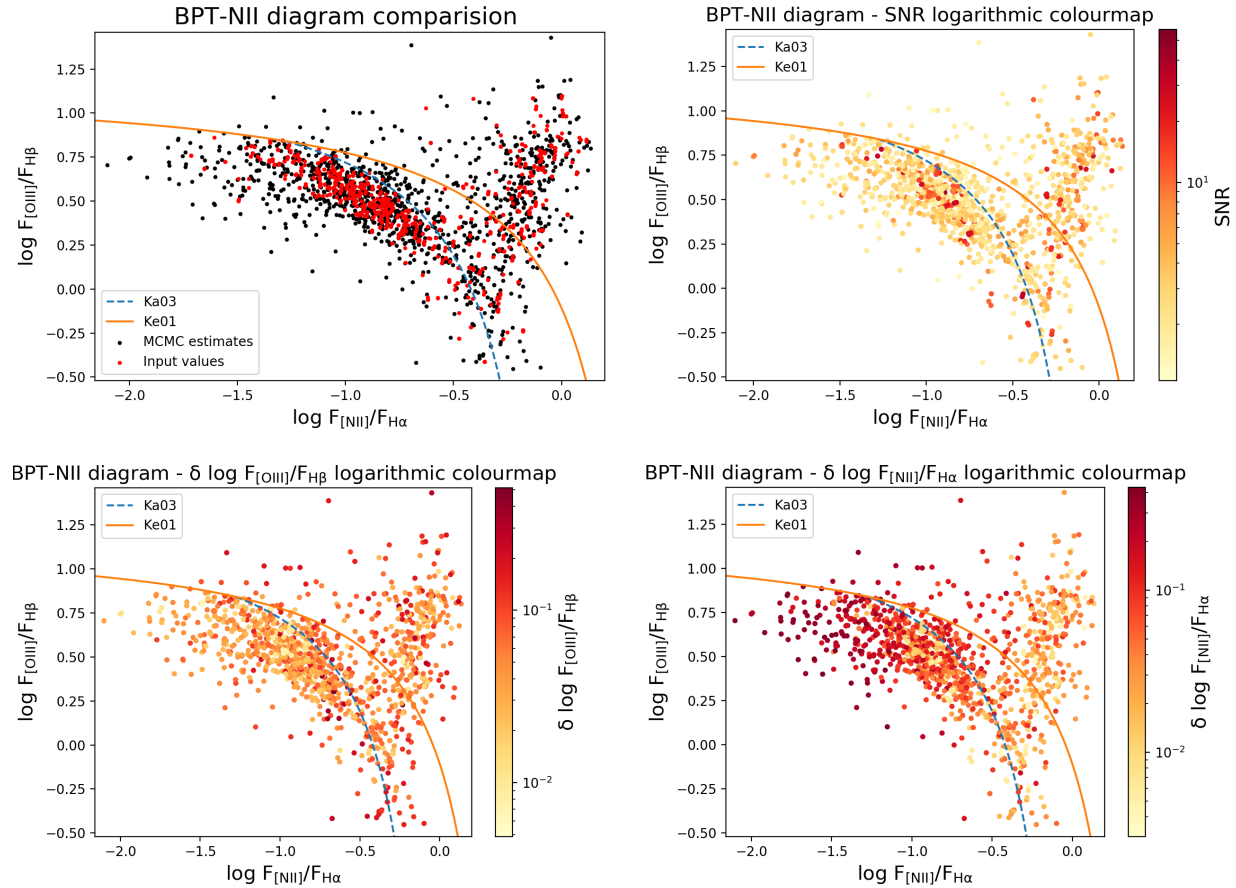
Figure 54: Four BPT-NII diagrams of the line flux ratios estimated using the MCMC algorithm. Each plot contains two hyperbolic curves; the orange Ke01 line is described by Eq.1 and the blue dashed Ka03 line is described by Eq.2. The upper left plot compares the MCMC estimated flux ratios (black markers) with the known input ratios of the emission lines (red markers). The upper right diagram plots a logarithmic colour-map of the SNR for the targets spectrum over the MCMC estimates. Two more logarithmic colour-maps are plotted in the lower two diagrams for the errors in $\log F_{[OIII]}/F_{H\beta}$ and $\log F_{[NII]}/F_{H\alpha}$ respectively.

The MCMC estimates in the BPT-NII comparison diagram in Fig.54 follow the general trend of the input values with considerable scatter. This scatter is mostly the result of low SNR spectra making it more unlikely to return the input flux ratios. As can be seen in the SNR colour-map of the BPT-NII diagram, the scattered regions correspond with the lowest SNR targets, and the central region, where the input values are located, contain much stronger SNR targets. The bottom two colour-maps of the $\log F_{[OIII]}/F_{H\beta}$ and $\log F_{[NII]}/F_{H\alpha}$ errors reflect the low SNR in the scattered regions. The $\delta \log F_{[OIII]}/F_{H\beta}$ values along the y-axis in the bottom left plot become slightly larger in the outer region of the BPT-NII diagram. A much stronger case can be made with the $\delta \log F_{[OIII]}/F_{H\beta}$, which also reflects the impact of poorly estimated NII-2 and $H\alpha$ values due to low SNR and the presence of the blended broad $H\alpha$ line. Fig.55 expands on the BPT-NII diagram. The two error bar

plots compare the log $F_{[OIII]}/F_{H\beta}$ and log $F_{[NII]}/F_{H\alpha}$ ratios with the input ratios and the logarithmic colour-maps plot the flux of each ratio component. Both of the plots have a C_s factor of 0.99, which means that the ratios of the MCMC estimates are in strong agreement with the input values. This further indicates that the fitting algorithm has performed very well, and that the explanation of the flux calibration issue is plausible. The scatter in each plot appears to correlate with the signal strength of the weakest emission line in each of the ratios. The scatter in $F_{[NII]}/F_{H\alpha}$ is dominated by the SNR in the NII line, since the NII line is always weaker than $H\alpha$ in the sample. On the other hand, the $F_{[OIII]}/F_{H\beta}$ lines are more varied in their relative strengths, which means that it varies which of the two species' measurements dominates the error budget and therefore the scatter about the input values.
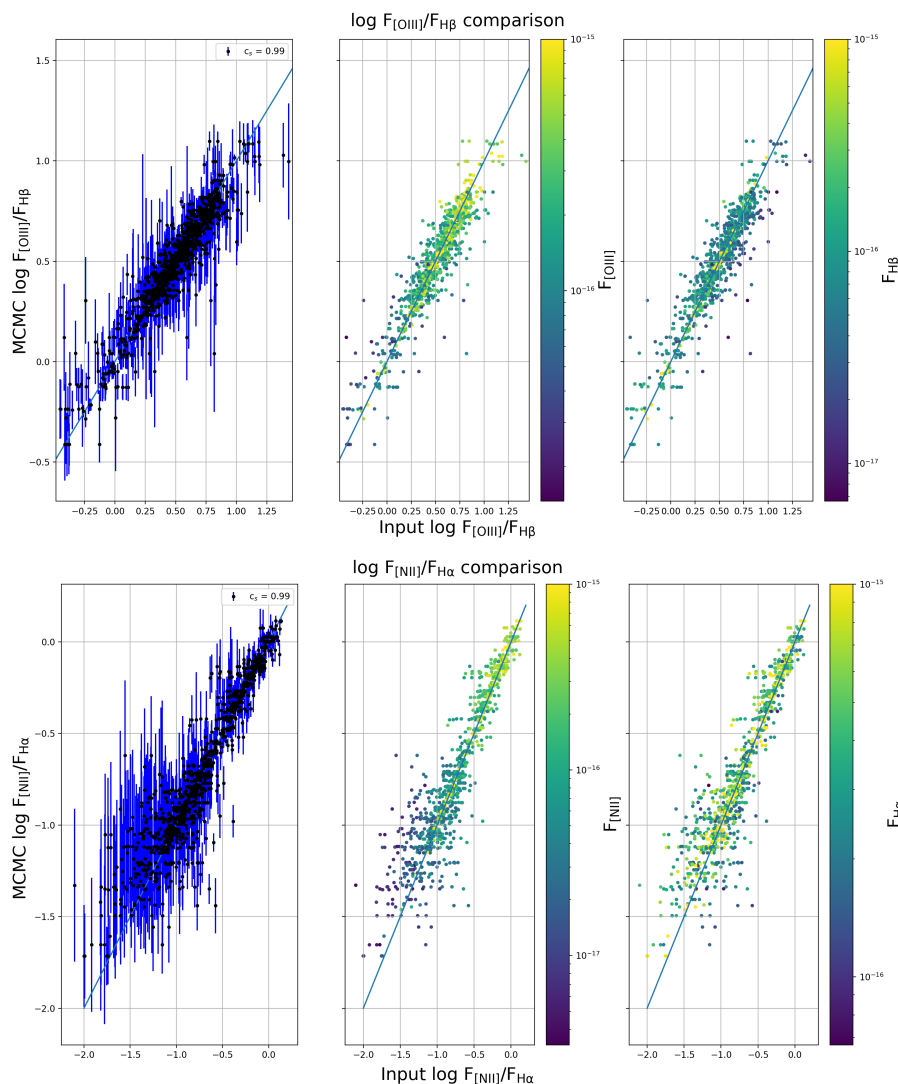
Figure 55: The two figures compare the log $F_{[OIII]}/F_{H\beta}$ and log $F_{[NII]}/F_{H\alpha}$ ratios with their input ratios. The first plot in each figure displays the error-bars and the C_s factor. The two colour-maps overlay the fluxes for each of the emission lines in the ratio. A blue 1:1 reference line is plotted in all the figures.

(a) SNR = 2.477, $\chi_\nu^2 = 1.197$

(b) SNR = 5.523, $\chi_\nu^2 = 1.369$

(c) SNR = 6.552, $\chi_\nu^2 = 1.629$

(d) SNR = 2.334, $\chi_\nu^2 = 1.392$

(e) SNR = 1.363, $\chi_\nu^2 = 1.136$

(f) SNR = 2.679, $\chi_\nu^2 = 0.911$
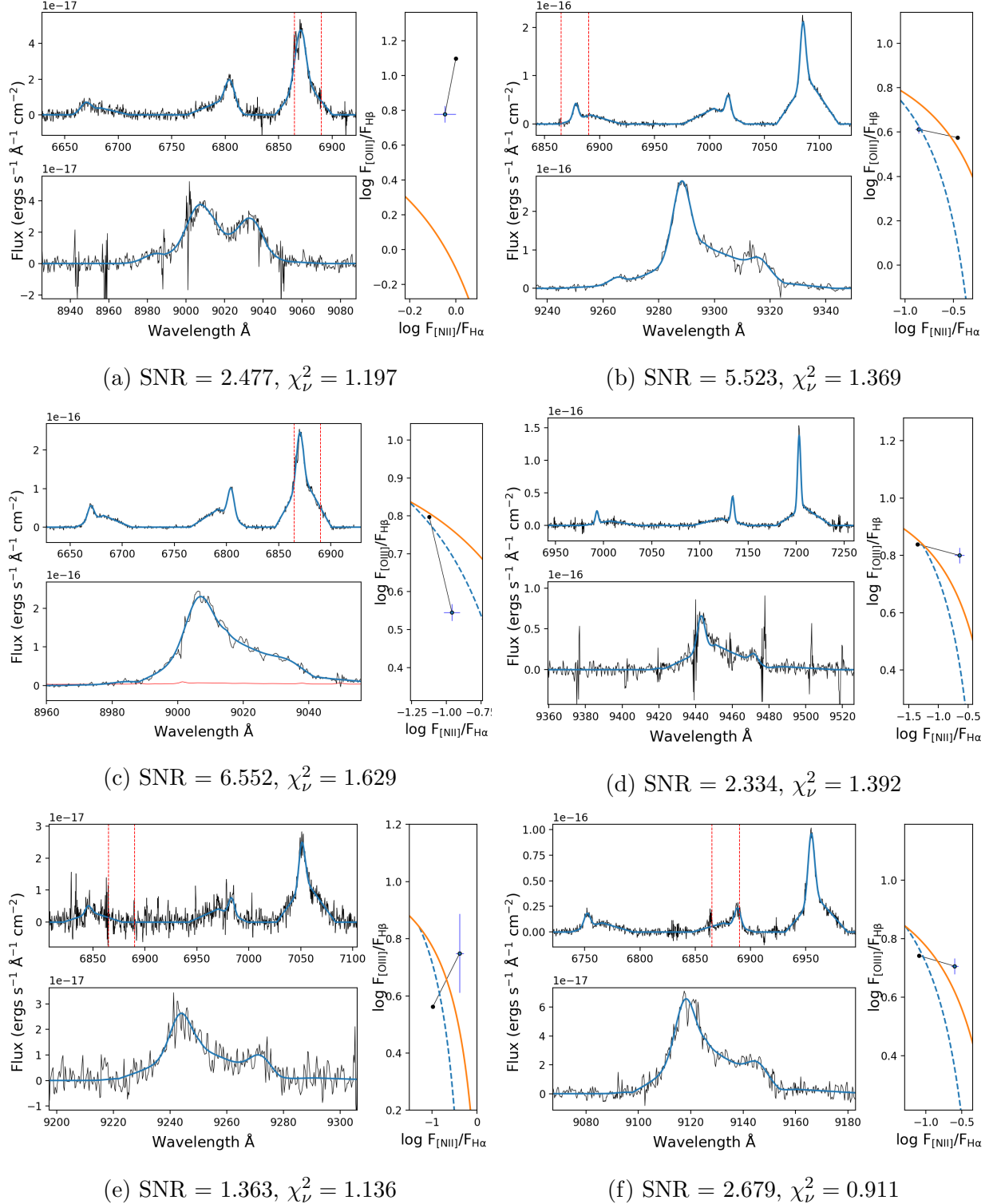
Figure 56: Plots of the Hα, Hβ regions and BPT-NII diagram for the six poorest ratio estimates. These are defined by any input ratio which does not fall within 6σ of either MCMC ratio estimate. The 6865 - 6890 Å skylines are represented by the red dashed lines wherever one of the regions is within range of them.

The most poorly estimated BPT-NII values, where the input ratio does not fall within 6σ of the MCMC estimate in either axis, are presented in Fig.56. The reason for such poor estimates is perhaps due to the presence of skylines causing absorption in the emission lines or their residuals creating structures unaccounted for by the noise (i.e. underestimated RMS of the spectrum). The poor $F_{[OIII]}/F_{H\beta}$ estimates in Fig.56a and 56c are due to an underestimation of the OIII-2 emission line flux due to aligning with the 6865 - 6890 Å skylines. This flux reduction is not fully accounted for in the RMS spectrum, therefore the MCMC algorithm fits the remaining emission and underestimates the parameters uncertainty. Fig.56b, d, e and f plot poorly estimated $F_{[NII]}/F_{H\alpha}$ fits. It is expected that the fit of the broad $H\alpha$ line in the latter figures are modelling a significant amount of the flux in the narrow $H\alpha$ component, resulting in a larger ratio. The lines are blended which makes it difficult to gauge the flux contribution from each of the six lines in this region. However, considering the poor estimation of the input ratio and the fact the fit has modelled the majority of the flux in these two spectra as the broad $H\alpha$ line, it strongly suggests in these two low SNR cases that the algorithm has failed to overcome the extreme blending. The poor estimate of the line fluxes in Fig.56d is a result of skyline residual contamination within the $H\alpha$ region at the high wavelength end of the spectrum which is not accounted for by the RMS array. As previously discussed, if the skylines are not correctly subtracted from the spectrum then it can interfere with the modelling of the emission lines and results in an underestimation of the flux uncertainties. The $F_{[NII]}/F_{H\alpha}$ ratio is offset in the opposite direction in Fig.56b, it appears as though the NII-2 emission line has aligned with an unidentified skyline, resulting in an underestimation of its flux which is unaccounted for in its uncertainty. In conclusion, it appears as though the skylines have a considerable impact on the emission lines if they come into conflict, therefore these must be properly corrected for in the spectrum or correctly accounted for in the RMS. This underlines the importance of the sky subtraction algorithm and the fact that it is essential the uncertainties in this process are to be propagated correctly through to the final WEAVE data products.

8.3 Dust Correction - Balmer decrement

The Balmer emission lines have been extensively studied in astronomy as they have a strong signal and show up almost everywhere since they arise from the recombination of the $n = 2$ level of hydrogen, the most abundant element in the Universe (Dopita et al. 2006; Groves et al. 2012). The two strongest Balmer lines, $H\alpha$ and $H\beta$, are often used to measure the reddening of a galaxy; Berman (1936) was one of the first to relate these lines to dust attenuation. This is possible if the radiation field ionising the hydrogen gas is known, and the relative fluxes of the resulting hydrogen emission lines are only weakly dependent on the local conditions (Groves et al., 2012). For the OPR3 simulation I will assume Case B environmental conditions, $T = 10^4 K$ and $n_e = 10^2 cm^{-3}$ (Dopita et al., 2006), where a nebula is optically thick to all Lyman lines with wavelengths shorter than $Ly\alpha$, which means that a majority of these photons are absorbed and re-emitted by HII regions as Balmer lines.

The intrinsic fluxes of the emission lines were derived following the empirical extinction relation in Eq.23, derived by Calzetti et al. (1994), and using the reddening curve $K(\lambda)$ from Eq.7, derived by Calzetti et al. (2000).

$$A(\lambda) = K(\lambda) \times E(B - V)$$
$$F_{int}(\lambda) = F_{obs}(\lambda) \times 10^{\frac{A(\lambda)}{2.5}}$$

(23)

$A(\lambda)$ is the extinction in magnitudes experienced at a given wavelength. This is required to calculate the intrinsic fluxes, $F_{int}(\lambda)$, in Eq.23 and it can be derived for both the Hα and Hβ lines using the Calzetti reddening curve and $E(B - V)$. The colour excess, $E(B - V)$, is the change in colour between the B and V bands due to dust attenuation. The relationship between the nebular emission line colour excess and the Balmer lines is given using Eq.24.

$$E(B - V) = \frac{E(\beta - \alpha)}{K(\beta) - K(\alpha)}$$

(24)

$K(\beta)$ and $K(\alpha)$ are the values of the Calzetti reddening curve at the Hβ and Hα emission wavelengths. The factor $E(\beta - \alpha)$ is analogous to the colour excess, but defined for Hβ and Hα instead of the B and V bands. $E(\beta - \alpha)$ is derived in Eq.25 using the difference between $A(H\beta)$ and $A(H\alpha)$ and the known Case B intrinsic flux ratio of 2.86.

$$A(\lambda) = -2.5 \times \log\left(\frac{F_{obs}(\lambda)}{F_{int}(\lambda)}\right)$$
$$E(\beta - \alpha) = A(H\beta) - A(H\alpha) = 2.5 \times \log\left(\frac{F(H\alpha)_{em}}{2.86 \times F(H\beta)_{em}}\right)$$

(25)

As mentioned, there were 9 observed flux ratios which were lower than the Case B recombination ratio of 2.86. These cannot be Balmer corrected as the process would result in a negative $E(B - V)$, which is nonphysical. A prior on this recombination ratio should be set on the emission parameters in the MCMC line fitting algorithm. Upon analysis, the 9 spectra were subject to either a poor template fit, conflict with skylines or noisy spectra. Since there were an insignificant quantity of spectra with low Balmer ratios, I decided to remove them from the sample. However, sources with low ratios in the real WEAVE spectra should be treated as consistent with no extinction and included in the sample.

Fig.57 compares the intrinsic estimates, dust corrected using the Balmer decrement, with the dust attenuated observed emission line fluxes for both Hα and Hβ. The histograms show that the dust correction has worked as intended, as none of the corrected fluxes are weaker than the observed fluxes. Fig.58 shows the same plots for the known input fluxes and their histograms follow a similar profile to that of the MCMC estimates. A comparison of the $A(H\alpha)$ attenuation of the MCMC and input estimates is shown in Fig.59a. The two distributions are in close agreement (C_s = input/MCMC = 0.96) with each other, which is encouraging considering that some of the MCMC Hβ fluxes have been calibration offset corrected; although only for a small fraction of the sample, therefore these data may have an insignificant influence. Fig.59b plots the true simulated A_v against the derived input $A(H\alpha)$ using the Balmer decrement. The derived $A(H\alpha)$ values overestimate the true attenuation by 34%, with a considerable amount of scatter. This is most likely because the Balmer decrement measures the extinction in the two Balmer lines which experiences a different level of attenuation from the continuum.
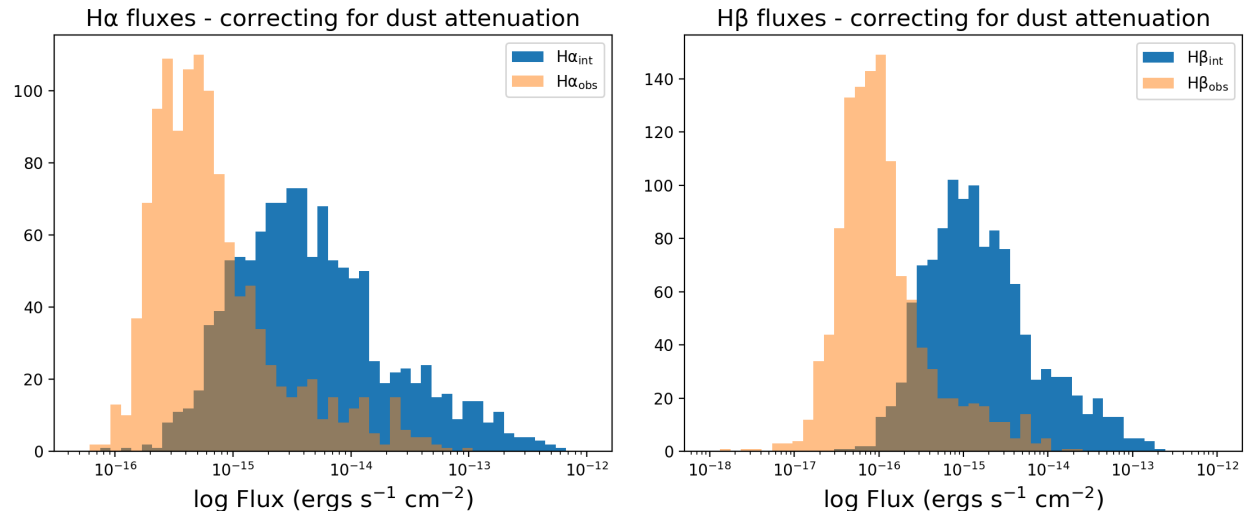
Figure 57: Histograms for the observed extinction-corrected flux in Hα (left) and Hβ (right). Both plots compare the observed fluxes (orange) of the emission lines in the OPR3 sample with the intrinsic estimates (blue) after correcting for dust attenuation using the Balmer decrement.
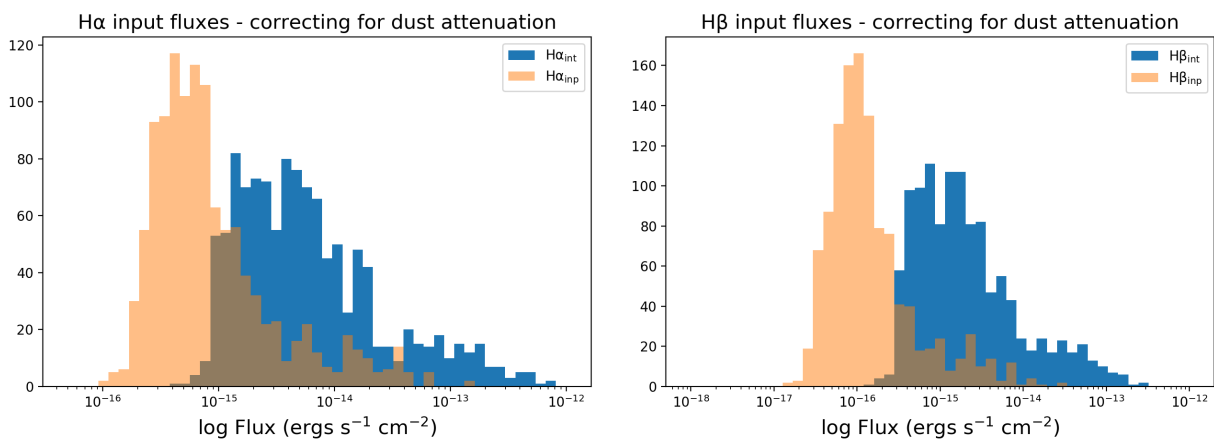
Figure 58: Histograms for the extinction-corrected input flux in the Hα (left) and Hβ (right) emission lines. Both plots compare the attenuated input fluxes (orange) of the OPR3 sample with the intrinsic estimates (blue) after correcting for dust attenuation using the Balmer decrement.

(a) Input A(Hα) vs the MCMC A(Hα)

(b) True A_v vs the input A(Hα)
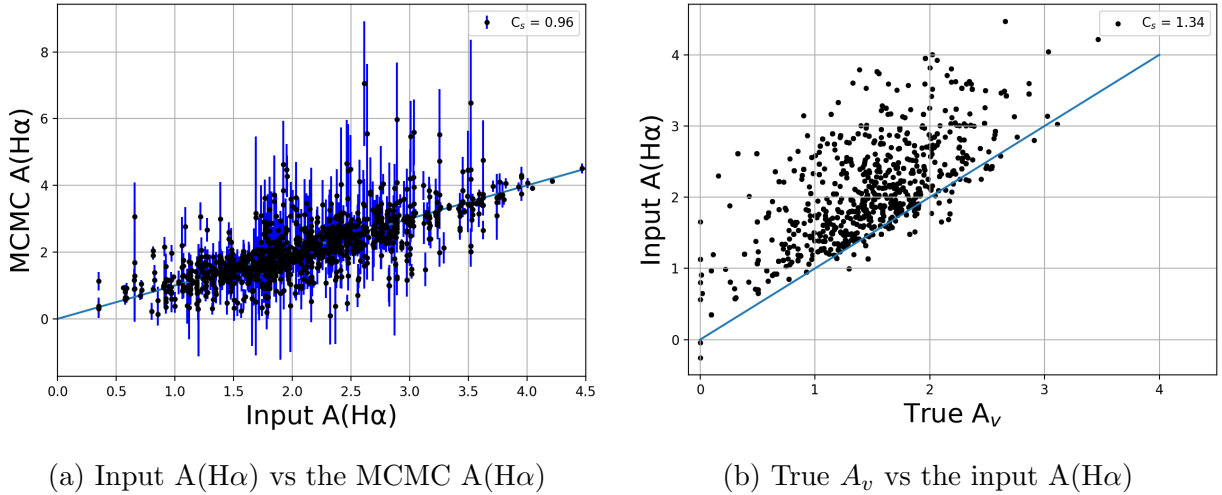
Figure 59: The comparison plot in Fig.59a is of the MCMC A(Hα) and the input A(Hα) derived using the Balmer decrement. Fig.59b compares the true A_v used by the simulation and the input A(Hα) derived using the Balmer decrement.

The Hα and Hβ dust corrected luminosity comparison plots are displayed in Fig.60; the scatter in these plots are largely dependent on the flux differences in Fig.59a. Removing the effects of the dust attenuation further offsets the MCMC estimates from the input values, with C_s factors now at 0.6-0.65. Since the attenuation is measured in magnitudes, the 4 % offset from the input A(Hα) values has further offset the luminosity distributions by up to 15 %. Nevertheless, the linear correlations in these dust corrected plots are very encouraging for the initial analysis of the WEAVE data.

(a) Hβ dust corrected luminosities.

(b) Hα dust corrected luminosities
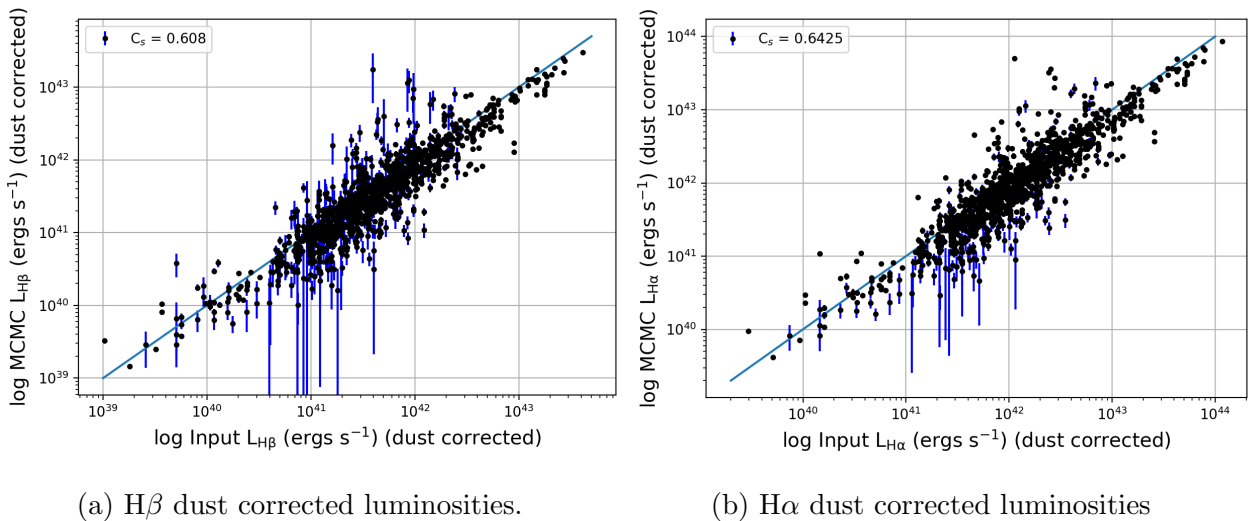
Figure 60: Comparison plots of the MCMC luminosities and the input luminosities which are dust corrected using the Balmer decrement.

The E(B − V) comparison plot in Fig.61a mimics that of Fig.59b. The colour-map of this plot in Fig.61b suggests that there is some correlation between the SNR and the

scatter in the E(B − V) estimation. E(B − V) is a function of the $F_{H\alpha}/F_{H\beta}$ ratio, which would be significantly affected by the N_b/N_r for targets with redshift values less than 0.2. These are plotted in Fig.61c with a colour-map of the N_b/N_r ratios estimated by the MCMC continuum fitting algorithm. There is a clear correlation between the E(B − V) outliers and the normalisation ratios which indicates the calibration offsets have either been incorrectly applied to the MCMC estimates or the input spectra also suffer from this offset. From the lack of correlation between this sample and the SNR colour-map in Fig.62a, I concluded that the noise is not a contributing factor to the severe scattering. Removing the N_b/N_r offset correction in Fig.62b drastically reduces the amount of scattering, forming a much stronger linear correlation with the E(B − V) input data set and the SNR now follows a similar trend to the rest of the data in Fig.61b.

The MCMC E(B − V) estimates form a strong linear correlation with the input values if the offset correction is not applied; the C_s factor is now 1.02. There are three possible explanations for this: either the input data is also affected by the offset caused by an error in the flux calibration, I have incorrectly applied the offset to the Hβ fluxes or MCMC did not recover accurate measurements for the normalisation parameters. As previously explained, if the wrong BC03 template is selected as the best-fit for the continuum then the algorithm is only capable of returning values for the three parameters along their correlations. It is possible that poor estimates of the continuum normalisation parameters are causing the scattering in Fig.62a. It is also plausible that the input spectra are also affected by the source of the offset for the OPR3 spectra. However, the uncorrected MCMC E(B − V) values in Fig.62b are consistently larger than those derived from the input spectra by 13%. There is undoubtedly a systematic offset occurring somewhere, however it is difficult to determine how to rectify it without knowing the source.

(a)

(b)   (c)
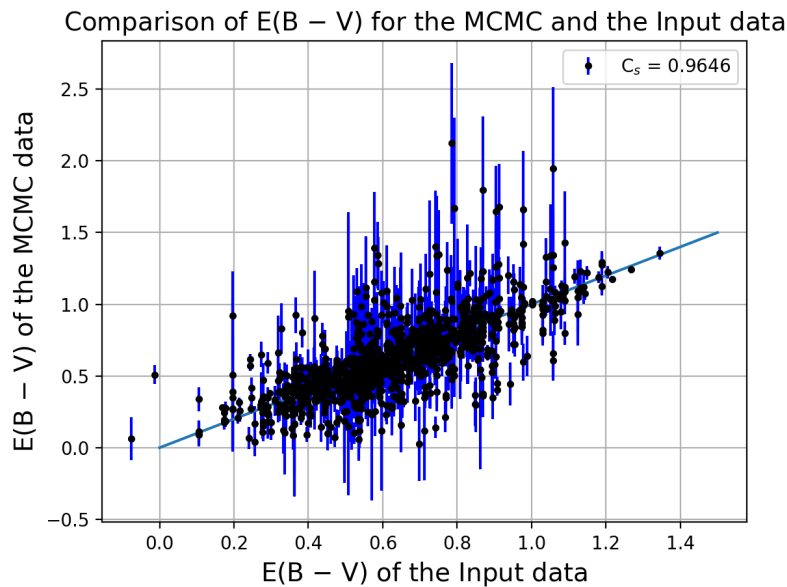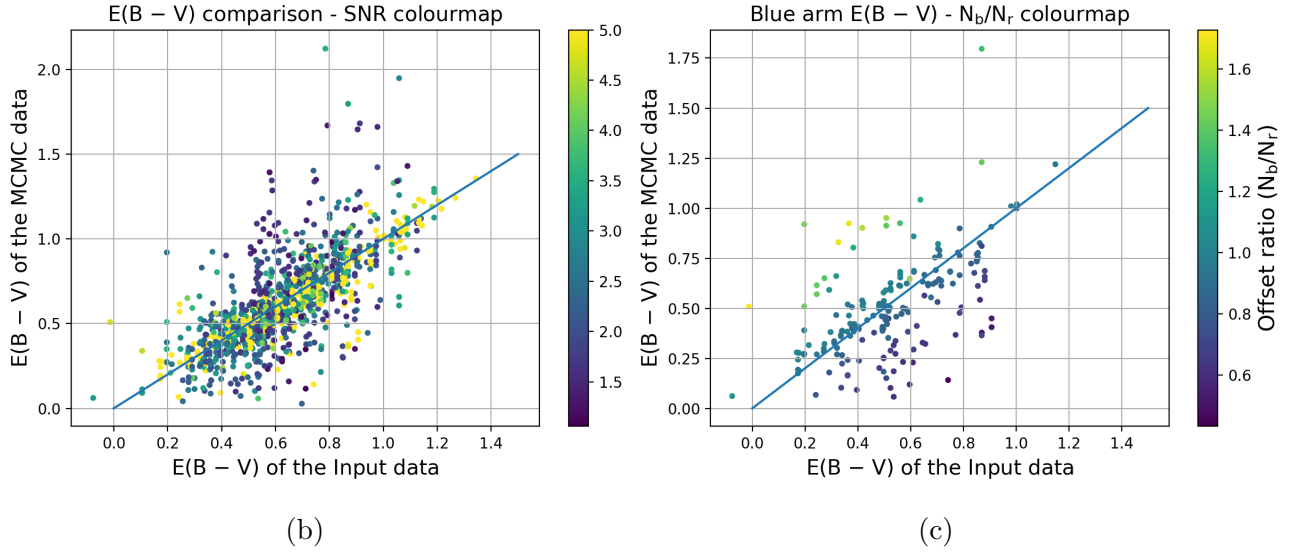
Figure 61: Comparison plots of $E(B - V)$ derived from MCMC estimates and the input data. Fig.61a plots the data with the MCMC errors and Fig.61b overlays a SNR colour map onto the data with the maximum value set to 5 (high SNR spectra are indicated in yellow). Fig.61c only includes the spectra where $H\beta$ fell within the wavelength range of the blue arm; the N_b/N_r offset is overlaid on this plot.

(a)   (b)
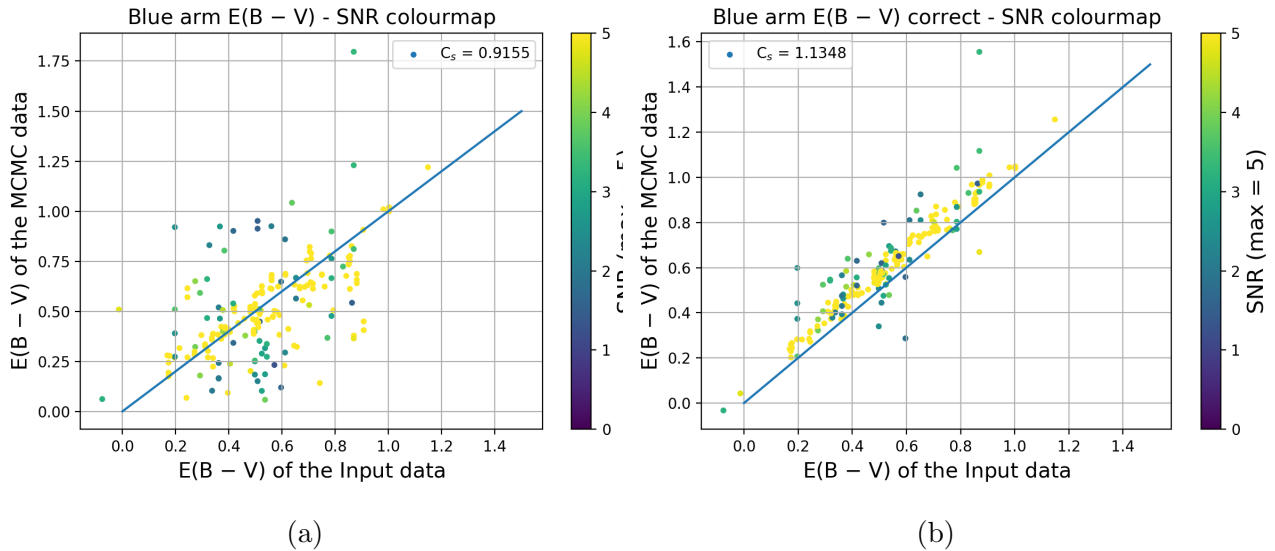
Figure 62: Comparison plots of $E(B - V)$ for a small sample of the OPR3 spectra with $z < 0.2$; the redshifted emission lines in the $H\beta$ for all the spectra in this sample fell within the wavelength range of the blue arm. Both the plots overlay a SNR colour map with the largest SNR (> 5) colour coded in yellow. Fig.62a plots the data with the N_b/N_r correction applied to the $H\beta$ flux and Fig.62b plots the data with the correction removed.

The general trend of the SNR colour map in Fig.63a suggests that the scatter is largely due to low SNR spectra, however the furthest two MCMC outliers have SNRs greater than

4. After investigating each of the emission line fits for these spectra I discovered that the MCMC algorithm underestimated the Hβ flux by 80%. Fig.64 plots the fit of the narrow and broad Hβ lines in each of these spectra. The model estimates that the broad line emission accounts for 93% of the flux in Fig.64a and 90% in Fig.64b. It is possible that the narrow emission has been mistakenly modelled as part of its broad line component in these two spectra. Given the proximity of the two structures and the freedom required by the broad line centre, it is inevitable that these two blended lines will at times come into conflict. The MCMC/input fraction of the Hβ fluxes are compared to the E(B $-$ V) comparison plot using a logarithmic colour-map in Fig.63b. This appears to be the dominant source of the scattering in the dust corrected luminosity plots. Hβ is a weak line relative to Hα, therefore even low-medium levels of noise make it difficult for MCMC to recover the input flux. As stated, it is also blended with its broad line counterpart which can mistakenly model part of the narrow lines emission.

(a)   (b)
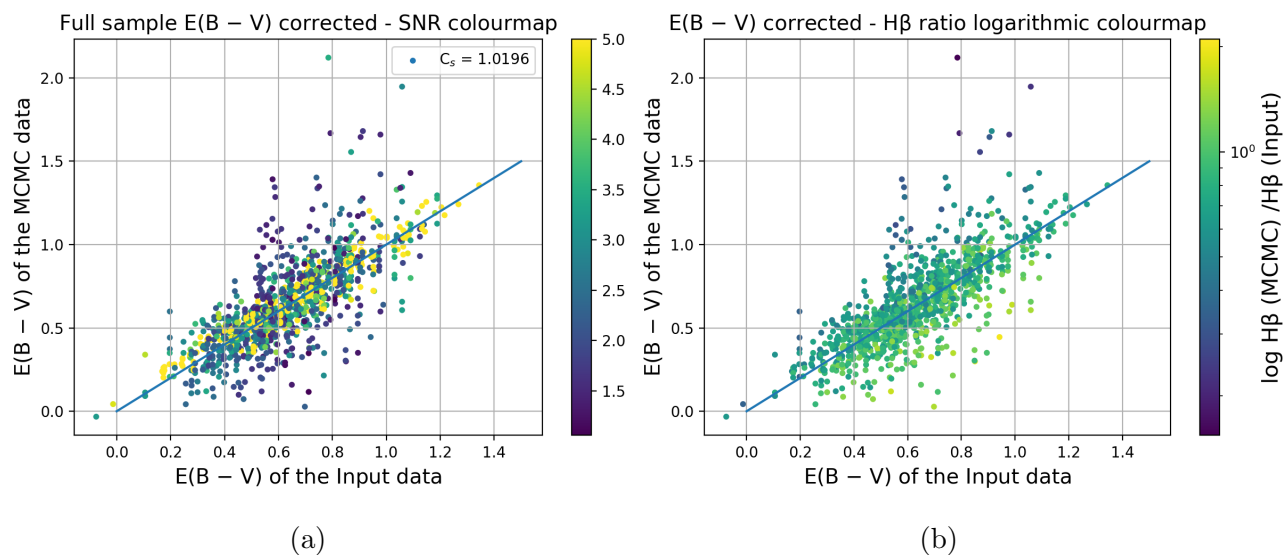
Figure 63: The full OPR3 sample with the N_b/N_r ratio removed from the Hβ fluxes in Fig.62. A SNR colour map is plotted with the data in Fig.63a and a colour map of the Hβ flux ratios for the MCMC estimates and input values is overlaid in Fig.63b.

(a) Furthest outlier in Fig.63   (b) Second furthest outlier in Fig.63
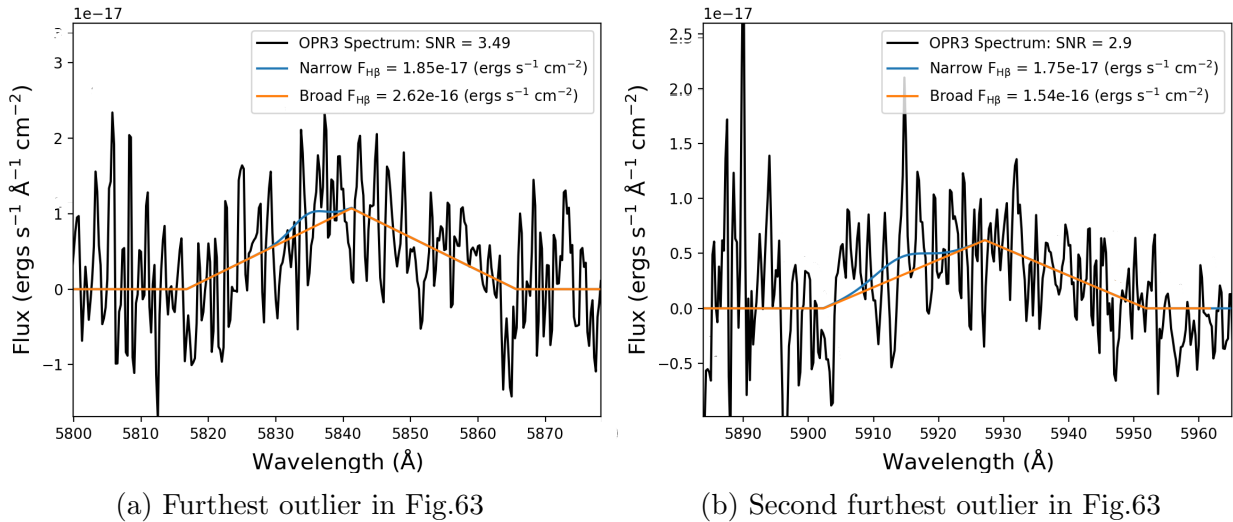
Figure 64: Broad and narrow fits of the Hβ line in the two furthest outliers in Fig.63. The black line represents the spectrum, the blue shows the fit of the narrow line using a Gaussian model and the orange the fit of the broad line using a triangular profile model.

8.4   SFR calculation and analysis

Fig.65 presents two comparison plots of the SFRs derived from the MCMC estimates against the SKA simulated skies (Wilman et al., 2008) 150 MHz radio measurements (Fig.65a) and those derived from the known input luminosities (Fig.65b). I have taken the given input Hα luminosities, converted them to fluxes, corrected for extinction, and then calculated the input SFR. Fig.65b is, as expected, identical to the dust corrected Hα luminosity plot in Fig.60, the only difference is a factor of 7.9×10^{-42} in both the data sets. The SFR(L$_{150}$) values in the Fig.65a comparison plot were taken from the SKA simulated skies. These measurements are derived from 150 MHz radio continuum measurements which are expected to be detected by LOFAR for each of the targets. The MCMC SFR(Hα)s underestimate the SFR(L$_{150}$)s by nearly 35%, with a large amount of scatter in Fig.65a. The SFRs derived from the simulated input spectra and the simulated radio continuum are compared in Fig.66; the input SFRs are $\sim 10\%$ lower than the radio derived SFRs. This difference of 25% could either be explained by the potential systematic offset or perhaps the 25% of the emission lines flux is expected to be lost upon entering the Earth's atmosphere. Further investigation must be done into the systematic offset, which is potentially caused by an issue with the flux calibration, in order to understand what is causing a large fraction of the flux to be underestimated.
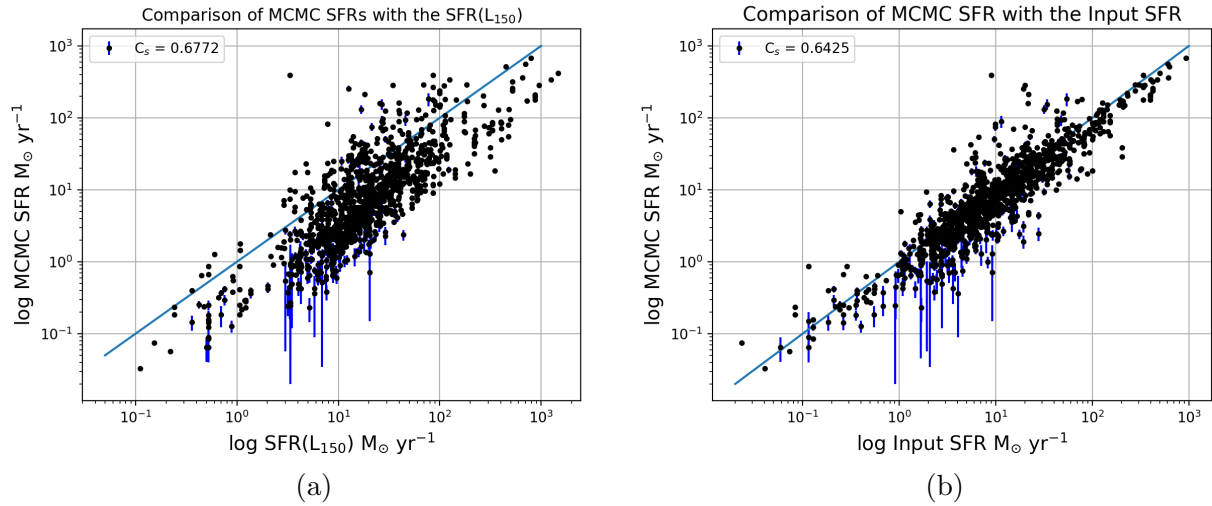
Figure 65: Fig.65a: Comparison of the SFRs derived from the MCMC estimated Hα fluxes vs the simulated LOFAR radio SFRs. Fig.65b: Comparison of the SFRs derived from the MCMC estimated Hα fluxes vs those from the input Hα luminosities.
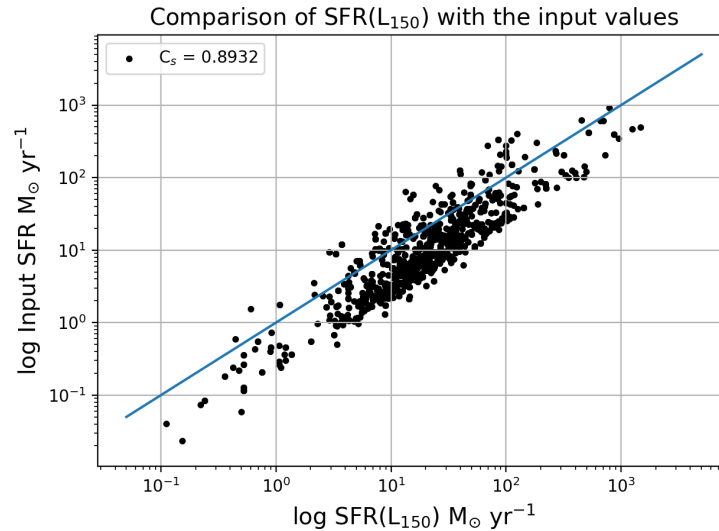
Figure 66: Comparison of the $SFR(L_{150})$ with the derived input SFRs.

9 Discussion

I have developed and tested a fitting algorithm for the BPT-NII emission lines in the WEAVE-LOFAR OPR3 star-forming galaxy spectra using MCMC techniques. An initial attempt was made to fit the entire wavelength range of the spectrum which highlighted an issue with the flux calibration. The BC03 templates and the Calzetti reddening curve, used to build the spectra, failed to model the continuum as a negative A_v was required for the

best-fit. This indicated that the shape of the continuum has been distorted, and further investigation indicated that the blue and red arm spectra were often offset from each other. This offset proved to be inconsistent throughout the OPR3 spectra, hence its cause and effect were difficult to establish. Two normalisation parameters were used to model the offset and their ratio was used to align the two spectra in an attempt to correct it. To circumvent the requirement of a negative A_v for an acceptable fit of the continuum, I instead focused on modelling the continuum only in a small range around the emission lines of interest for BPT classification. The local wavelength ranges were defined as two regions: $\pm 200 \times (1+z)$ Å either side of Hβ and OIII λ /5007 Å for the Hβ region and $\pm 200 \times (1+z)$ Å either side of NII λ /6548 Å and NII λ /6584 Å for the Hα region. A shorter wavelength range alleviated the aforementioned problems with wavelength dependent flux calibration issues and more optimal dust and normalisation parameters could be found using an MCMC algorithm with a lower bound of 0 set for A_v. This resulted in significantly lower χ_ν^2 values and the continuum surrounding the emission lines could be adequately removed so that the only significant features that remained were emission lines.

To validate the MCMC algorithm I built simplified model spectra using the BC03 templates, the Calzetti reddening curve and Gaussian profiles for the broad and narrow emission lines. In this way, I demonstrated that the algorithm is performing as expected, with well recovered parameters and sensible uncertainties. During this process it became evident that MCMC could not return the true parameter values within reasonable uncertainties, however it is capable of retrieving estimates along the strong correlations between the continuum parameters. Further results from the continuum fitting of the OPR3 sample showed that the A_v estimates were strongly dependent on the template selected to model the spectrum. The template was selected based on the fit with a χ_ν^2 closest to 1, upon reflection the template with the lowest χ_ν^2 should instead be selected, therefore it would be interesting to see how this change in criteria would affect the template selection and the A_v estimates. I concluded that the A_v measurements using this selection criteria for the template fits were unreliable, and further suggested that the normalisation parameters used to realign the blue spectrum with the red were insufficient to account for the issues with flux calibration since the problem remains after applying them. Nevertheless, the A_v estimates for each BC03 template did form linear correlations with the input values, with gradients of 1, which is very encouraging. Further evidence of Hβ flux measurements in the blue arm proved that the offset had not been modelled correctly, as MCMC derived E(B - V) measurements using the Balmer decrement correlated with the input data with significantly less scatter without the offset correction. The MCMC best-fit E(B-V) values revealed a strong linear relationship with the input values, however there was still a very clear offset of 13 % from the input data. This suggests that there is still a systematic offset which is unaccounted for, potentially caused by the flux calibration, which must be addressed before calibrating and attempting to fit that real WEAVE data output.

The systematic offset was further highlighted in the MCMC vs input flux comparison plots of the emission line measurements from the 1163 spectra in the sample. The MCMC flux estimates for each of the emission lines are all offset from the input fluxes within ± 0.1 of 0.73. The MCMC fitting algorithm has proved to reliably model the narrow emission lines using the simplified model spectra, and the low χ_ν^2 fits (< 3.23) of the OPR3 spectra suggest the algorithm has performed remarkably well. Therefore, we speculate that the flux

calibration issue is responsible for the underestimation of the input fluxes by $\sim 25\%$.

Some of the skylines were not correctly subtracted, particularly at longer wavelengths, and left large residuals behind which are not accounted for in the RMS array In other cases, such as the OI 6300 Å line and the skyline feature between 6865-6890 Å it appears as though there has been no attempt to be subtract them. This resulted in contaminated emission lines which interfered with the emission line modelling. These must either be correctly subtracted before the fitting process or the accuracy of the sky subtraction must be included in the RMS array of the spectra. Low SNR spectra (< 3) can also present an issue with the dust correction of the Hα line using the Balmer decrement due to uncertain Hβ flux estimation. Even in the absence of extinction, in the Case B scenario, Hβ is a factor of 2.86 weaker than Hα, therefore it is harder for MCMC to extract the correct line profile parameters. Furthermore, Hβ is also blended with its broad counterpart and MCMC has, at times, been unable to distinguish between the emission of the two components. The fraction over or underestimated by the MCMC Hβ fluxes strongly correlated with the scatter in the E(B - V) comparison plot, indicating that poor Hβ estimates strongly influence the accuracy of the attenuation derived using the Balmer decrement.

The Gaussian function proved to poorly model the broad components of each of the lines in the spectrum, with significantly better fits using a model with a triangular profile. Unlike in the real universe where there are physical explanations for the intrinsic velocity profiles of emission lines that we observe, in the simulations any line profile is theoretically possible. Following discussions with the people who built the input simulated spectra, we are unable to explain how they came to have the observed shape, and we therefore made the pragmatic decision to adopt the triangular model. The flux of the broad lines hold no relevant information about the nebular emission, hence it is not necessary to physically interpret them. The only purpose of modelling these structures was to remove them from the spectra by selecting the model which resulted in the best-fit and χ^2_ν closest to 1. The real WEAVE data will have broad lines, therefore any issues or complications that arose from modelling multiple, blended line components in the simulated OPR3 spectra will also be the case in real radio-source spectra.

The main aim of this research was to build an algorithm which could be used on the real WEAVE spectra. Once the flux calibration issue is resolved, full spectrum fitting of the continuum should be the preferred method over the masked method used in this thesis in order to retrieve accurate A_v estimates and to study the stellar population of galaxies. Once the cause of the offset and shape distortion has been isolated and fixed, the algorithm I have built is capable of fitting the full spectral range and no alterations are required for this to work. Although the spectral lines will need to be masked in the preparation stage prior to fitting the continuum. Additional species of emission lines can be easily modelled alongside the BPT-NII lines and it is also possible to simultaneously model the continuum; however, a compromise will have to be made for the dimensionality of the optimisation problem and a demand on CPU time and resources. The parameters used in the triangular function to model the broad line components in the OPR3 spectra are analogous to the Gaussian parameters, therefore few alterations will be required to change this for the real WEAVE spectra. Upon reflection, the velocity offset parameter for the narrow line components was not essential as any velocity difference between the emission and observed wavelength of the narrow lines is accounted for in the redshift. However, it is possible that the redshifts for the

real WEAVE data will be calculated using the continuum, therefore this parameter should be included to model any offset between the continuum and the emission lines.

The continuum and emission line models and the MCMC algorithm has performed exceptionally well for the OPR3 spectra, with χ^2_ν less than 3.23 and posterior distributions for the parameters that appear Gaussian. Even the largest χ^2_ν have proved to be a result of the presence of skylines or their residuals which are not accounted for in the RMS array and not a reflection on the MCMC algorithm's performance limitations. In these cases, the spectra have not been removed from the sample if they only contaminate the continuum or the broad lines, and leave the narrow emission lines unblemished. Most of the spectra with skylines which came into conflict with the narrow emission lines were removed from the sample prior the line fitting procedure. This reduced the sample by 268, $\sim 20\%$, which further demonstrates the requirement for a successful sky subtraction or modelling. The algorithm was specifically intended to accurately model for low SNR spectra (< 5).

Naturally, the fractional uncertainties for the flux become larger for lower SNR spectra, and there is slightly more scatter in the comparison plots. However, there is still a very clear linear correlation between the lower SNR (< 5) MCMC estimates and the known input fluxes which appears to follow the same gradient as the estimates with SNR > 5. Furthermore, the BPT-NII comparison plot demonstrates relatively low scatter which correlates with the SNR of the spectra. In conclusion, the MCMC algorithm is capable of handling low SNR spectra (< 5) and returning reliable flux estimates for the emission lines.

The BPT-NII diagram and the (Kauffmann et al., 2003) demarcation curve were used to classify radio-sources into star-forming or AGN galaxies. The line flux ratios of NII $\lambda6584$ Å and Hα vs the ratios of OIII $\lambda5007$ Å and Hβ were used in the BPT-NII diagram. Using the flux ratios of the MCMC estimates, I successfully managed to correctly classify 89% of the targets in the sample based on the (Kauffmann et al., 2003) demarcation curve; 2.5% were incorrectly classified as star-forming galaxies and 8.5% were incorrectly classified as AGN. This is a very encouraging outcome of this thesis, as it indicates that WEAVE can be used to determine reliable classifications with a very high accuracy.

Another motivation of my project was to verify the simulated SFR(L_{150}) LOFAR measurements by comparing them to the estimated SFR(Hα) of the OPR3 sample. Fig.65a provides an informative overview on how the two SFR measurements compare and how representative the radio SFR measurements are. There is a linear correlation between the two sets of data with the gradient appearing equivalent with the 1:1 reference line. This is so far encouraging for the SFR(L_{150}) data, although they overestimate the SFR(Hα) values by 33% so it would be interesting to see how the comparison changes once the flux is calibrated correctly.

As stated, the flux calibration used for the OPR3 spectra should be reviewed in order to identify the cause of the offset between the blue and red spectra, the wavelength dependence of the necessary corrections and also to investigate the 20-25% underestimation of the MCMC estimates of the emission fluxes relative to the input values. The blue and red arm wavelength range overlap can be used for this investigation at $z \sim 0.2$ when the three emission lines in the Hβ region can be detected by both arms. Two sets of measurements for each emission line can be taken using the red and blue arm spectrum which can be compared and investigated for any offset. Furthermore, the BPT and flux comparison plots can be analysed for multiple spectra in the OPR3 sample with the same targets. Each of these spectra were simulated with

varying observing conditions, hence it would be beneficial to understand how this affects the fits and their flux measurements as well as looking at whether the SNR increases as expected with the square root of the integration time. A comparison of multiple measurements in the same observing conditions can be analysed to learn about the stability of the spectrograph, and if repeat observations are made through different fibres then this can indicate how well the flux calibration is working.

In conclusion, the MCMC spectral fitting algorithm presented in this thesis has proved to retrieve reliable emission line measurements for the OPR3 spectra. Minor adjustments can be made for the full spectral fitting of the real WEAVE data once the sky subtraction and flux calibration is applied correctly. Successful BPT classifications can be made using the MCMC measurements with 89% of the sample in the correct BPT class. Finally, the Hα derived SFRs have so far indicated that the SFR(L$_{150}$) radio measurements are most likely representative of the true SFR, however further analysis is required to verify this.

References

Alam S., et al., 2015, ApJS, 219, 12

Antonucci R., 1993, ARA&A, 31, 473

Baldry I. K., Glazebrook K., Driver S. P., 2008, MNRAS, 388, 945

Baldwin J. A., Phillips M. M., Terlevich R., 1981, PASP, 93, 5

Balzano V. A., 1983, ApJ, 268, 602

Barkana R., Loeb A., 2001, , 349, 125

Becker R. H., et al., 2001, AJ, 122, 2850

Bell A. R., 1978, MNRAS, 182, 443

Bell E. F., 2003, ApJ, 586, 794

Berman L., 1936, MNRAS, 96, 890

Best P. N., Heckman T. M., 2012, MNRAS, 421, 1569

Blanc G. A., et al., 2011, ApJ, 736, 31

Bongiorno A., et al., 2016, A&A, 588, A78

Bruzual G., Charlot S., 2003, MNRAS, 344, 1000

Burgess A., 1958, MNRAS, 118, 477

Cai Z.-Y., Lapi A., Bressan A., De Zotti G., Negrello M., Danese L., 2014, ApJ, 785, 65

Calzetti D., 2013, Star Formation Rate Indicators. p. 419

Calzetti D., Kinney A. L., Storchi-Bergmann T., 1994, ApJ, 429, 582

Calzetti D., Armus L., Bohlin R. C., Kinney A. L., Koornneef J., Storchi-Bergmann T.,
2000, ApJ, 533, 682

Cappellari M., 2017, MNRAS, 466, 798

Cappellari M., Emsellem E., 2004, PASP, 116, 138

Choudhury T. R., Ferrara A., 2006, arXiv e-prints, pp astro–ph/0603149

Condon J. J., 1992, ARA&A, 30, 575

Condon J. J., Cotton W. D., Greisen E. W., Yin Q. F., Perley R. A., Taylor G. B., Broderick
J. J., 1998, AJ, 115, 1693

Cox P., Mezger P. G., 1989, , 1, 49

Dalton G., et al., 2016, in Ground-based and Airborne Instrumentation for Astronomy VI. p. 99081G, doi:10.1117/12.2231078

Dalton G., et al., 2018, in Ground-based and Airborne Instrumentation for Astronomy VII. p. 107021B, doi:10.1117/12.2312031

Davé R., 2008, MNRAS, 385, 147

Davies L. J. M., et al., 2018, MNRAS, 480, 768

Davis T. A., et al., 2012, MNRAS, 426, 1574

Dimeo R., 2005, PAN: Peak Analysis, `ftp://ftp.ncnr.nist.gov/pub/staff/dimeo/pandoc.pdf`

Dopita M. A., Evans I. N., 1986, ApJ, 307, 431

Dopita M. A., Sutherland R. S., 1995, ApJ, 455, 468

Dopita M. A., Koratkar A. P., Allen M. G., Tsvetanov Z. I., Ford H. C., Bicknell G. V., Sutherland R. S., 1997, ApJ, 490, 202

Dopita M. A., Kewley L. J., Heisler C. A., Sutherland R. S., 2000, ApJ, 542, 224

Dopita M. A., et al., 2006, ApJS, 167, 177

Driver S. P., et al., 2011, MNRAS, 413, 971

Driver S. P., et al., 2019, The Messenger, 175, 46

Eales S., et al., 2010, PASP, 122, 499

Eales S., et al., 2018, MNRAS, 473, 3507

Elbaz D., et al., 2007, A&A, 468, 33

Evans Neal J. I., 1999, ARA&A, 37, 311

Fabian A. C., 2012, ARA&A, 50, 455

Foreman-Mackey D., Hogg D. W., Lang D., Goodman J., 2013, Publications of the Astronomical Society of the Pacific, 125, 306–312

Gavin H., 2013.

Goodman J., Weare J., 2010, Communications in Applied Mathematics and Computational Science, 5, 65

Groves B., Brinchmann J., Walcher C. J., 2012, MNRAS, 419, 1402

Gunn J. E., Peterson B. A., 1965, ApJ, 142, 1633

Gürkan G., et al., 2018, MNRAS, 475, 3010

Hao C.-N., Kennicutt R. C., Johnson B. D., Calzetti D., Dale D. A., Moustakas J., 2011, ApJ, 741, 124

Hardcastle M. J., Croston J. H., 2020, , 88, 101539

Hardcastle M. J., Evans D. A., Croston J. H., 2007, MNRAS, 376, 1849

Hardcastle M. J., et al., 2016, MNRAS, 462, 1910

Hardcastle M. J., et al., 2019, A&A, 622, A12

Harrison E., 1993, ApJ, 403, 28

Hayes M., Schaerer D., Östlin G., Mas-Hesse J. M., Atek H., Kunth D., 2011, ApJ, 730, 8

Heckman T. M., 1980, A&A, 500, 187

Heckman T. M., Best P. N., 2014, ARA&A, 52, 589

Heesen V., Brinks E., Leroy A. K., Heald G., Braun R., Bigiel F., Beck R., 2014, AJ, 147, 103

Helou G., Soifer B. T., Rowan-Robinson M., 1985, ApJ, 298, L7

Ho L. C., Filippenko A. V., Sargent W. L. W., 1993, ApJ, 417, 63

Hubble E., 1929, Proceedings of the National Academy of Science, 15, 168

Huchra J. P., 1977, ApJS, 35, 171

Johnson B. D., et al., 2007, ApJS, 173, 392

Kauffmann G., et al., 2003, MNRAS, 346, 1055

Kauffmann G., White S. D. M., Heckman T. M., Ménard B., Brinchmann J., Charlot S., Tremonti C., Brinkmann J., 2004, MNRAS, 353, 713

Keel W. C., 1983, ApJ, 269, 466

Kennicutt Robert C. J., 1998, ARA&A, 36, 189

Kennicutt R. C., Evans N. J., 2012, ARA&A, 50, 531

Kennicutt Robert C. J., Tamblyn P., Congdon C. E., 1994, ApJ, 435, 22

Kewley L. J., Heisler C. A., Dopita M. A., Lumsden S., 2001a, ApJS, 132, 37

Kewley L. J., Dopita M. A., Sutherland R. S., Heisler C. A., Trevena J., 2001b, ApJ, 556, 121

Khachikian E. Y., Weedman D. W., 1974, ApJ, 192, 581

Koski A. T., 1978, ApJ, 223, 56

Lagos C. D. P., Padilla N. D., Strauss M. A., Cora S. A., Hao L., 2011, MNRAS, 414, 2148

Le Fèvre O., et al., 2003, in Iye M., Moorwood A. F. M., eds, Society of Photo-Optical Instrumentation Engineers (SPIE) Conference Series Vol. 4841, Instrument Design and Performance for Optical/Infrared Ground-based Telescopes. pp 1670–1681, doi:10.1117/12.460959

Leitet E., Bergvall N., Hayes M., Linné S., Zackrisson E., 2013, A&A, 553, A106

Loeb A., Barkana R., 2001, ARA&A, 39, 19

Madau P., Dickinson M., 2014, ARA&A, 52, 415

Madau P., Pozzetti L., Dickinson M., 1998, ApJ, 498, 106

Mannucci F., Cresci G., Maiolino R., Marconi A., Gnerucci A., 2010, MNRAS, 408, 2115

Maraston C., 2003, in Kissler-Patig M., ed., Extragalactic Globular Cluster Systems. p. 237 (arXiv:astro-ph/0301419), doi:10.1007/10857603˙37

Maraston C., 2007, in Combes F., Palouš J., eds, Vol. 235, Galaxy Evolution across the Hubble Time. pp 52–56, doi:10.1017/S1743921306005047

Martin D. C., et al., 2005, ApJ, 619, L1

Massey P., Hanson M. M., 2013, Astronomical Spectroscopy. p. 35, doi:10.1007/978-94-007-5618-2˙2

Matsuoka Y., et al., 2019, ApJ, 872, L2

McKee C. F., Ostriker E. C., 2007, ARA&A, 45, 565

Moustakas J., Kennicutt Robert C. J., Tremonti C. A., 2006, ApJ, 642, 775

Murphy E. J., et al., 2011, ApJ, 737, 67

Newville M., Stensitzki T., Allen D. B., Ingargiola A., 2014, LMFIT: Non-Linear Least-Square Minimization and Curve-Fitting for Python, doi:10.5281/zenodo.11813, https://doi.org/10.5281/zenodo.11813

Ocvirk P., Pichon C., Lançon A., Thiébaut E., 2006, MNRAS, 365, 46

Osterbrock D. E., 1989, Astrophysics of gaseous nebulae and active galactic nuclei

Perley R., et al., 2009, IEEE Proceedings, 97, 1448

Pilbratt G. L., et al., 2010, A&A, 518, L1

Porter J., Queener H., Lin J., Thorn K., Awwal A. A. S., 2006, Adaptive Optics For Vision Science. Wiley-Interscience

Ranganathan A., 2004, Academia.edu

Röttgering H., et al., 2011, Journal of Astrophysics and Astronomy, 32, 557

Sabater J., et al., 2019, A&A, 622, A17

Salim S., Narayanan D., 2020, ARA&A, 58, 529

Salpeter E. E., 1955, ApJ, 121, 161

Sarzi M., 2012, GANDALF: Gas and Absorption Line Fitting, `http://star-www.herts.ac.uk/~sarzi/gandalf_releases/`

Sarzi M., et al., 2006, MNRAS, 366, 1151

Sarzi M., et al., 2010, MNRAS, 402, 2187

Schreiber C., 2019, Slinefit: Measure redshifts and emission/absorption lines in 1D galaxy spectra, `https://github.com/cschreib/slinefit`

Seager S., Sasselov D. D., Scott D., 1999, ApJ, 523, L1

Seibert M., et al., 2005, ApJ, 619, L55

Seyfert C. K., 1943, ApJ, 97, 28

Shimwell T. W., et al., 2017, A&A, 598, A104

Shimwell T. W., et al., 2019, A&A, 622, A1

Shlosman I., Begelman M. C., Frank J., 1990, Nature, 345, 679

Smit R., Bouwens R. J., Franx M., Illingworth G. D., Labbé I., Oesch P. A., van Dokkum P. G., 2012, ApJ, 756, 14

Smith G., et al., 2004, Proc SPIE, 5492

Smith D. J. B., et al., 2014, MNRAS, 445, 2232

Smith D. J. B., et al., 2016, in Reylé C., Richard J., Cambrésy L., Deleuil M., Pécontal E., Tresse L., Vauglin I., eds, SF2A-2016: Proceedings of the Annual meeting of the French Society of Astronomy and Astrophysics. pp 271–280 (`arXiv:1611.02706`)

Smith D. J. B., Best P. N., Duncan K. J., Hatch N. A., Jarvis M. J., Röttgering H. J. A., Simpson C. J., Stott J. P., 2019.

Stasińska G., Cid Fernandes R., Mateus A., Sodré L., Asari N. V., 2006, MNRAS, 371, 972

Sunyaev R. A., Chluba J., 2009, Astronomische Nachrichten, 330, 657

Tabatabaei F. S., et al., 2017, ApJ, 836, 185

Urry C. M., Padovani P., 1995, PASP, 107, 803

Veilleux S., Osterbrock D. E., 1987, ApJS, 63, 295

Werner M. W., et al., 2004, ApJS, 154, 1

Westmoquette M. S., Exter K. M., Smith L. J., Gallagher J. S., 2007, MNRAS, 381, 894

Wilman R. J., et al., 2008, MNRAS, 388, 1335

Wright E. L., et al., 2010, AJ, 140, 1868

York D. G., et al., 2000, AJ, 120, 1579

Yun M. S., Reddy N. A., Condon J. J., 2001, ApJ, 554, 803

Zaroubi S., 2013, The Epoch of Reionization. p. 45, doi:10.1007/978-3-642-32362-1˙2

van Haarlem M. P., et al., 2013, A&A, 556, A2

van Ravenzwaaij D., Cassey P., Brown S., 2016, IEEE Proceedings, 97, 143–154

van der Hulst J. M., Terlouw J. P., Begeman K. G., Zwitser W., Roelfsema P. R., 1992, in Worrall D. M., Biemesderfer C., Barnes J., eds, Astronomical Society of the Pacific Conference Series Vol. 25, Astronomical Data Analysis Software and Systems I. p. 131

van der Kruit P. C., 1971, A&A, 15, 110

List of Figures